Effects of superstructuring on optical and transport properties of selected layered materials

Velebit, Kristijan

Doctoral thesis / Disertacija

2015

Degree Grantor / Ustanova koja je dodijelila akademski / stručni stupanj: **University of Zagreb, Faculty of Science / Sveučilište u Zagrebu, Prirodoslovno-matematički fakultet**

Permanent link / Trajna poveznica: https://urn.nsk.hr/urn:nbn:hr:217:613872

Rights / Prava: In copyright / Zaštićeno autorskim pravom.

Download date / Datum preuzimanja: **2024-04-17**

Repository / Repozitorij:

Repository of the Faculty of Science - University of Zagreb

DIGITALNI AKADEMSKI ARHIVI I REPOZITORIJI

UNIVERSITY OF ZAGREB
FACULTY OF SCIENCE
DEPARTMENT OF PHYSICS

Kristijan Velebit

EFFECTS OF SUPERSTRUCTURING ON OPTICAL AND TRANSPORT PROPERTIES OF SELECTED LAYERED MATERIALS

DOCTORAL THESIS

Zagreb, 2015

UNIVERSITY OF ZAGREB
FACULTY OF SCIENCE
DEPARTMENT OF PHYSICS

Kristijan Velebit

EFFECTS OF SUPERSTRUCTURING ON OPTICAL AND TRANSPORT PROPERTIES OF SELECTED LAYERED MATERIALS

DOCTORAL THESIS

Supervisor: Dr. Ana Smontara

Zagreb, 2015

SVEUČILIŠTE U ZAGREBU
PRIRODOSLOVNO-MATEMATIČKI FAKULTET
FIZIČKI ODSJEK

Kristijan Velebit

UTJECAJ SUPERSTRUKTURIRANJA NA OPTIČKA I TRANSPORTNA SVOJSTVA ODABRANIH SLOJEVITIH MATERIJALA

DOKTORSKI RAD

Mentor: dr.sc. Ana Smontara

Zagreb, 2015.

This thesis was made under the mentorship of dr. sc. Ana Smontara as a part of the doctoral study at the Department of Physics, Faculty of Science, University of Zagreb. Presented experimental work was carried out at the 1. Physikalisches Institut, Universität Stuttgart in Germany and in the *Laboratory for the physics of transport phenomena* at the Institute of Physics in Zagreb, Croatia.

Ovaj doktorski rad je izrađen pod mentorstvom dr. sc. Ane Smontare u sklopu doktorskog studija na Fizičkom odsjeku Prirodoslovno-matematičkog fakulteta Sveučilišta u Zagrebu. Predstavljeni eksperimentalni rad proveden je na 1. Physikalisches Institut, Universität Stuttgart (Njemačka) i u *Laboratoriju za fiziku transportnih svojstava* Instituta za fiziku u Zagrebu (Hrvatska).

Acknowledgments

I am very grateful to my supervisor, Dr. Ana Smontara, for introducing me to the research of transport properties in condensed matter physics, for her guidance, and for her attention to details.

I am especially grateful to Dr. Eduard Tutiš for sharing his knowledge with me and for being an unlimited source of advice and support.

I wish to thank Prof. Dr. László Forró, Prof. Dr. Ivo Batistić, Dr. Jovica Ivkov, Prof. Dr. Neven Barišić, Prof. Dr. Ante Bilušić and Dr. Petar Popčević for shaping and aiding my scientific career in many ways, and for collaborating in my work. I am also grateful to Prof. Dr. Mario Basletić and Prof. Dr. Mihael S. Grbić for the work they have done on reviewing this thesis.

I am grateful to Prof. Dr. Martin Dressel for the hospitality I received at the 1. Physikalisches Institut, Universität Stuttgart, Germany, and for making this work possible. I thank Prof. Dressel and the researchers of the Institute for sharing their knowledge of optical techniques with me. I appreciate all the help with the preparation of the samples by Chem.-Tech. Gabriele Untereiner. I thank all members of the Institute for their help, and above all, for making me feel welcomed.

Most of all, I am grateful to my wife Karolina, my parents, Duško and Zlatica, and my sister Danijela for showing me love and support over the years.

BASIC DOCUMENTATION CARD

University of Zagreb
Faculty of Science
Department of Physics

Doctoral thesis

EFFECTS OF SUPERSTRUCTURING ON OPTICAL AND TRANSPORT PROPERTIES OF SELECTED LAYERED MATERIALS

Kristijan Velebit

Institute of Physics, Zagreb

Very special electronic phases brought upon by the superstructuring in layered materials have held the interest of researchers for decades. This thesis deals with the effects of the lattice superstructuring on optical and transport properties of pure and doped samples of 1T-TaS_2 and 1T-$TiSe_2$. This work brings the first ever analysis of the optical properties of the nearly-commensurate charge density wave (NCCDW) phase of 1T-TaS_2 at temperatures below 200 K. Optical response of the NCCDW phase is for the first time analyzed with the nano-composite-like nature of the phase in mind. Modeling of the optical response using the Bruggeman effective medium theory is suggested and demonstrated. As a result, localized surface plasmon feature is identified in the optical spectrum, as well as the asymmetry of the optical phonon modes brought upon by the coupling of spatially distinct nano-sized domains which comprise the material. A novel analysis of the superstructure-related phonon peaks which allows the determination of the charge redistribution over the star-like superstructure is presented. Lastly, this work also presents the study of the 1T-$TiSe_2$ compound, where the analysis is focused on the properties of the high temperature phase of the material. The contributions of electron and hole pockets are resolved for the first time, as well as the spectral weights and the scattering rates for each channel. Calculated energy ranges of the quasi-2D hole band settle the ongoing debate and determine that 1T-$TiSe_2$ in the high-temperature phase is a semimetal, with scattering which gets stronger over a wide interval as the temperature approaches the phase transition.

(148 pages, 49 figures, 4 tables, 155 references)

Keywords: layered materials, transition metal dichalcogenides, superstructuring, charge density wave, effective medium theory, localized surface plasmon, asymmetric phonon modes, charge redistribution, optical conductivity, infrared spectroscopy

Language of the original: English

Supervisor: Dr. Ana Smontara

Thesis defense committee:

1. Assoc. Prof. Dr. Mario Basletić,
   Faculty of Science, Department of Physics, Croatia

2. Dr. Ana Smontara, senior scientist,
   Institute of Physics, Croatia

3. Prof. Dr. László Forró,
   Ecole Polytechnique Fédérale de Lausanne, Switzerland

4. Assist. Prof. Dr. Neven Barišić,
   Technische Universität Wien, Austria

5. Dr. Eduard Tutiš, senior scientist,
   Institute of Physics, Croatia

Thesis accepted: October 13, 2015

Thesis is deposited in The Central Library for Physics, Faculty of Science - Department of Physics, Bijenička c. 32, Zagreb.

TEMELJNA DOKUMENTACIJSKA KARTICA

Sveučilište u Zagrebu Doktorska disertacija
Prirodoslovno-matematički fakultet
Fizički odsjek

UTJECAJ SUPERSTRUKTURIRANJA NA OPTIČKA I TRANSPORTNA SVOJSTVA ODABRANIH SLOJEVITIH MATERIJALA

Kristijan Velebit

Institut za fiziku, Zagreb

Vrlo posebne elektronske faze koje nastaju superstrukturiranjem slojastih materijala već desetljećima zaokupljaju pažnju istraživača. Ovaj doktorski rad proučava efekte superstrukturiranja kristalne rešetke na optička i transportna svojstva čistih i dopiranih uzoraka 1T-TaS$_2$ i 1T-TiSe$_2$. Rad donosi prvu analizu optičkih svojstava faze približno sumjerljivog vala gustoće naboja (*engl.* NCCDW) 1T-TaS$_2$ na temperaturama ispod 200 K. Po prvi put je optički odziv NCCDW faze analiziran uzimajući u obzir njenu nano-kompozitnu prirodu, te je predloženo i provedeno modeliranje optičkog odziva pomoću Bruggemanove teorije efektivnog medija. Kao rezultat, u optičkom spektru je identificiran učinak lokalnog površinskog plazmona, kao i asimetrija fononskih modova do koje dolazi zbog vezanja optičkog odziva prostorno razdvojenih nano-domena. Nadalje, predložena je nova analiza intenziteta super-strukturnih fononskih vrhova koja omogućava određivanje redistribucije naboja u zvjezdastoj superstrukturi. Napose, ovaj rad predstavlja i istraživanje 1T-TiSe$_2$, gdje je analiza usredotočena na svojstva visokotemperaturne faze materijala. Po prvi put su razlučeni doprinosi elektronskih i šupljinskih pobuđenja, te njihova spektralna težina i jačina raspršenja. Proračuni energijskog raspona kvazi-dvodimenzionalne šupljinske vrpce omogućuju zaključenje dugotrajne debate u korist zaključka da je 1T-TiSe2 u visokotemperaturnoj fazi “polumetal” (*engl.* semimetal), s raspršenjem koje jača preko vrlo širokog intervala u kojem se temperatura približava točki prijelaza.

(148 stranica, 49 slika, 4 tablice, 155 referenci)

Ključne riječi: slojeviti materijali, dihalkogenidi prijelaznih metala, superstrukturiranje, val gustoće naboja, teorija efektivnog medija, lokalizirani površinski plazmon, asimetrični fononski modovi, preraspodjela naboja, optička vodljivost, infracrvena spektroskopija

Jezik izvornika: engleski

Mentor: dr. sc. Ana Smontara

Povjerenstvo za obranu doktorata:

1. Izv. prof. dr. sc. Mario Basletić,
   Fizički odsjek, PMF, Hrvatska
2. Dr. sc. Ana Smontara, znanstvena savjetnica,
   Institut za fiziku, Hrvatska
3. Prof. dr. sc. László Forró,
   Ecole Polytechnique Fédérale de Lausanne, Švicarska
4. Dr. sc. Neven Barišić, znanstveni savjetnik,
   Technische Universität Wien, Austrija
5. Dr. sc. Eduard Tutiš, znanstveni savjetnik,
   Institut za fiziku, Hrvatska

Rad prihvaćen: 13. listopada 2015.

Rad je pohranjen u Središnjoj knjižnici za fiziku Prirodoslovno-matematičkog fakulteta, Fizički odsjek, Bijenička c. 32, Zagreb.

Contents

1. Introduction 1

1.1. Transition metal dichalcogenides 3

1.2. Important relations in optics 6

1.2.1. Drude-Lorentz model 6

1.2.2. Fano model 7

1.2.3. Effective medium theory (EMT) 8

1.2.4. Localized surface plasmon 9

1.3. Superstructuring and charge density waves (CDW) 12

1.3.1. Peierls transition 12

1.3.2. Kohn anomaly 14

1.3.3. Collective modes 17

1.3.4 Alternatives to Fermi nesting 18

2. Experimental Methods 19

2.1. Optical measurements 21

2.2. Fourier Transform Infrared Spectroscopy 23

2.3. Spectroscopic Ellipsometry 26

2.4. Electrical resistivity 27

2.5. Samples 28

3. Superstructuring of 1T-TaS$_2$ 29

3.1. The abundance of phases 31

3.2. Transport and optical properties of 1T-TaS$_2$ 34

3.3. Effects of doping and pressure 38

4. Nano-Composite Superstructuring in 1T-TaS$_2$ 43

4.1. Nano-composite nature of the mixed phase 45

4.2. Effect of the Fermi surface geometry on the mean free path in 1T-TaS$_2$ 45

4.3. EMT model of the NCCDW phase 49

4.3.1. The 2-component EMT model 49

4.3.2. The 3-component EMT model 54

4.4. Conclusions of Chapter 4 57

5. Charge Redistribution Over Superstructure 59

5.1. Optical conductivity of phonons 61

5.2. Optical conductivity for a reconstructed unit cell 62

5.3. Acoustic and dipolar modes 64

5.4. Optical response of a restructured system 66

5.5. Analysis of the NCCDW phonon data 68

5.6. Analysis of the CCDW phonon data 71

5.7. Conclusions of Chapter 5 73

6. Superstructuring of 1T-TiSe$_2$ 75

6.1. Introduction to 1T-TiSe$_2$ 77

6.2. Transport and optical properties of 1T-TiSe$_2$ 80

6.3. Normal phase of 1T-TiSe$_2$ 82

6.3.1. Effect of degeneracy on the band model 84

6.3.2. Two-band model of the normal phase 86

6.4. CDW phase of 1T-TiSe$_2$ 92

6.5. Effects of doping 94

6.6. Conclusions of Chapter 6 97

Conclusions **99**

APPENDIX A Introduction to Optical Properties of Solids **105**
A.1. Propagation of electromagnetic waves in vacuum 107
A.2. Propagation of electromagnetic waves in a medium 109
A.3. Reflectivity 111
A.4. Optical properties of metals 113
A.5. Optical properties of semiconductors 115
A.6. Conventions and comparison to experiments 117

APPENDIX B Bruggeman Effective Medium Theory **119**
B.1. Effective medium theory 121
B.2. Non-spherical grains 122
B.3. The percolation condition 124
B.4. Metallic grains in vacuum 125

Sažetak **129**
Bibliography **141**

Chapter 1

INTRODUCTION

1.1. Transition metal dichalcogenides

Superstructuring of the crystal lattice is an impressive companion of several states of matter. Superstructuring in layered materials proves to be especially intriguing due to the low dimensionality of the electron spectrum and a number of very special electronic phases layered materials have been exhibiting for decades. Layered members of the transition metal dichalcogenides (TMD) family hold the interest of this thesis. There are over 60 transition metal dichalcogenides, two-thirds of which have layered structures [Wilson1969]. Several interesting topics, such as d-band formation, metal-insulator transition, textured phases of electronic condensates and superconductivity have emerged. TMDs have the chemical formula MX_2, where M is a transition metal, and X represents a chalcogenide atom. The quasi-two-dimensional character of layered TMDs is a consequence of their electronic structure. Each layer has a sandwich-like crystal structure of the X-M-X form, where a plane of transition metal atoms is arranged between two planes of chalcogenide atoms. Layers are generally considered to be weakly coupled to each other by van der Waals bonds. There are several stacking arrangements of the layers, referred to as polytypes: 1T, 2H, 3R, 4Ha, 4Hb or 6R. The number in the notation says how many layers are there in a unit cell, and T, H, and R denote trigonal, hexagonal and rhombohedral symmetries, respectively. This thesis will deal with the 1T-polytype TMDs.

TMDs are particularly noted as quasi-2D electronic materials that first widely exhibited CDW transitions. In some cases, these have been thought as the first direct generalizations of the CDW Peierls mechanism, previously observed at work in quasi-1D electron systems (chain compounds). However, other mechanisms have also been proposed in cases where Peierls mechanism is not well grounded, and the mechanism behind the transition is still unresolved in some materials. This includes 1T-$TiSe_2$, where the mechanism of instability is under hot debate. The case of 1T-TaS_2 is still not fully resolved either, although the mechanism of CDW formation is at least generally understood in this compound.

Analysis done on two members of the TMD family, 1T-TaS_2 and 1T-$TiSe_2$ will be shown here. Layered materials have held the interest of condensed matter physics for decades by exhibiting CDW, Mott insulator state, mixed phases or superconductivity. 1T-TaS_2 has it all in one package. Moreover, 1T-TaS_2 is the only TMD material known to exhibit the Mott phase. Although it has been studied for quite some time, this material still had some surprises. This work will show the signatures of the “localized surface plasmon” mode in the optical data, for the first time arising in an electronic crystal self-organized at nano-scale. This thesis will also show the analysis which enables the extraction of charge redistribution information induced by superstructuring for a commensurate layered material. 1T-$TiSe_2$ might have just a slightly less complicated phase diagram than the 1T-TaS_2, but it grabs the attention as a contender for the title of the first experimentally observed excitonic insulator.

Effects of the lattice superstructuring on optical and transport properties of pure and doped samples of 1T-TaS_2 and 1T-$TiSe_2$ are emphasized in the thesis. These two members of the TMDs show how a very simple layered structure can result in a very complex weave of different electronic phases. The state-of-the-art measurements are followed by an analysis and modeling which for the first time identify the spectral consequences of the effectively nano-composite nature of the nearly commensurate charge density wave phase of 1T-TaS_2 and show the procedure for extracting the charge redistribution information from the optical infrared phonon modes of the commensurately superstructured 1T-TaS_2. Analysis of the measurements on 1T-$TiSe_2$ resolves the contribution of electron and hole pockets in the low-frequency optical response in the normal phase. Spectral weights and scattering rates for each channel are determined. This analysis not only allows for the calculation of the charge carrier density and carrier mass with a greater precision, but also enables the determination of the nature of the normal phase and sets the stage for the charge density wave transition. Work done on building a setup for measurements of transport properties under a high magnetic field and some early measurements are also presented in light of further investigation of layered materials, particularly TMDs. Specific issues related to the measurements are addressed.

This thesis contains 7 chapters. **Chapter 1** gives an introduction to the field of layered transition metal dichalcogenides, and a quick review of the theoretical models needed. Wider theoretical background, if deemed necessary to understand the work presented in the main body, was placed in Appendices. Some technical details were however kept in the introduction to equip the reader not familiar with the field with basic tools needed to access the heart of the matter. **Chapter 2** gives an overview of the experimental methods used. **Chapter 3** gives an overview of the previous work on pure and doped 1T-TaS_2, showing the structure and the numerous electronic phases this material exhibits. Results of our measurements of the electrical resistivity and optical reflectivity of pure and doped 1T-TaS_2 are presented. Optical conductivity obtained from the measured reflectivity and basic data analysis is shown. **Chapter 4** introduces the consequences of the nano-textured nearly commensurate phase of 1T-TaS_2. The need for the effective medium theory in the analysis of the optical data is shown.

Bruggeman effective medium theory as the tool of choice is introduced and novel results, developed using the 2-component and 3-component effective medium theory, are presented. **Chapter 5** introduces the effects of refolding on the optical spectra. The novel extraction procedure for the charge redistribution information using the spectral weight of the infrared phonons brought on by the deformation is explained on 1T-TaS$_2$. Analysis on both pure and doped 1T-TaS$_2$ is presented. **Chapter 6** introduces the previous work on 1T-TiSe$_2$, comparing the similarities and glaring differences between 1T-TiSe$_2$ and 1T-TaS$_2$. Our measurements of the electrical resistivity and optical reflectivity of pure and doped 1T-TiSe$_2$ are presented, as well as the calculated optical conductivity. Necessity of using a two-band model in the analysis of the low frequency optical data is demonstrated through Kramers-Kronig consistent fits to the experimental data of the pure sample in the normal phase. The two bands are identified as optical responses of an electron pocket and a hole pocket. Spectral weights determined through our two-band model of the low-frequency optical data enable us to determine the band width of the hole band. We demonstrate that this band alone is already too wide to enable thermal population at 290 K, thereby discarding the semiconductor description of the normal phase of 1T-TiSe$_2$ in favor of the semimetal with a band overlap. **Chapter Conclusions** brings the conclusions of the thesis.

Appendix A gives an overview of the optical properties and relations relevant to the experimental procedures and models used in the thesis. **Appendix B** gives an introduction to the Bruggeman effective theory used in the analysis of the experimental data.

The Summary of the thesis in Croatian is given in **Sažetak**. **Bibliography** is located at the end of the thesis.

1.2. Important relations in optics

1.2.1. Drude-Lorentz model

Seeing how analysis of the optical experimental data represents a corner stone of this thesis, some important relations used will be reviewed here. For a more detailed introduction to optical properties of solids turn to Appendix A.

The optical observable actually measured in this work was normal-incidence reflectivity of a sample. While we can draw some conclusions from the reflectivity, it is standard practice to calculate optical conductivity using the Kramers-Kronig analysis [Dressel2003, Kittel1996, Landau1960]. This procedure yields both the real and imaginary part of the complex optical conductivity $\sigma(\omega) = \sigma_1(\omega) + i\sigma_2(\omega)$.

Optical properties of a material can in many cases be modeled within a simple Drude-Lorentz model [Dressel2003]. The Lorentzian has the form (SI units)

$$\sigma(\omega) = \frac{\varepsilon_0 \omega_p^2 \omega}{i(\omega_0^2 - \omega^2) + \omega\Gamma} = \varepsilon_0 \omega_p^2 \omega \frac{\omega\Gamma - i(\omega_0^2 - \omega^2)}{(\omega_0^2 - \omega^2)^2 + \omega^2\Gamma^2}$$

where $\varepsilon_0 = 8.8542 \times 10^{-12}\ \mathrm{AsV^{-1}m^{-1}}$ is the dielectric constant of vacuum, ω_p is the "plasma frequency", ω_0 is the resonant frequency and Γ is the width (or scattering rate, as $\Gamma = 1/\tau$, where τ is the relaxation time) of the Lorentzian peak. Lorentzian is usually used to describe interband excitations. This is enough to model the optical properties of most standard semiconductors, but for metals we also need to model the intraband excitation. This can be achieved with the Drude term, which can be simply derived from the Lorentzian term by setting $\omega_0 = 0$. For a metal, the plasma frequency ω_p can be expressed as

$$\omega_p = \sqrt{\frac{ne^2}{m\varepsilon_0}} = \sqrt{\frac{\sigma_{dc}\Gamma}{\varepsilon_0}}$$

where n is the charge carrier density, e is the charge of an electron, m is the mass of an electron (or the effective mass if effects of a non-simple Fermi surface geometry have to be considered) and σ_{dc} is the dc conductivity of the sample (i.e. the frequency dependent conductivity at $\omega = 0$). The meaning of ω_p is, of course, not quite the same in Drude and Lorentzian terms. The expression for ω_p given above is completely valid for Drude terms describing the metal low-frequency optical properties. There, charge density is the charge density of the free electrons (i.e. the electron plasma) as described in the Drude-Sommerfeld theory [Kittel1996, Ashcroft1976]. For Lorentzian terms describing intraband excitations, only the first relation holds, $\omega_p = \sqrt{ne^2/m\varepsilon_0}$, and the charge density n and effective mass m are connected to the dominant charge carriers of the modeled band.

Plasma frequency ω_p can be extracted from the spectral weight through a simple relation

$$SW = \int_0^\infty \sigma_1(\omega)d\omega = \frac{\pi\varepsilon_0}{2}\omega_p^2$$

1.2.2. Fano model

Asymmetric phonon modes are a constant fixture of this work. The standard way of modeling such peaks is given here.

In not so simple situations, e.g. when a narrow phonon mode is coupled to the wide background of electronic excitations, Fano model might be introduced. Fano peak is used to model the asymmetric phonon peaks deviating from the Lorentzian standardly used for the phonon optical response. Asymmetric phonon peak in the optical conductivity is expressed within the Fano model as [Fano1961, Dean2011, Thomsen1991]

$$\sigma(\omega) = \varepsilon_0\omega_p^2\left(1-\frac{i}{q}\right)^2\frac{\omega}{i(\omega_0^2-\omega^2)+\omega\Gamma} \tag{1.1}$$

where $1/q$ is the dimensionless Fano parameter giving the asymmetry of the mode. For $q \gg 1$, Fano peak approaches the standard Lorentzian, while for $q = 1$ the asymmetry is maximal. Fano effect is a general phenomenon that can be observed whenever discrete and continuous excitations interfere coherently. Ugo Fano actually proposed it to explain asymmetries in atomic absorption spectra [Fano1961]. Application of this formalism to an approximately flat continuum background interfering with a discrete phonon state can prove the existence of an intrinsic scattering background in the experimental spectra. It also proves that an interaction exists between the elementary excitation responsible for the background and those phonons which show the Fano effect. Spectral weight of a Fano peak can be determined using the expression [Cappelluti2012, DiPietro2014]

$$SW = \frac{\pi\varepsilon_0}{2}\omega_p^2\left(1-\frac{1}{q^2}\right) \tag{1.2}$$

1.2.3. Effective medium theory (EMT)

The basics of effective medium theory (EMT), primarily Bruggeman EMT, will be shown here. For a more detailed introduction to Bruggeman effective medium theory of solids turn to Appendix B. Further insights into the particulars of the used models will be presented as needed in Chapter 4 when we show that homogeneous models, such as Drude-Lorentz, are inadequate for the nano-textured room temperature phase of 1T-TaS_2.

Bruggeman EMT offers a symmetric treatment of the components of the composite, resulting in the percolation transition as the volume fraction of the components is changed. The general Bruggeman EMT equation governing the effective optical response of the composite is [Carr1985]

$$\sum_i f_i \frac{\varepsilon_i - \varepsilon_{eff}}{g_i \varepsilon_i + (1 - g_i)\varepsilon_{eff}} = 0$$

where summation goes over all components of the composite, f_i is the volume fraction, g_i is the depolarization factor and ε_i is the frequency dependent dielectric function of the *i*-th component, while ε_{eff} is the dielectric function of the composite. Depolarization factor introduces the effect of non-spheroidal grains.

The shortcomings of the Bruggeman EMT equation come from the fact that it can at most handle ellipsoidal grains. It will not reproduce the additional features that occur in the optical spectra of a composite due to the special, non-ellipsoidal, shape of the grains or features due to the interaction of clustered small grains. However, Bruggeman EMT can at least give a rough model of the complex composite, capturing its general features.

We can calculate both the effective conductivity and reflectivity from the solution to the above Bruggeman equation and ensure the self-consistency of our fits by fitting simultaneously to the reflectivity experimental data and optical conductivity data obtained from the measured reflectivity using the Kramers-Kronig analysis.

1.2.4. Localized surface plasmon

When optical response of a metal-semiconductor nano-composite is considered, localized surface plasmons become an unavoidable feature. As will be demonstrated in Chapter 4, this is exactly the case with the nearly commensurate CDW phase of 1T-TaS$_2$.

Plasmons are the eigenmodes of the collective oscillations of the "electron gas" (or "plasma") in metals. These oscillations will occur under different conditions in the cases of bulk material, planar metal-dielectric interface and metal particles. We distinguish these cases by referring to bulk plasmons, surface plasmon polaritons or localized surface plasmons (also called particle plasmons), respectively.

Bulk plasmon will always occur when a metallic material is in the presence of an electromagnetic field oscillating at the resonant frequency of the electron plasma. According to the Drude model, the free electrons will then oscillate 180° out of phase relative to the driving electric field. As a consequence, most metals possess a negative dielectric constant at optical frequencies, which causes, for example, a very high reflectivity. The quasi-free electrons that make up the electron plasma will start to oscillate with the frequency ω_p (A.9) in respect to the fixed positive ions that make up the crystal lattice. The only parameter that influences the plasma frequency is the electron density. Notice that the plasma oscillation is in the direction of the electric field and hence it defines a longitudinal mode. In reality, the plasma oscillation is damped due to electron–lattice collisions and also due to radiation losses [Novotny2012].

Surface plasmon polaritons (SPPs) propagate along the metal-dielectric interface, for distances on the order of tens to hundreds of microns, and decay evanescently in the z-direction with 1/e decay lengths on the order of 200 nm [Brockman2000, Knoll1998, Knobloch1993, Willets2007]. Figure 1.1 illustrates the difference between propagating SPPs and localized surface plasmons [Duyne2004, Haes2005, Kelly2003]. An important feature of SPPs is that for a given energy, the wave vector of the surface plasmon polariton is always larger than the wave vector of light in free space. The SPP dispersion asymptotically approaches the light-line for small energies. The physical reason for the large SPP momentum is the strong coupling between light and surface charges. The light field has to "drag" the electrons along the metal surface. Consequently, SPPs on plane interfaces cannot be excited by light of any frequency incident from free space. Excitation of SPPs by light is possible only if a wave vector component of the exciting light can be increased over its free-space value. There are several ways to achieve this increase of the wave vector component, all of which are beyond the scope of this work. For more information, see ref. [Novotny2012].

In the case of localized surface plasmons (LSPs), light interacts with particles much smaller than the wavelength the incident electromagnetic wave (Figure 1.1 b). This leads to a plasmon that oscillates locally around the nanoparticle with a frequency known as the LSPR (Localized Surface Plasmon Resonance) [Haes2005, Kelly2003].

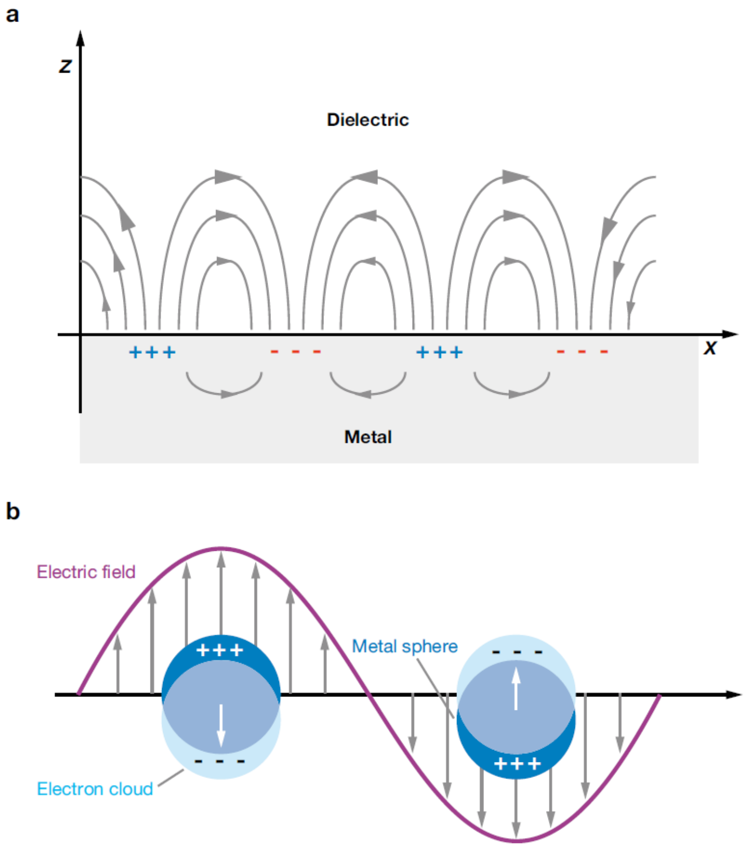

Figure 1.1. Schematic diagrams illustrating (a) a surface plasmon polariton (or propagating plasmon) and (b) a localized surface plasmon [Willets2007].

The power removed from the incident beam due to the presence of a particle is due to scattering and absorption. The sum of absorption and scattering is called extinction. If we look at spherical particles of radius a, it turns out that absorption scales with a^3, whereas scattering scales with a^6. Consequently, for large particles extinction is dominated by scattering, whereas for small particles it is dominated by absorption. This effect can be used to detect extremely small metal particles down to diameter 2.5 nm, which are used as labels in biological samples [Boyer2002]. The transition between the two size regimes is characterized by a distinct color change. For example, small gold particles absorb green and blue light and thus render a red color. On the other hand, larger gold particles scatter predominantly in the green and hence render a greenish color. A very nice illustration of these findings is the famous Lycurgus cup made by ancient Roman artists and is today exhibited at the British Museum, London. Today it is known that the colors displayed by the cup are due to nanometer-sized gold/silver particles embedded in the glass. The colors are determined by the interplay of absorption and scattering [Novotny2012].

For non-spherical particles, due to the broken symmetry, the degeneracy between collective electron oscillations along different directions is lifted. One way to obtain the plasmon resonances of non-spherical particles is to model them as prolate spheroids and to apply the quasi-static approximation [Johnson1972]. For strongly elongated particles the quasi-static approximation eventually breaks down.

Similar to the SPR (Surface Plasmon Resonance, the resonant frequency of the surface plasmon polariton), the LSPR is sensitive to changes in the local dielectric environment [Kelly2003, Knobloch1993, Jensen1999]. The role of size, shape, material and local dielectric properties on the LSPR wavelength has been extensively studied [McFarland2003, Haes2005, Kelly2003, Knobloch1993, Mock2002, Haynes2002].

Simple, highly symmetric structures, such as isolated spherical nanoparticles or nano rods, exhibit plasmon resonances that can easily be assigned to characteristic surface charge distributions. More complex structures, however, often yield multi-featured resonance spectra that are difficult to interpret at first sight [Michaels2000]. Moreover, clustering of nanoparticles and correlation between them can lead to even more complex plasmon spectra [Zeng1989, Auguie2008, Fischer2008, Lamprecht2000]. Coupling between the LSP response and a structureless background originating from interband transitions produces an asymmetric plasmon line shape [Pakizeh2009].

1.3. Superstructuring and charge density waves

Superstructuring brought on by charge density waves is an ever present theme in this work. Peierls transition is used to introduce the mechanism of charge density waves.

1.3.1. Peierls transition

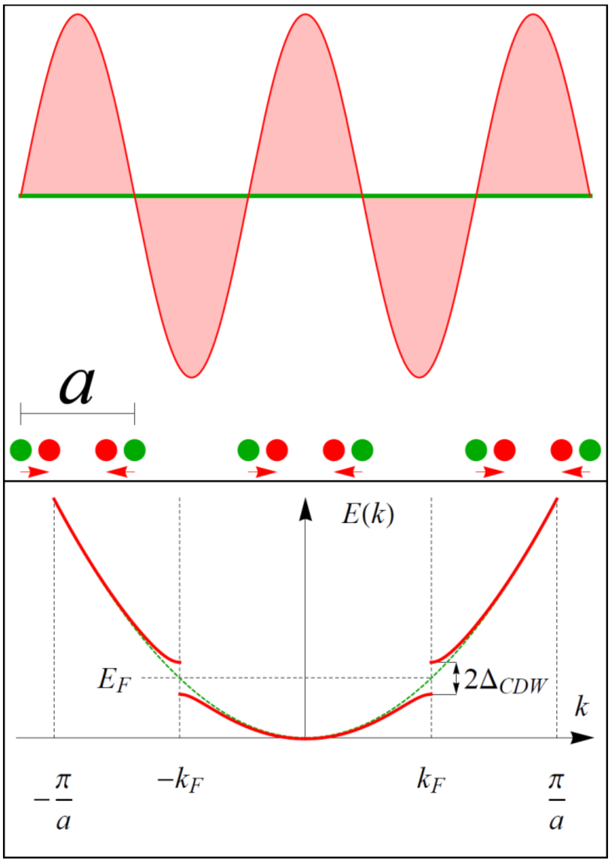

Figure 1.2. Upper panel is a sketch of the Peierls transition. Periodic crystal lattice with the period a (green disks) is deformed in such a way that effectively pairs of atoms are formed (red disks). These pairs form a regular superstructure with the period $2a$. The green line shows the uniform charge density distribution of the undeformed lattice, and the red line shows the charge density distribution of the deformed lattice. The lower panel shows a sketch of the gap opening at the Fermi level in the conductive band of the deformed lattice.

Perhaps the most graphic example of an effect connected to superstructuring is the Peierls transition. It denotes a so called charge density wave (CDW) enabled by the superstructuring of the crystal lattice. Imagine a one-dimensional crystal in the form of a periodic chain of monovalent atoms with a period a (green disks in Fig. 1.2) at temperature T = 0 K. It was suggested by Peierls that such a lattice is unstable with respect to a static lattice deformation of a wave vector equal to $2k_F$ [Peierls1955, Kittel1996], which acts as a so called nesting vector. This deformation would be visible as dimerization of the lattice, where pairs of atoms (dimers) would come closer to each other (red disks in Fig. 1.2). The dimers form a periodic superstructure with a period $2a$. The new arrangement of atoms is accompanied with a periodic modulation of the charge density known as a charge density wave. The charge density of the CDW is given by

$$\rho(\boldsymbol{r}) = \rho_0 + \rho_1 \cos\left(2\boldsymbol{k}_F\boldsymbol{r} + \varphi\right)$$

where $\boldsymbol{r}$ is a real space position, ρ_0 is the unperturbed electron density of the metal, ρ_1 is the amplitude of the CDW, $\boldsymbol{k}_F$ is the Fermi vector and φ is the phase of the CDW [Grüner1988].

Deformation of the crystal lattice costs elastic energy. How can this be energetically favorable for the crystal? The system gains energy because the deformation of the lattice opens a gap at the Fermi level. As can be seen from Figure 1.2, this effectively lowers the electronic energy states leading to a minimum in the total energy of the system. In other words, in a 1D metal at low temperature the elastic energy cost to produce the periodic lattice deformation is less than the gain in the conduction electron energy.

Even this rudimentary explanation points to the character of the Peierls transition, namely it is a metal-insulator (or a metal-semiconductor) transition. We have assumed that the undeformed lattice was composed of monovalent atoms, meaning that in the free electron model we assume to have one "free" or nearly free electron per atom. This in turn means that we have a half-filled conductive band, leading to metallic behavior. Gap opening at Fermi level creates two sub-bands, one of which is full and one empty, divided by a gap. This leads to insulating or semiconducting behavior, depending on the gap width.

Increasing temperature leads to the reduction of the gap [Kuper1955] and magnitude of the lattice deformation and eventually to the transition at the so called Peierls temperature. The material is a metal above the transition temperature while it is an insulator (semiconductor) with a temperature dependent gap below it.

Two-dimensional materials may present CDW instabilities when favorable nesting conditions of the Fermi surface occur. In fact, CDW states were first unambiguously observed by diffraction experiments on two-dimensional TMDs [Wilson1975, Hughes2001].

The study of Peierls transition in two dimensions is not as straightforward as in one dimension because both Fermi surface and lattice deformations are more complex. As shown in Figure 1.3, 1D case enables perfect nesting where the whole Fermi surface can be simply translated with a single wave vector. In the 2D case, The Fermi surface is (in the simplest case) a cylinder and nesting is reduced to lines on opposite sides of the cylinder.

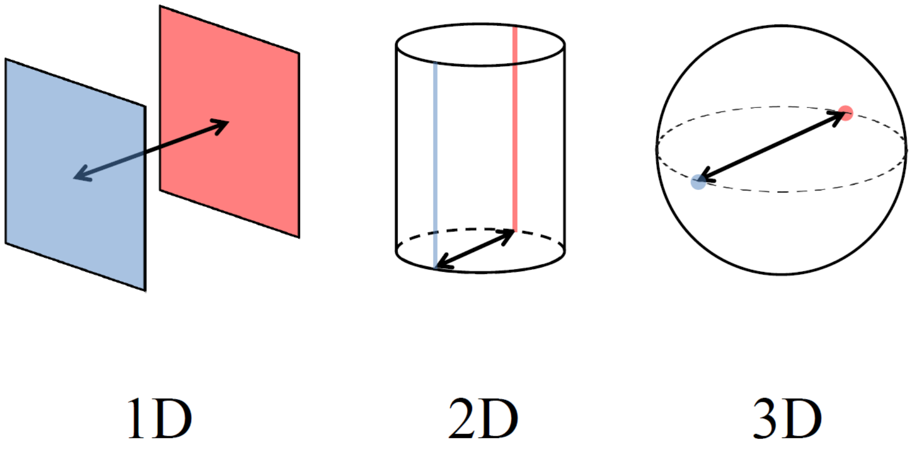

Figure 1.3. Fermi surfaces in a one-dimensional, two-dimensional and three-dimensional case. Arrows represent the nesting vector. Parts of Femi surfaces that can be nested by the same vector are colored blue and red. Note the drastic reduction of the nested surface in the 2D case, so called "imperfect nesting". In 3D only two points, on opposite sides of the Fermi surface sphere can be nested by one vector.

1.3.2. Kohn anomaly

The Peierls transition is a result of the coupling of electronic states near E_F, with collective vibrations of the lattice [Chan1973, Kohn1959, Smith1995]. Consequently, electron-phonon interaction is crucial. When the electrons in a metallic system are perturbed by some periodic potential, the electrons move to screen the applied potential. A measure of this screening is provided by the generalized susceptibility, $\chi_{\boldsymbol{q}}$, (where $\boldsymbol{q}$ is the wave vector associated with the periodic potential). $\chi_{\boldsymbol{q}}$ (also called Lindhard response function) is given by the expression

$$\chi_{\boldsymbol{q}} = \sum_{\boldsymbol{k}} \frac{f_{\boldsymbol{k}} - f_{\boldsymbol{k}+\boldsymbol{q}}}{\varepsilon_{\boldsymbol{k}+\boldsymbol{q}} - \varepsilon_{\boldsymbol{k}}} \tag{1.3}$$

$f_{\boldsymbol{k}}$ is the Fermi-Dirac function and $\varepsilon_{\boldsymbol{k}}$ is the energy for a state with wave vector $\boldsymbol{k}$. $f_{\boldsymbol{k}} - f_{\boldsymbol{k+q}}$ is then the difference in the occupation number of two states separated by the wave vector $\boldsymbol{q}$ [Kevan1991]. As is evident in equation (1.3), the susceptibility will become singular if $\varepsilon_{\boldsymbol{k}} = \varepsilon_{\boldsymbol{k+q}}$. This is precisely what occurs if $\boldsymbol{q} = 2\boldsymbol{k}_F$, where $\boldsymbol{k}_F$ is the Fermi wave vector of the Fermi surface (when $\boldsymbol{q} = 2\boldsymbol{k}_F$, $\boldsymbol{q}$ is said to be a nesting vector of the Fermi surface). The number of states coupled by the displacement vector $\boldsymbol{q} = 2\boldsymbol{k}_F$ is a function of the shape of the Fermi surface.

The Fermi surface of a 1D electron gas is simple. It consists of two points, one at $+k_F$ and one at $-k_F$ [Grüner1994]. Real crystals are quasi-one-dimensional, meaning they have many weakly interacting chains of atoms organized in a three-dimensional crystal lattice. The result of this is that the Fermi surface for a quasi-one-dimensional real crystal consists of two parallel sheets, one at $+k_F$ and one at $-k_F$ ($2k_F$ apart).

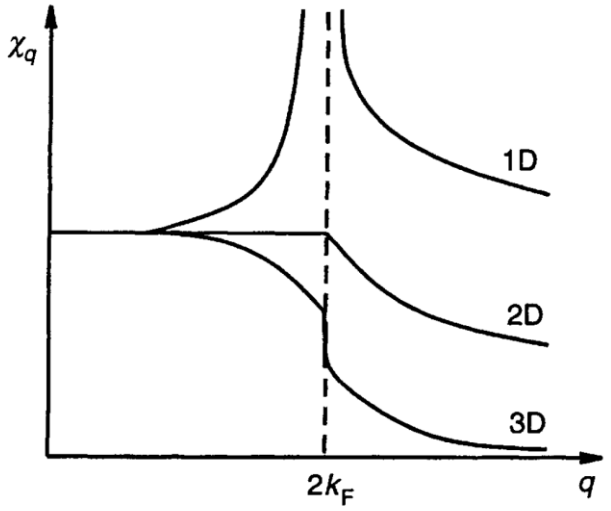

Figure 1.4. Susceptibility as a function of displacement vector $\boldsymbol{q}$. Note the singularity at $\boldsymbol{q} = 2\boldsymbol{k}_F$ [Smith1995].

Since in a quasi-1D metal the Fermi surface consists of two parallel sheets at $k = \pm k_F$, the displacement at $q = 2k_F$ couples all of the states at the Fermi surface, and the susceptibility diverges. This behavior is illustrated in Fig. **1.4**, which shows the singularity of χ in different dimensions [Schlenker1989, Rouxel1986].

When Fermi surface possesses parallel fragments such that many pairs of electronic states can be connected by the same wave vector ***q***, it is said to be “nested” and ***q*** is called the “nesting vector”. In general, the strength of the singularity in susceptibility depends on how heavily is the Fermi surface nested, i.e., how many states are coupled by a specific nesting vector ***q***.

The perturbing periodic potential (and thus the displacement vector ***q***) can be associated with a phonon in the lattice. However, since the atom cores vibrating in the phonon mode are interacting via the screened Coulomb potential, it is clear that if $\boldsymbol{q} = 2\boldsymbol{k}_F$, then the screening will become singular and the frequency of the phonon mode falls at this wave vector. This is the origin of Kohn anomalies observed in the phonon dispersion curves for metals [Kohn1959] where the frequency of the phonon mode associated with a specific wave vector is considerably lowered and there is a discontinuity in its derivative (see Fig. 1.5). In 1D and 2D systems, the singularity can be large enough to cause the frequency of the mode to fall to zero (a "giant Kohn anomaly"). If this occurs, a phonon is said to have frozen into the lattice, and the resulting static distortion is the periodic lattice deformation.

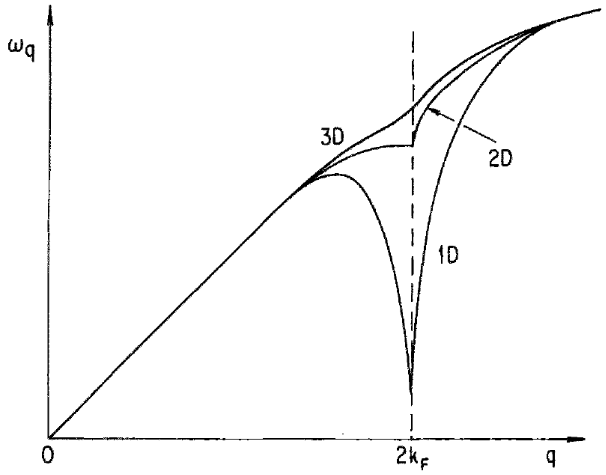

Figure 1.5. Kohn anomaly in the acoustic phonon dispersion in 1D, 2D, and 3D metals. [Grüner1994]

1.3.3. Collective modes

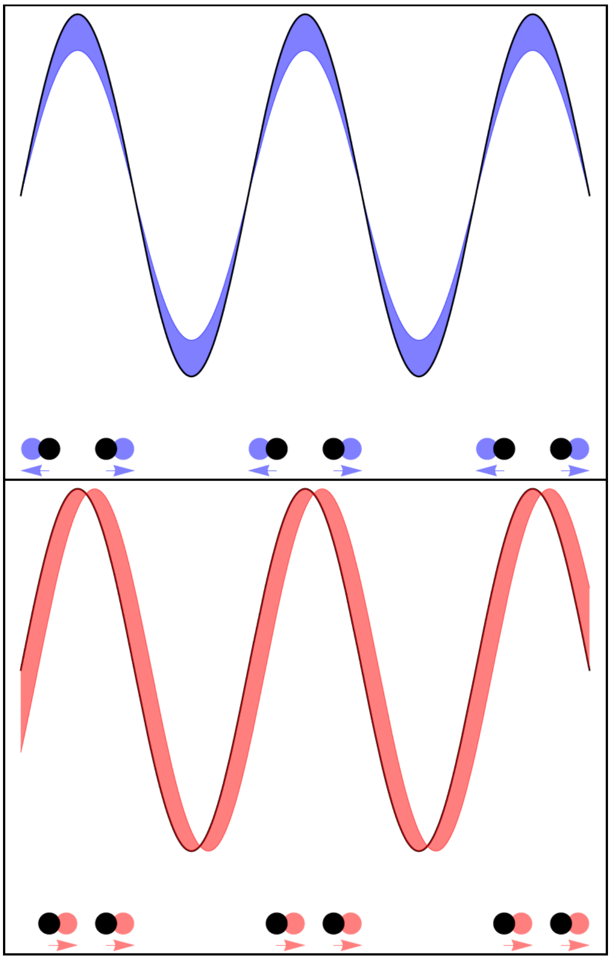

Figure 1.6. Collective modes. Top panel shows the "counter-phase" oscillations of the dimerazed atoms in a 1D lattice related to the amplitude oscillations of the CDW. Bottom panel shows the "in-phase" oscillations of the atoms related to the phase oscillations of the CDW. Note that the circles in the bottom of each panel do not show the real lattice distortions, only the phase of the oscillations.

It has been shown that a CDW in a perfect crystal has two modes of collective excitations called the amplitudon and the phason (Fig. 1.6) [Lee1974]. Amplitudon has a gap in the dispersion relation which cuts off the low frequency part of the dispersion, and phason is an acoustical mode which means that only the phason would be involved in the low frequency collective dynamical phenomena. For a real crystal which has defects, it has been shown [Lee1974] that the phason mode has a gap related to the mean pinning energy of the CDW.

Pinning potentials can be realized by anything from impurities to grain boundaries. Amplitudon is Raman active, while phason is infrared active [Grüner1994].

In real space, amplitudon is realized as an oscillation of the CDW amplitude, coupled to the "counter-phase" oscillations of the dimerized atoms of the 1D lattice. Phason is realized as a translation of the charge density, coupled to the "in-phase" oscillations of the dimerized atoms (Fig. 1.6).

1.3.4 Alternatives to Fermi surface nesting

While Fermi surface nesting is seemingly the most popular way of explaining the CDW mechanism, it is by no means the only one available. When discussing CDW in 1T-TiSe$_2$ for example, two other candidates become the front runners: band-type Jahn-Teller effect [Hughes1977, Rossnagel2002] and excitonic insulator model [DiSalvo1976B, Cercellier2007].

Band-type Jahn-Teller effect can manifest itself if the ground state electronic configuration of a nonlinear complex is orbitally degenerate and asymmetrically filled, in which case the complex distorts so as to remove the degeneracy and achieve a lower energy [Shriver1999]. The essential point, pertaining to 1T-TiSe$_2$, is that the overall density of states of the d_{z^2} band is slightly lower for trigonal prismatic than for octahedral coordination [Hughes1977]. The upper and lower faces of the selenium octahedra are rotated in opposite directions which leads to a symmetry break and a shift of the Ti 3*d* band towards lower energies.

Excitonic insulator phase can occur in a semimetal with a small band overlap or a semiconductor with a small gap [Jerome1967]. At low enough temperatures, electron-hole pairs (excitons) form if the binding energy of an exciton is bigger than the gap and Coulomb screening is weak due to a low charge carrier density. The new ground state is insulating because the binding energy of the excitons has to be overcome to allow conduction. The modulation of the charge density here is a consequence of the non-zero momentum of the excitons connecting the hole band maximum with the electron band minimum.

Chapter 2

EXPERIMENTAL METHODS

In this thesis, we present optical measurements of reflectivity in the frequency range 30 cm^{-1} to 37000 cm^{-1}, on pure and doped 1T-TaS_2 and 1T-$TiSe_2$. All optical measurements were done at the 1. Physikalisches Institut of the Universität Stuttgart in Germany, in the group of Prof. Dr. Martin Dressel. The Fourier Transform Infrared Spectroscopy measurements covered the frequency range from 30 cm^{-1} to 6000 cm^{-1}, while spectroscopic ellipsometry measurements covered the frequency range from 6000 cm^{-1} to 37000 cm^{-1}. Electrical dc resistivity measurements were made on the same samples in the group of Dr. Ana Smontara at the Laboratory for the physics of transport phenomena of the Institute of Physics in Zagreb, Croatia.

2.1. Optical measurements

This chapter aims to bring to light the basic measuring principles and techniques used in the measurements presented in this thesis. For a more detailed description of optical measurement methods, consult references [Dressel2003] and [Herres1984].

If the wavelength of the incident electromagnetic waves is much smaller than the sample size, the considerations of geometrical optics apply and diffraction and boundary effects become less important. Standard power reflection measurements are performed in an extremely wide frequency range, from millimeter waves up to the ultraviolet (between 1 cm^{-1} and 10^6 cm^{-1}). They are probably the single most important technique of studying the electrodynamic properties of solids.

Although tunable monochromatic radiation sources are available in the infrared, visible, and ultraviolet frequency range, it is more common that broadband sources are used and dispersive spectrometers (grating and prism spectrometers) are employed to select the required frequency. For the latter case, either a certain frequency of the radiation is selected (by dispersing prisms or by utilizing diffraction gratings) which is then guided to the specimen, or the sample is irradiated by a broad spectrum but only the response of a certain frequency is analyzed. Combined with suitable detectors the relative amount of radiation at each frequency is then recorded.

Optical experiments are in general performed in a straightforward manner by measuring, at different frequencies, either the reflectivity or transmission. The combination of different techniques then allows one to calculate the reflectivity $R(\omega)$ over a broad spectral range.

Beyond the spectral range in which measurements have been performed, suitable extrapolations are necessary, the choice being guided by the information available on the material. For metals, the Hagen–Rubens behavior of the reflectivity is a good approximation at low frequency, where $R(\omega) = 1 - \sqrt{8\varepsilon_0\omega/\sigma_{dc}}$ (Appendix A, relation (A.12)). Semiconductors and insulators have a constant reflectivity for $\omega \to 0$. At very high frequencies the reflectivity eventually has to fall to zero. Usually a ω^{-2} or ω^{-4} behavior is assumed in the spectral range above the ultraviolet. Then with $R(\omega)$ known over the entire range of frequencies, the Kramers–Kronig analysis [Dressel2003, Kittel1996, Landau1960] can be performed.

We always deal with complex response functions when describing the response of a system to a certain excitation. It always contains possible dissipation and some phase change. General considerations, involving causality, can be used to derive important relations between the real and imaginary parts of the complex response functions. They were first given by Kramers [Kramers1926] and Kronig [Kronig1926], and play an important role. These relations are also of great practical importance: they allow for the evaluation of the components of the complex dielectric constant or conductivity when only one optical parameter such as the reflected or absorbed power is measured. With reflectivity $R(\omega)$ obtained over a broad frequency range, the dispersion relations can be utilized to evaluate the phase change $\phi_r(\omega)$. There are two restrictions of practical importance: the data have to cover a wide spectral range and the sample must not be transparent. For a detailed derivation of the Kramers-Kronig relations, see [Dressel2003].

If we define a complex response function $\chi(\omega) = \chi_1(\omega) + i\chi_2(\omega)$, Kramers-Kronig relations will be

$$\chi_1(\omega) = \frac{1}{\pi}\wp\int_{-\infty}^{\infty}\frac{\chi_2(\omega')}{\omega' - \omega}d\omega'$$

$$\chi_2(\omega) = -\frac{1}{\pi}\wp\int_{-\infty}^{\infty}\frac{\chi_1(\omega')}{\omega' - \omega}d\omega'$$

$\wp$ is the principal part of the integral, i.e. mathematically correct way to handle divergence at $\omega = \omega'$ by excluding an infinitesimally small region. Using the odd/even properties of integrals and some algebra, final practical relations can be obtained where we do not deal with the unphysical negative frequencies or the divergence at $\omega = \omega'$ [Mihaly2006]

$$\chi_1(\omega) = -\frac{2}{\pi}\int_0^\infty \frac{\omega'\big(\chi_2(\omega') - \chi_2(\omega)\big)}{\omega'^2 - \omega^2} d\omega'$$

$$\chi_2(\omega) = -\frac{2\omega}{\pi}\int_0^\infty \frac{\chi_1(\omega') - \chi_1(\omega)}{\omega'^2 - \omega^2} d\omega'$$

Complex reflection coefficient $\hat{r}$ can be written as

$$\ln \hat{r} = \ln\sqrt{R} + i\phi_r$$

where R is the reflectance measured in an experiment and ϕ_r is the phase shift of the reflected light. The phase shift can now be calculated as

$$\phi_r(\omega) = -\frac{2\omega}{\pi}\int_0^\infty \frac{\ln\sqrt{R(\omega')} - \ln\sqrt{R(\omega)}}{\omega'^2 - \omega^2} d\omega'$$

Now we can use the measured reflectivity and the phase shift to calculate the real and imaginary parts of complex optical conductivity or dielectric function (see [Dressel2003]).

2.2. Fourier Transform Infrared Spectroscopy

Fourier transform spectroscopy utilizes two beams of one broadband source and records the response of the material as a function of the difference in path lengths between the two arms; a Fourier transformation then leads to the frequency dependent response. The spectral limitations on the high frequency side are the timely stability of the setup and the intensity of the source. On the lower frequency side, diffraction of the beam due to the large wavelength limits the performance, and also the spectral intensity of the light source diminishes rapidly due to Planck’s law. Hence Fourier transform spectroscopy is mainly used in the infrared range [Dressel2003].

The heart of the optical apparatus in a Fourier Transform Infrared Spectroscopy (FTIR) spectrometer is the interferometer [Herres1984]. An idealized Michelson interferometer is shown in 2.1. Infrared (IR) light emitted by a source is directed to the beam splitter, which ideally allows half of the light to pass through while the rest is reflected. The reflected part of the beam travels to the fixed mirror over a distance L. It is then reflected back to the beam splitter with a total covered path of $2L$. The transmitted part of the beam travels to the movable mirror. The mirror can be moved back and forth so that the distance between the beam splitter and the movable mirror oscillates around *L* by the distance *x*. The distance *x* can be measured very precisely by sending a laser beam parallel to the IR beam. Since the frequency of the laser is very far in spectrum from infrared, it will not interfere with the measurement. Total path covered by the transmitted part of the beam is 2(*L*+*x*).

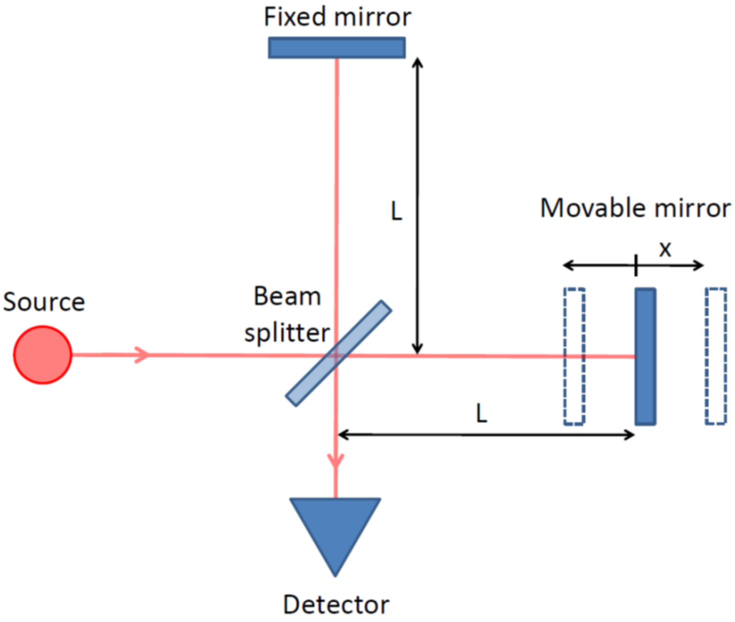
Fixed mirror
L
Movable mirror
x
Source
Beam splitter
L
Detector

Figure 2.1. Schematics of a Michelson interferometer.

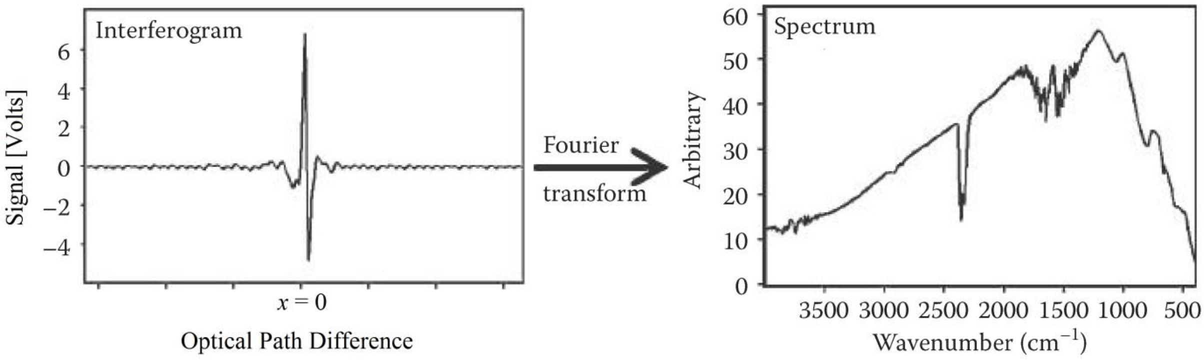

Figure 2.2. *Left*: an interferogram. Right: Frequency dependent spectrum calculated from the interferogram using Fourier transform. (Adapted from [Smith2011]).

The two halves of the beam recombine on the beam splitter with an optical path difference of $2x$. This produces the interference patterns called the interferogram. The recombined beam leaving the interferometer is passed through the sample compartment and then focused on the detector. The instrument measures the intensity of the recombined beam as a function of optical path difference. Depending on the optical path difference $2x$ relation to the wavelength of the light λ, the recombined beams can interfere constructively (for $2x = n\lambda, n = 0,1,2,\dots$), destructively (for $2x = (n + 1/2)\lambda, n = 0,1,2,\dots$) and something in between. For a monochromatic source, the interferogram would be a simple cosine with maximum in constructive and minimum in destructive interference points. For a polychromatic source, the interferogram is a sum of the interferograms for each individual frequency. This results in a central burst at $x = 0$ (because all wavelengths will have constructive interference there) and wings that quickly fall of to zero (see Figure 2.2, left panel). Fourier transform can now be used to convert the interferogram into the corresponding frequency dependent spectra (Figure 2.2, right panel). This procedure is standardly done using the specialized software packages that come with the measuring equipment. For this work Opus software was used, standardly delivered with the Bruker FTIR spectrometers.

The beam leaving the interferometer is reflected by the sample before reaching the detector. The sample will absorb light at some frequencies and this interaction can be detected by dividing the spectra reflected by the sample with the spectra of the original beam (usually gained by reflecting the beam from a gold or aluminum mirror).

During the measurements for this work, three FTIR spectrometers were used: Bruker IFS 66v/S, Bruker Vertex 80v and Bruker IFS 113v. Both Bruker IFS 66v/S and Bruker Vertex 80v were used in the mid-infrared (MIR) frequency range from 500 cm^{-1} to 8000 cm^{-1} with a resolution of 1 cm^{-1}. Exceptions are the measurements on the doped 1T-TaS$_2$ sample (d-TaS$_2$), where resolution of 0.5 cm^{-1} was used. Measurements in the frequency range from around 700 cm^{-1} to 6000 cm^{-1} were used for the final joined reflectivity curves. For MIR measurements, spectrometers were always equipped with a Bruker HYPERION IR microscope. To enable temperature dependent measurements, cold finger MicroVac cryostat was used for reflection measurements with the HYPERION IR microscope. This small-size cryostat is designed to fit under the IR microscope. In this way, temperatures between 300 and 10 K can be achieved [PI1-Web-FTIR]. The cryostat is equipped with a KBr window to enable optical measurements. The light from an infrared source integrated into the microscope is reflected at normal incidence from the sample (spot size 30 to 40 μm). The reflected beam is guided back through the microscope to the interferometer, and finally detected with a nitrogen-cooled bolometer. The measurement and result imaging is automated using the Opus software package. The measurement is repeated at the same temperature on an aluminum reference mirror (also at normal incidence). Ratio of sample signal and the reference signal then produces the sample reflectivity.

The Bruker IFS 113v spectrometer was used in two configurations (involving two different bolometer detectors) to cover the far-infrared (FIR) frequencies from 10 cm^{-1} to 800 cm^{-1} with a resolution of 0.24 cm^{-1}. The spectrometer was equipped with a modified CryoVac cold finger continuous-flow cryostat for reflectivity measurements with *in-situ* gold evaporation. The cryostat can be operated between 5 and 300 K [PI1-Web-FTIR]. It allows very precise measurements of the reflection by employing the double referencing method. In the first run reflectivity of a sample and a stainless steel reference mirror, both mounted on a brass cone, are measured. Then, we perform an *in-situ* evaporation of a gold film on the sample. In the second run reflectivity of the gold evaporated sample and the stainless steel reference are measured. Absolute values of reflectivity of the sample are calculated from the reflection data recorded for sample and reference in both runs.

2.3. Spectroscopic Ellipsometry

Ellipsometry measurements have been performed in collaboration with Mathias Eichler from the group of Prof. Dr. Martin Dressel at the 1. Physikalisches Institut of the Universität Stuttgart. Ellipsometry is based on the fact that different polarization states of an electric field, parallel (E_p) and perpendicular (E_s) to the plane of incidence, are reflected with different intensities [Dressel2003, PI1-Web-Ellipsometry]. The resulting polarization state is generally elliptic. This elliptically polarized light can be described via the so-called ellipsometric angles Ψ and Δ, which are defined by the complex Fresnel reflection coefficients. Δ corresponds to the phase shift of the electrical fields in p- and s-direction and tan Ψ describes the corresponding change of the amplitude ratios.

Today, most ellipsometers are based on a configuration with one rotating element. First, the unpolarized light coming from a light source is linearly polarized. Due to the interaction with the sample surface, the polarization state changes to elliptic. The rotating analyzer modulates the intensity of the reflected light with twice the rotation frequency. Via Fourier analysis of amplitude and phase of the detected signal the ellipsometric angles Ψ and Δ can be calculated.

In the simple case of bulk materials, where only the air-sample interface is considered, the optical constants can be directly calculated from the angles Ψ and Δ.

The ellipsometer used at 1. Physikalisches Institut, Universität Stuttgart, is a Variable Angle Spectroscopic Ellipsometer (VASE) from J. A. Woollam which allows a computer controlled variation of the angle of incidence.

2.4. Electrical resistivity

Electrical resistivity measurements were performed in collaboration with Dr. Petar Popčević from the group of Dr. Ana Smontara at the Laboratory for the physics of transport phenomena of the Institute of Physics in Zagreb, Croatia. The standard four-contact method was used. Here the two current leading wires are connected (using silver paste) to the opposite ends of a sample. One voltage probing wire is connected to the sample near each end (also using silver paste). With a known current through the sample, the voltage is read. The polarity of the current is then reversed and voltage again read. Polarity reversal is done to eliminate any errors due to the thermoelectric effects from the measurements, which would tend to add an offset to the voltage measurements. The correct resistance of the sample can then be determined as a simple arithmetic mean of the two resistances calculated using Ohm’s law.

$$R = \frac{R_+ + R_-}{2}, \qquad R_{+,-} = \frac{V_{+,-}}{I_{+,-}}$$

R is the sample resistance; $V_{+,-}$ and $I_{+,-}$ are the voltage and current for the two polarizations; $R_{+,-}$ is the resistance for the two polarizations. Resistivity can be calculated from resistance using the known geometrical factor of the sample from

$$R = \rho \frac{L}{A}$$

where ρ is the resistivity of the sample, L is the distance between the voltage probing wires and A is the cross-section area of the sample perpendicular to the current flow.

2.5. Samples

The measured single crystal samples were grown by Dr. Helmuth Berger at the École polytechnique fédérale de Lausanne (EPFL) and provided for this research by Prof. Dr. László Forró of the Laboratoire de Physique de la Matière Complexe at the EPFL. The samples include pure and doped single crystals of 1T-TaS_2 and 1T-$TiSe_2$. The doped sample of 1T-TaS_2 belongs to the same batch as the one whose properties have been reported in reference [Xu2010]. It is referred to as d-TaS_2 and, as reported in [Xu2010], it contains less than 0.1% copper. The doped sample of 1T-$TiSe_2$ is 1T-$TiSe_{2-x}Te_x$, where $x = 0.03$.

Chapter 3

SUPERSTRUCTURING OF 1T-TaS_2

3.1. The abundance of phases

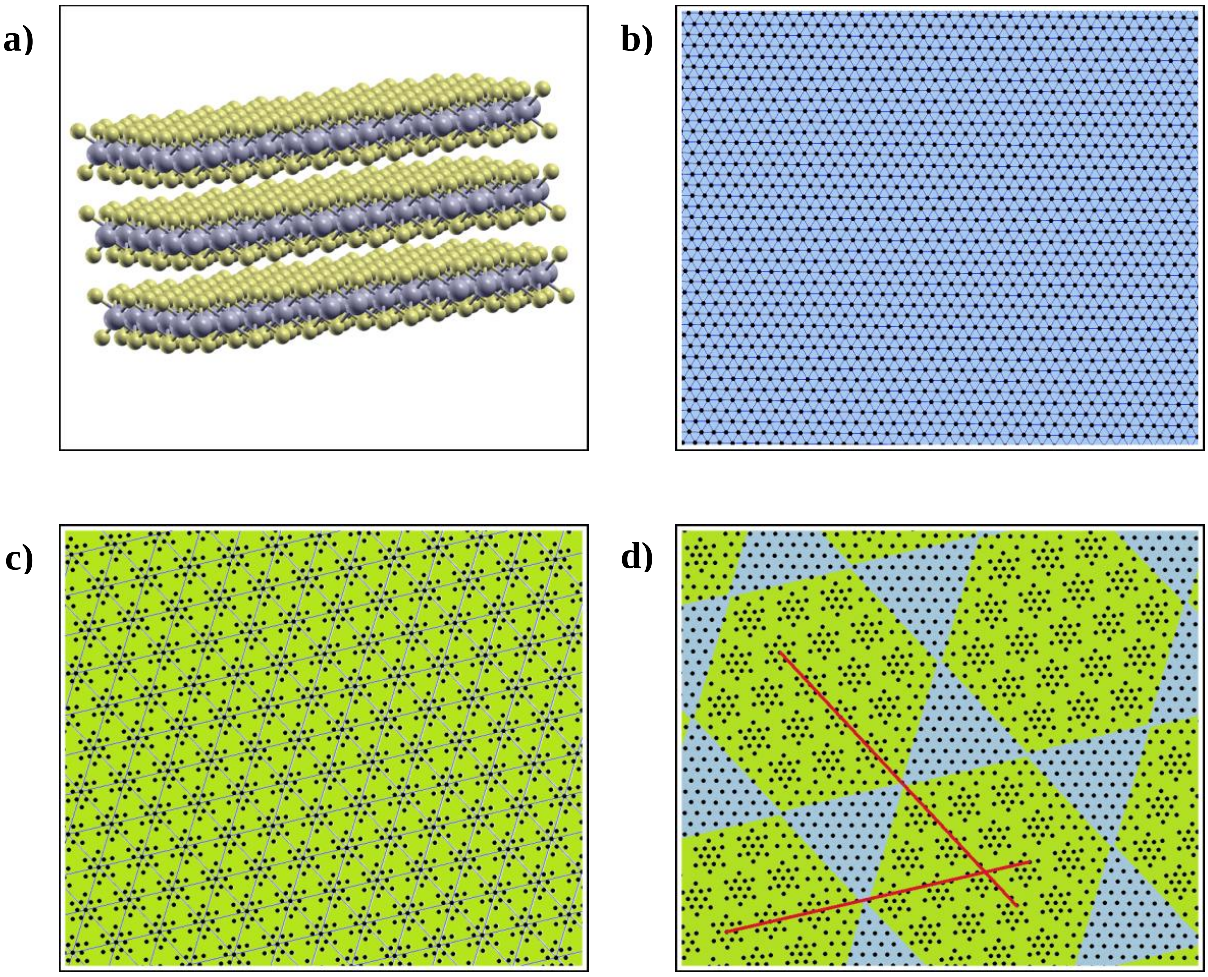

Figure 3.1. a) Layered structure of the 1T-TaS_2 crystal. Within each layer, a tantalum plane is sandwiched between two sulfur planes. b) In the metallic undeformed state, above 550 K, each layer has a hexagonal structure (only Ta atoms showed for clarity). c) At low temperatures, the sample is in a commensurate charge density wave (CCDW) state where one electron per star-like deformation is left above the charge density wave gap, and localizes through a Mott insulator state. Magnitude of the star-like deformation is exaggerated for effect. d) At room temperature, the sample is in a nearly commensurate charge density wave (NCCDW) state. A roughly kagome-like texture of semiconducting CCDW hexagons and metallic triangles is present. Red lines emphasize the phase slip between neighboring semiconducting domains [Wu1990, Thomson1994].

1T-TaS$_2$ is a layered material with strong covalent bonds within layers and standardly reported weak van der Waals bonds between layers (Fig. 3.1). It has been long known that this material has five temperature dependent phases, four of which support a charge density wave (CDW) [Wilson1975, Scruby1975, Bayliss1984, Thomson1994]. Recently a sixth, hidden, stable photoinduced phase has been reported [Stojchevska2014].

Parent phase of 1T-TaS$_2$, appearing only above 543 K [Bayliss1983], has a very simple structure. It features layers in which a perfectly planar hexagonal lattice of tantalum atoms, with each Ta atom in the center of an octahedron made of sulfur atoms. Lattice constants of the undeformed parent phase are $a = b = 3.36$ Å and $c = 5.90$ Å for the in-plane and out-of-plane lattice constants, respectively [Jellinek1962]. The parent phase is metallic in nature since each Ta atom has one 5*d* valence electron in a half-filled band [Rossnagel2006].

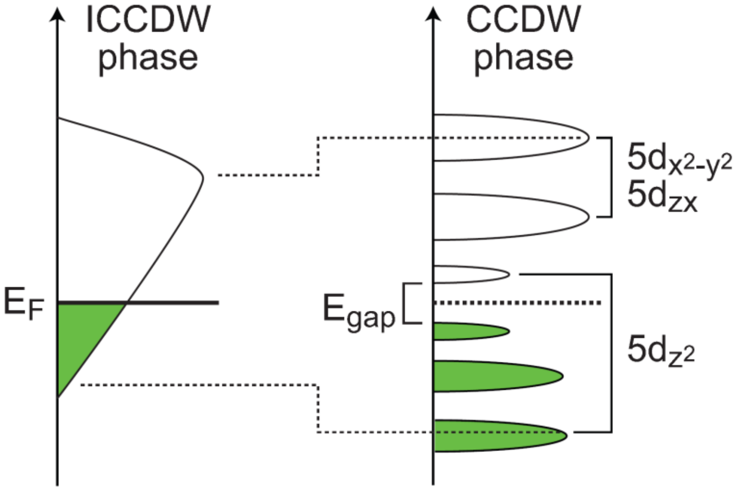

Figure 3.2. Schematic Ta 5*d* DOS model of 1T-TaS$_2$ in the ICCDW (left) and CCDW (right) phase. Due to the formation of the superstructure in the CCDW phase, the Ta 5*d* band splits into three bands both in occupied and unoccupied DOS. The Mott localization gap of ~200 meV opens centered at E_F. [Sato2014]

At low temperatures the sample is in a commensurate charge density wave (CCDW) phase with a periodic lattice deformation in the form of Star-of-David (SD) structure [Wilson1975, Thomson1988]. Each SD consists of 13 Ta atoms, with one central Ta atom and two concentric rings of six Ta atoms each around it. Stars show a superstructure with a $\sqrt{13}a \times \sqrt{13}a$ rotated unit cell, where a is the lattice constant of the undeformed 5*d* electron structure. Formation of the SD clusters also involves displacements perpendicular to the plane, causing a periodic swelling of the TaS_2 layers [Wilson1978, Bovet2003]. Density of states of the deformed system is gapped, with only twelve electrons of the new unit cell fitting bellow the gap. The 13th electron is left above the gap, in a half-filled sub-band at the Fermi level [Rossnagel2006]. This enables Mott localization in two dimensions [Fazekas1979, Fazekas1980], also confirmed by spectroscopic measurements [Pillo2000, Zwick1998] and scanning-tunneling microscopy (STM) [Kim1994]. Optical and angle-resolved photoemission spectroscopy (ARPES) measurements in CCDW phase [Gasparov2002, Pillo2001] show a gap on the order of 0.12 to 0.18 eV attributed to the Mott state [Manzke1989, Dardel1992]. Density functional theory (DFT) calculations give a gap of 0.125 to 0.15 eV [Freericks2009]. This is the only known case of Mott phase found in a TMD material.

At room temperature, the sample is in the mixed nearly-commensurate charge density wave (NCCDW) phase (Fig. 3.1 d). This is actually a super-superstructure of the CCDW phase. The NCCDW phase shows a texture of roughly hexagonal CCDW domains and undeformed (or much less deformed) triangles [Wilson1975, Wu1989, Thomson1994, Spijkerman1997]. When two periodic lattices with non-proportional periods are present in a system, the simplest solution is for the system to be in an incommensurate state. If there is some interaction between the periodic properties of the lattices, a solution in which two lattices become locally commensurate is possible. If the magnitude of terms in the free energy which determine the periodicities of lattices and the term that promotes their commensurability is favorable, the two lattices can become locally commensurate within domains and undergo phase slips at the domain walls [McMillan1976, Wu1990, Thomson1994]. The 13th electron, which localizes in the low temperature phase, now finds it energetically more favorable to transfer into the triangles. NCCDW phase of 1T-TaS_2 is characterized by a roughly kagome-like texture of semiconducting and metallic domains [Thomson1994, Spijkerman1997].

While this covers the phases relevant to this work, for the sake of completeness it is good to mention other phases of 1T-TaS_2. If the system is cooled below 550 K, before the transition into the NCCDW phase at 350 K, it will be in the incommensurate charge density wave (ICCDW) phase. If it is heated from the low temperature CCDW/Mott phase, at 220 K it will go into a striped phase, and then to NCCDW phase around 280 K. The most recently discovered stable phase is accessible only when the sample is exposed to femtosecond laser pulses at low temperatures, as described in reference [Stojchevska2014].

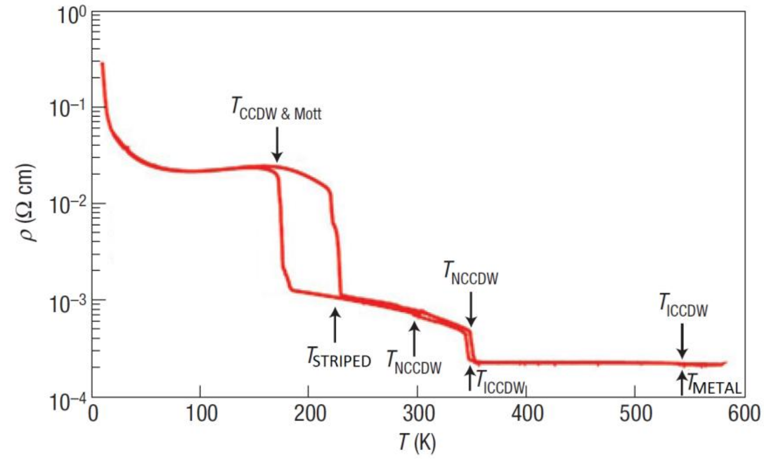

Figure 3.3. Temperature dependent resistivity of 1T-TaS$_2$ [Sipos2008]. Arrows above the resistivity curve mark the transitions in cooling: from metal phase to ICCDW phase at 550 K, NCCDW phase at 350 K and CCDW/Mott phase at 180 K. A wide hysteresis is clearly visible as the sample transitions from CCDW to striped phase at 220 K upon heating [Wilson1975, Thomson1994]. Arrows below the resistivity curve mark the transitions in heating: from CCDW/Mott phase to striped phase at 220 K, NCCDW phase at 290 K, ICCDW phase close to 350 K and metal phase above 550 K.

The multitude of phases in 1T-TaS$_2$ can be clearly seen in the temperature dependent resistivity in Figure 3.3 [Sipos2008]. As far as the NCCDW and CCDW phases are concerned, the most prominent features are the first-order phase transition and a wide hysteresis. In the NCCDW phase, non-metallic behavior can be seen. This behavior has been linked to the ordered array of the nano-composite consisting of metallic and semiconducting domains [Sipos2008, Spijkerman1997]. Here, narrow channels that connect the metallic areas are considered to be the main contributor to the scattering of the conductive electrons in dc measurements of electrical resistivity. As the temperature is lowered, the semiconducting domains grow [Thomson1994]. Since the ratio of metallic to semiconducting domain area is not changed in temperature [Ritschel2013], the metallic areas must also grow as the temperature is lowered. However, the shape of the semiconducting domains is expected to become increasingly closer to a regular hexagon, which would mean that the conducting channels are “pinched” at low temperatures. This causes the increase in the scattering rate.

At 180 K in cooling, there is a first-order transition to a CCDW/Mott phase. Below the transition temperature, metallic-like behavior of the resistivity can be observed (Fig. 3.3, Fig. 3.7). This has been linked to the possibility of an incomplete Mott gap [Mott1974, Dardel1992, Bovet2003]. As the temperature is lowered, the deep pseudogap formed by the overlapping tails of the Hubbard subbands [Mott1974] is bound to give rise to disorder-driven localization which prevents metallic conduction. Bovet has explained the metallic temperature behavior just below the Mott transition as a consequence of remaining midgap states [Bovet2003].

Optical properties of 1T-TaS$_2$ have been studied extensively in a broad temperature and frequency region [Benda1974, Beal1975, Barker1975, Bayliss1983, Gorshunov1986]. With the advancement of the equipment resolution, the study of the phonon modes was enabled [Karecki1979, Uchida1981, Gasparov2002].

Optical measurements presented in this thesis present state-of-the-art reflectivity measurements with a high resolution. For an introduction to the optical properties of materials see Appendix A. The experimental methods are given in Chapter 2 and only results will be presented here. The measured reflectivity of pure 1T-TaS$_2$ is shown in Figure 3.4.

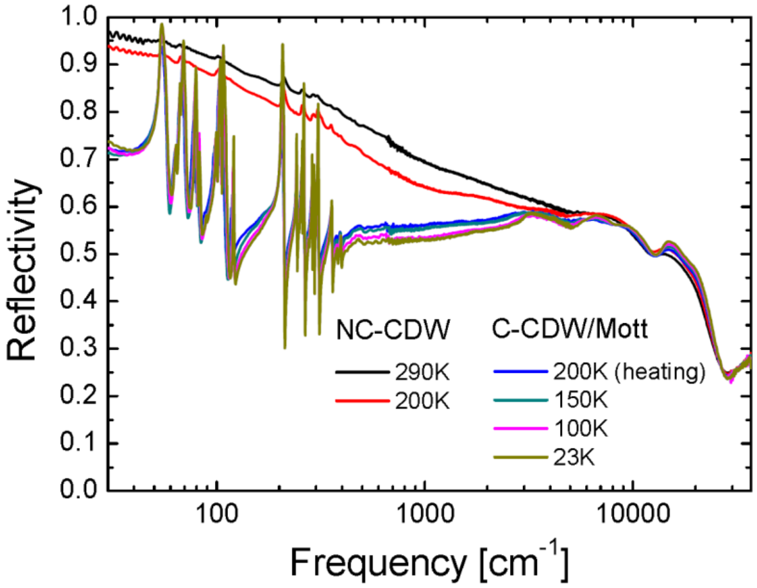

Figure 3.4. Frequency and temperature dependent reflectivity of the pure 1T-TaS$_2$ in the frequency range 30 cm^{-1} to 37000 cm^{-1}. All measurements were taken in cooling except for one curve at 200 K which was taken in heating. Curves taken at 290 K and 200 K (black and red curves, respectively) belong to the NCCDW phase. They are clearly separated from the rest of the curves which belong to the CCDW-Mott phase.

The figure clearly shows the separation of the room-temperature NCCDW and low temperature CCDW phase reported in [Karecki1979]. The rise of reflectivity with temperature in the NCCDW phase is consistent with the non-metallic slope of the resistivity measurements shown in Figure 3.3, but this is in contrast to the metallic Drude-like shape and high reflectivity of the NCCDW curves. This is an optical “clue” of the complexity of the nano-composite NCCDW phase. Phonon modes are much smaller than the ones in the low-temperature phase, but still clearly visible. Phase transition to the CCDW phase is accompanied by a significant drop in reflectivity below 3000 cm^{-1}. This is expected as the sample enters the Mott insulator state, but the reflectivity is still quite high, with a hint of Drude-like behavior of the low-frequency spectra. Electronic background of the spectra, generated by the intraband transitions, is obscured by the phonon-related deformations of the reflectivity curves, preventing any strong conclusions. The spectra between 50 cm^{-1} and 400 cm^{-1} are dominated by prominent phonon peaks.

Real part of the optical conductivity calculated using the Kramers–Kronig analysis [Dressel2003, Kittel1996, Landau1960] is shown in Figure 3.5.

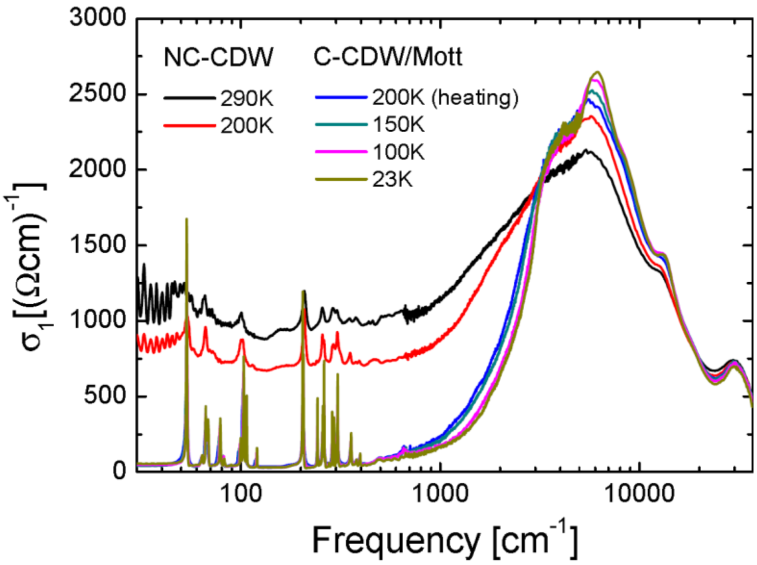

Figure 3.5. Frequency and temperature dependent real part of optical conductivity in the frequency range 30 cm^{-1} to 37000 cm^{-1}. All curves belong to measurements done in cooling unless otherwise stated.

Gasparov has previously reported the optical conductivity of the pure 1T-TaS_2 [Gasparov2002], albeit with a coarser resolution and less precision compared to the measurements presented in this work.

Optical conductivity reveals that the low temperature phase, even though it is nominally a Mott insulator phase, shows a small dc conductivity of 50 $(\Omega cm)^{-1}$ as estimated from the conductivity at the lowest measured frequency. This is of the same order of magnitude as the CCDW sub-millimeter conduction of 30 $(\Omega cm)^{-1}$ determined by [Gorshunov1986]. The origin of this small conductivity could be the high (26-fold!) degeneracy of the star-like deformation which inevitably leads to dis-commensurated domain walls between domains with non-matching CDW phase. This high degeneracy comes from the fact that prior to star-like superstructuring takes place, any one of the 13 unit cells that will make up the Star-of-David has an equal chance to become the center. After the center is fixed, the unit cells that will make up the star can still be chosen in two non-equivalent ways (hence, 26 fold degeneracy).

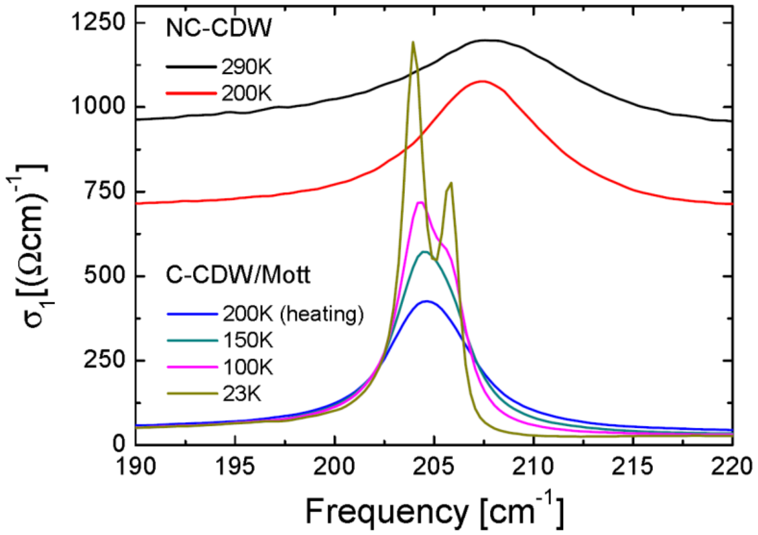

Figure 3.6. Additional phonon peak close to 200 cm^{-1} found in the CCDW/Mott phase.

Above approximately 800 cm^{-1} (close to 0.1 eV), spectra are dominated by the interband transitions. Below this, spectra are dominated by the two distinct groups of phonon modes appearing between roughly 50 cm^{-1} and 400 cm^{-1}. Simple mass-on-a-spring model of lattice vibrational modes tells us that in a two-atom system, the lower-frequency group should be related to the heavier atoms (i.e. tantalum because $m(Ta) \approx 5.6 \cdot m(S)$), while the higher-frequency group should be related to the lighter atoms (i.e. sulphur) [Gasparov2002].

Compared to [Gasparov2002], we show that the 205 cm-1 phonon at 30 K of Gasparov is actually composed of two phonons, clearly visible at low temperature (Fig. 3.6). We have determined the mode frequencies at 23 K to be around 204 and 206 cm-1. Higher frequency phonon, the „206 cm-1 mode“, is clearly discernible only at temperatures equal to or lower than 150 K, but fitting shows that it is present in the whole temperature range belonging to the Mott phase.

The NCCDW phase shows a more or less flat intraband with much wider phonons. Optical conductivity decreases as the temperature is lowered, similar to dc conductivity, with a large drop in conductivity of around 800 $(\Omega\mathrm{cm})^{-1}$ occuring at the Mott transition, measured at the frequency of 30 cm^{-1}.The same phonon modes seen in CCDW phase seem to be present in the NCCDW phase, but the widening of the phonon modes and the screening make it difficult to account for every peak. Over 800 cm^{-1} interband transitions very similar to the ones in the lower temperature phase can be seen, but with much greater widths.

3.3. Effects of doping and pressure

Pressure has been found to have a profound effect on the properties of 1T-TaS_2. CCDW transition can be completely removed by pressure, and NCCDW phase can be extended to the lowest temperatures [Sipos2008]. As soon as the fully commensurate CDW phase is suppressed, at 0.8 - 1 GPa, the sample will become superconductive. As the pressure is increased, all CDW phases are suppressed until the sample is in the parent metallic phase above 8 GPa according to [Sipos2008]. The remarkable insight of reference [Sipos2008] is that once the superconductivity is fully established in the NCCDW phase, the superconductive transition temperature will remain approximately constant around 5 K as the pressure is increased. This means that even though superconductivity originates in the NCCDW phase, the transitions from NCCDW phase to the metallic phase have absolutely no effect on superconductivity. The conclusion from [Sipos2008] is that domains very similar to the undeformed parent phase must be the ones that actually turn superconductive in the NCCDW phase, i.e. the metallic triangles. It has been noted by X-ray investigations under pressure [Ritschel2013] that there are actually traces of CDW still present in the metallic phase of [Sipos2008] from 8GPa to 25GPa. While this might hold, the character of the phase as seen in temperature dependent resistivity is clearly metallic and resistivity practically does not change in this enormous pressure range. In other words, the metallic phase accessed in [Sipos2008] is a good representation of the metallic triangles of the mixed NCCDW phase and very close to the ideal undeformed parent phase, a fact which will come in handy when we try to model the optical response of the NCCDW phase.

Optical measurements of reflectivity under pressure up to 1.4 GPa have been performed [Kezsmarki2007], showing the far-infrared (FIR) features of the pressure induced CCDW-NCCDW transition similar to the ones from the temperature induced transition.

Although doping and pressure are not directly interchangeable, they are often used as analogous. 1T-TaS$_2$ has been studied extensively by doping [Thomson1972, Wu1988, Tison2004, Benda1974, DiSalvo1975, Endo2000, Ang2013, DiSalvo1976A, Ko2011, Ang2012, Pettenkofer1994, Pettenkofer1991, Xu2010, Lahoud2014].

It has been shown that substitution of Ta by as little as 1% Ti [DiSalvo1975] or Fe [Ang2012] and S by 4% Se will completely suppress CCDW/Mott phase. Slight doping by less than 0.1% copper will have the same effect and allow the investigation of the NCCDW phase down to low temperatures [Xu2010] (Fig. 3.7).

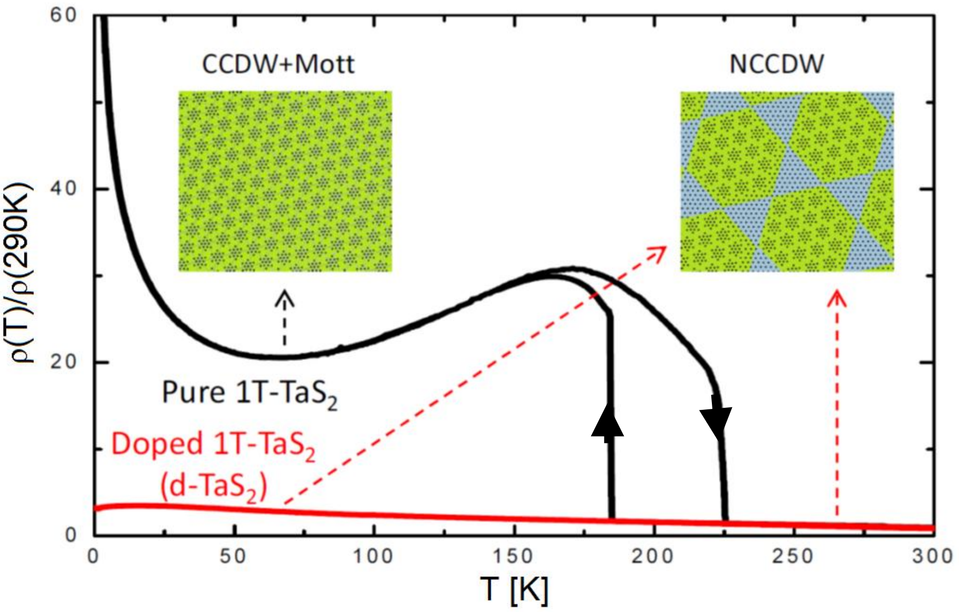

Figure 3.7. Temperature dependent relative resistivity of pure and slightly doped 1T-TaS$_2$. Resistivity measurements show that doping by less than 0.1% Cu completely suppresses the Mott transition and leaves the sample in the mixed NCCDW state down to low temperatures. This allows us to make a direct comparison of the phases at low temperatures. For previous report on the properties of samples from the same batch, slightly doped by copper, see [Xu2010].

The reference [Xu2010] uses samples from the same batch as the sample used in this work, so the analysis done there applies here too. We have taken the convention from [Xu2010] to refer to the slightly doped sample of 1T-TaS_2 as d-TaS_2.

Reflectivity measurements on the d-TaS_2 are shown in Figure 3.8. As already seen from the resistivity measurements, there is no phase transition, so the sample remains in the NCCDW phase at all measured temperatures. Low temperature measurements at 23 K show strong phonon modes very similar to the pure sample at the same temperature, albeit more dampened.

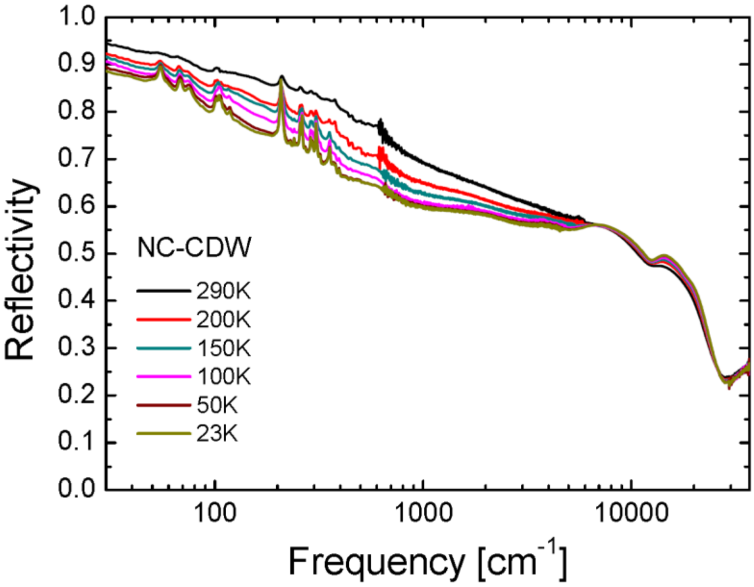

Figure 3.8. Frequency and temperature dependent reflectivity of the slightly doped 1T-TaS_2 (d-TaS_2) in the frequency range 30 cm^{-1} to 37000 cm^{-1}. All measurements were taken in cooling. There is no visible phase transition and all curves belong to the NCCDW phase.

Figure 3.9 shows the real part of the optical conductivity. As with the NCCDW phase in the pure sample, spectra seem to consist roughly from interband transitions at high frequencies and a sort of a quasi-Drude intraband at low frequencies.

Comparison of the relative dc conductivities obtained through transport measurements to the ones estimated from the optical measurements is shown in Figure 3.10. We can see that the relative conductivities agree quite well.

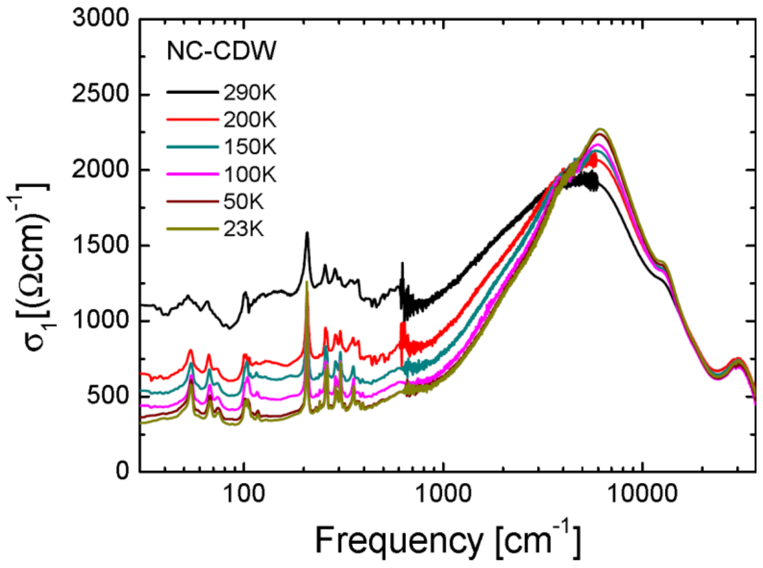

Figure 3.9. Frequency and temperature dependent optical conductivity of d-TaS_2 in the frequency range 30 cm^{-1} to 37000 cm^{-1}.

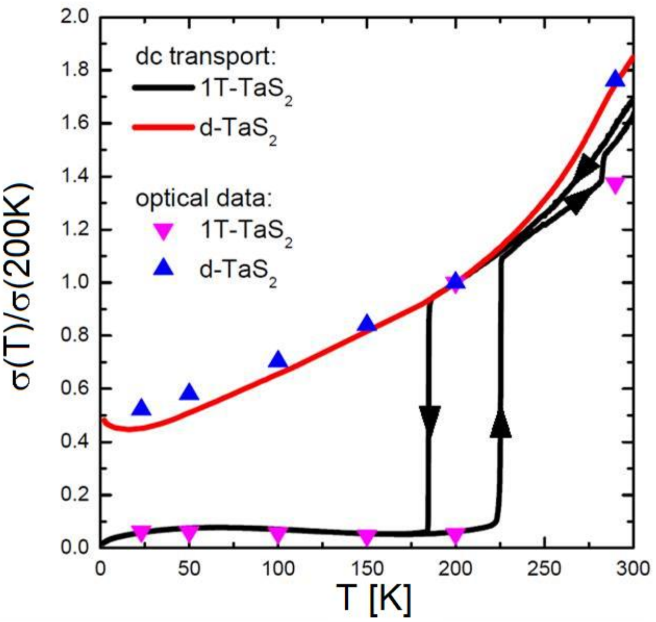

Figure 3.10. Comparison of dc conductivities gained from transport and optical measurements. Conductivity curves of pure 1T-TaS_2 in both cooling and heating are normalized to the value in cooling at 200 K. Conductivity curves of d-TaS_2 are normalized to their respective values at 200 K.

Doping can also induce superconductivity [Xu2010, Ang2012, Li2012, Ang2013, Liu2013], but the transition temperatures required were inaccessible in our optical measurements.

Chapter 4

NANO-COMPOSITE SUPERSTRUCTURING IN 1T-TaS$_2$

4.1. Nano-composite nature of the mixed phase

The NCCDW phase of 1T-TaS$_2$ has been determined to be effectively a metal-semiconductor nano-composite by X-ray and STM measurements [Spijkerman1997, Thomson1994]. The commensurate domains of the NCCDW phase are roughly hexagons 7 nm in size. The 13th electron of each David-star in a hexagon is transported from these commensurate domains to roughly triangular non-deformed (or at least much less deformed) regions between the hexagons [Sipos2008]. The commensurate hexagons are semiconducting and non-deformed triangles are metallic in nature. Together, the semiconducting and metallic areas form a rough kagome lattice, giving us an estimate of the volume fraction of ¼ and ¾ for metallic and semiconducting areas, respectively. The optical response of a composite with nano-sized grains will differ from the optical response of a homogeneous sample. The simplest way to model the optical response of a nano-composite is through an effective medium theory (EMT).

Out of several effective medium theories available, we used Bruggeman effective medium theory [Bruggeman1935, Landauer1952, Carr1985] for its symmetrical features. In fact, Bruggeman EMT has been said to be the simplest approximation giving rise to a percolation transition in a metal-insulator nano-composite [Stroud1979]. For an introduction to this theory, see Appendix B. The optical properties of the NCCDW phase of 1T-TaS$_2$ are deeply influenced by the proximity of the nano-composite to the percolation edge, as inferred from [Spijkerman1997]. This allows us to develop a simple model of the optical response of the metal-semiconductor nano-composite material.

4.2. Effect of the Fermi surface geometry on the mean free path in 1T-TaS$_2$

Further motivation for the use of EMT is the mean free path of electrons within the metallic areas. In the simple case of an isotropic electronic dispersion, dc conductivity is really the Fermi surface integral and the well-known expression for conductivity (A.7) can be expressed in terms of the Fermi surface parameters, Fermi wave vector k_F and Fermi velocity $v_F = \hbar k_F/m$,

$$\sigma_{dc} = \frac{ne^2}{\hbar k_F}\ell$$

where $\ell = v_F\tau$ denotes the mean free path of electrons between scatterings, and τ gives the scatterings time.

Let us concentrate on the quasi-two dimensional system, with conducting planes separated by distance $d_\perp$. The electronic density n and the Fermi wave vector k_F are related through $n = k_F^2/2\pi d_\perp$. Mean free path can now be written as

$$\ell = 2\pi d_\perp \frac{\hbar\sigma_{dc}}{e^2 k_F} = \frac{\hbar\sigma_{dc}}{e^2}\sqrt{\frac{2\pi d_\perp}{n}}$$

The case of the parent metallic phase of 1T-TaS$_2$ is slightly more complicated [Tutiš2014]. First, the Fermi see is composed of three parts instead of one (Fig. 4.1). Second, the anisotropy of the electronic dispersion is pronounced in each of them.

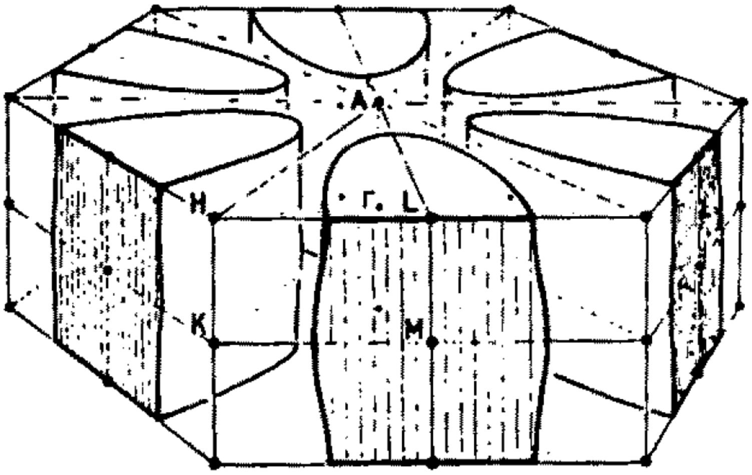

Figure 4.1. Fermi surface for undistorted 1T-TaS$_2$ [Friend1987].

The effect of the three-fold division of the Fermi surface on the formula for the mean free path may be easily derived within the model with three isotropic Fermi surfaces. Each of them contributes one third of the total conductivity, and captures one third of the occupied electronic states. This taken into account produces the relation with additional factor of $1/\sqrt{3}$ with respect to the one for the single Fermi surface.

To estimate the effect of anisotropy we approximate the Fermi surface by three elliptical shapes, oriented at 120 degrees one with respect to another. For one of those shapes, with effective masses m_a and m_b , and anisotropy $\nu = k_{Fa}/k_{Fb} = \sqrt{m_a/m_b} \leq 1$, the conductivities along the principal axes are

$$\sigma_{1aa} = \frac{n_1 e^2}{m_a}\tau, \qquad \sigma_{1bb} = \frac{n_1 e^2}{m_b}\tau$$

where particle density $n_1 = n/3$ is related to the geometry of the Fermi surface through

$$n_1 = \frac{1}{2\pi d_\perp} k_{Fa} k_{Fb} = \frac{1}{2\pi d_\perp \nu} k_{Fa}^2$$

Conductivity in an arbitrary direction at an angle ϕ relative to light-mass axis is given by

$$\sigma_1(\phi) = \sqrt{\sigma_{1aa}^2 cos^2\phi + \sigma_{1bb}^2 sin^2\phi}$$

while the contribution from three Fermi surfaces tilted by the angle $2\pi/3$ one with respect to another is given by

$$\sigma(\phi) = \sum_{j=0,1,2} \sigma_1\left(\phi + \frac{2\pi j}{3}\right)$$

While for $m_a = m_b$ the total conductivity simply triples the conductivity of a single Fermi surface, for any significant anisotropy (e.g. $\nu < 0.7$) one finds that $\sigma \approx A\sigma_{1aa}$ for arbitrary angle ϕ, with $A \approx 2$. The mean free path that dominates the conductivity is thus the one along the direction of lighter mass, $\ell = v_{Fa}\tau$, and the equation for the conductivity becomes

$$\sigma = A\frac{n_1 e^2 \tau}{m_a} = A\frac{n_1 e^2 v_{F1a}\tau}{\hbar k_{F1a}} = A\frac{n_1 e^2}{\hbar\sqrt{2\pi d_\perp n_1 \nu}}\ell$$

This leads to the final relation for the mean free path

$$\ell = g\frac{\hbar\sigma}{e^2}\sqrt{\frac{2\pi d_\perp}{n}} \tag{4.1}$$

where the factor $g \equiv \sqrt{3\nu/A^2}$ accounts for all the effects of the Fermi surface geometry, including its separation into three parts and the anisotropy of each of them. For the anisotropy appropriate in 1T-TaS$_2$, with $\nu = k_{Fa}/k_{Fb} \approx 0.5$, this factor is $g \approx 0.6$.

If the charge density n is known, we can use (4.1), otherwise we can notice that since all effects of the Fermi surface geometry are accounted for by the factor g, charge density n can be simply approximated by one of a simple metal with a circular (in two dimensions) Fermi surface with a half-filled band. In this case we use the expression for the Fermi wave vector at half-filling

$$k_F = \sqrt{\frac{4\pi}{\sqrt{3}a^2}}$$

where a is the in-plane lattice constant of undeformed 1T-TaS$_2$ and then $n = k_F^2/2\pi d_\perp$.

Mean free path of electrons in the metallic triangles of the NCCDW phase of 1T-TaS$_2$, shown in Figure 4.2, is smaller than the estimated size of metallic grains at all temperatures relevant to the experiment. Mean free path in the NCCDW phase of the d-TaS$_2$ is expected to be the same or even slightly smaller, due to the small amount of disorder.

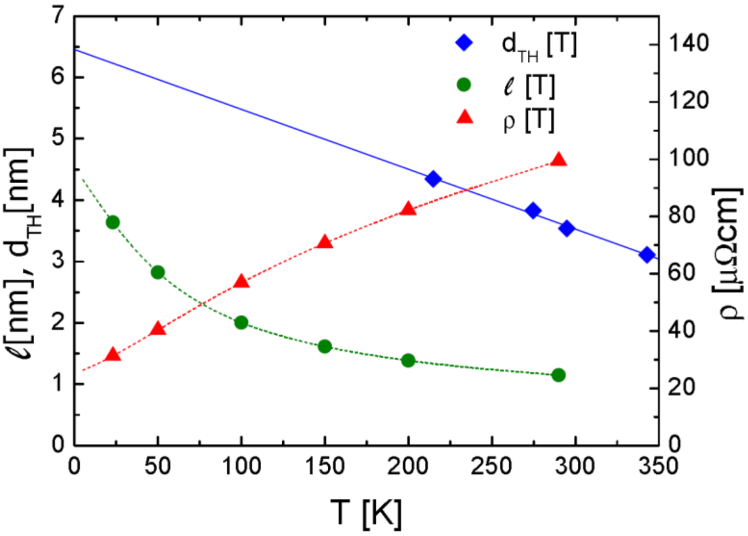

Figure 4.2. Comparison of the mean free path ℓ within the metallic triangles (green circles) to the size d_{TH} of the metallic triangles (blue rhombs) estimated from [Thomson1994] in the range 200 K to 350 K. Below that range, a linear extrapolation of the [Thomson1994] data is used to approximate the temperature dependence of the metallic triangles size. Mean free path was calculated based on the resistivity curve of the metallic phase at 8 GPa of [Sipos2008] (red triangles).

4.3. EMT model of the NCCDW phase

4.3.1. The 2-component EMT model

As previously stated, we roughly perceive the NCCDW phase of the 1T-TaS_2 as a kagome-like patchwork of metallic triangles and semiconducting hexagons (Fig. 3.1 d). From dc measurements we know that the metal grains are percolating, although, based on Spijkerman x-ray measurements, system is always close to the percolation edge. Semiconducting grains “pinch” the conductive connections between the metallic grains ever more as the temperature is lowered, increasing the scattering rate and producing the semiconductor-like appearance of the temperature dependent dc resistivity curve (Fig. 3.1).

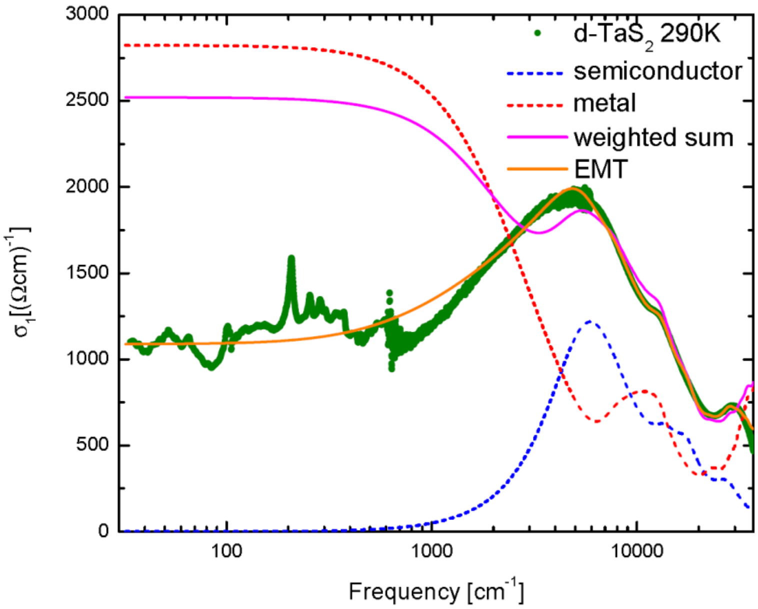

Figure 4.3. Bruggeman EMT fit to the d-TaS_2 experimental data at 290 K. Dashed red and blue lines represent the used metal and semiconductor components, respectively. Each curve shown is multiplied by the appropriate volume fraction used in the fitting. Solid magenta curve represents the normal homogeneous optical response of a metal-semiconductor alloy. It is calculated by multiplying the component models with their volume fractions and then adding them. Solid orange curve represents the EMT fit to the experimental data.

In the two-component Brugggeman EMT model, we use an estimate of the semiconducting grain size provided by ref. [Thomson1994] to calculate the depolarization factor of an equivalent ellipsoid with the same volume and semi-axis ratio. The depolarization factor of the metal grains, much as the volume fraction of the metal, is left as a free variable of the fit. The dielectric function of the metal component is obtained using the plasma frequency from the DFT calculations done in collaboration with Prof. Dr. Ivo Batistić and scattering rate of the metallic phase from the measurements of the metallic phase induced by pressure [Sipos2008] (Fig. 4.4).

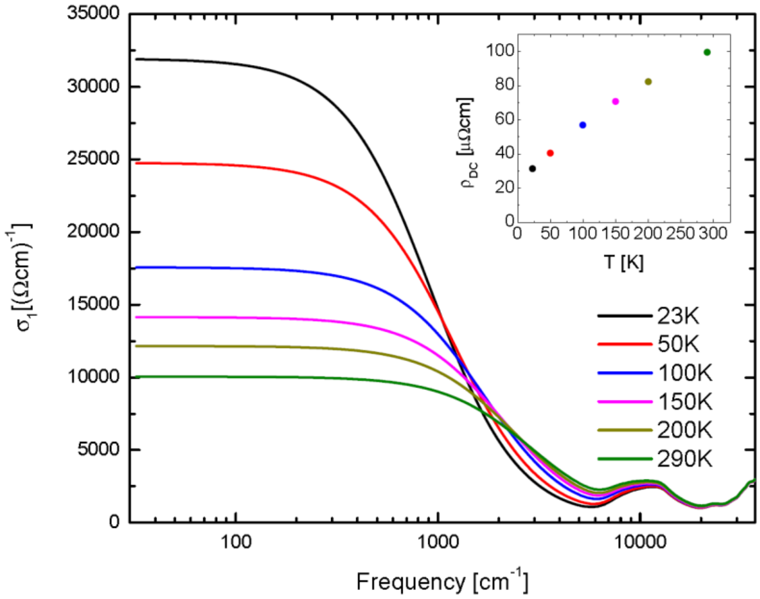

Figure 4.4. Metal component for the Bruggeman EMT model. Inset shows the dc resistivity of the metallic phase from [Sipos2008], from which scattering rates have been extracted using the DFT calculated plasma frequency.

The semiconductor component is modeled as a series of Lorentzian peaks in the interband range which are adjusted so as to get the best fit to the experimental data of the doped 1T-TaS_2 (we will refer to it as d-TaS_2). The d-TaS_2 is slightly doped with copper (less than 0.1%) which completely collapses the CCDW/Mott transition and leaves the material in the composite-like NCCDW phase down to low temperature.

As can be seen from Figure 4.3, EMT fit correctly reproduces two key features of the experimental optical conductivity: the general slope of the curve at lower frequencies and the additional spectral weight coming from the localized surface plasmon on the metallic grains at the beginning of the interband peaks. Both of these features are missing from the homogeneous fit calculated as the weighed sum of components. This strengthens our view that the NCCDW phase of 1T-TaS$_2$ must be regarded as a composite. In Figure 4.5, the temperature dependent fits are shown.

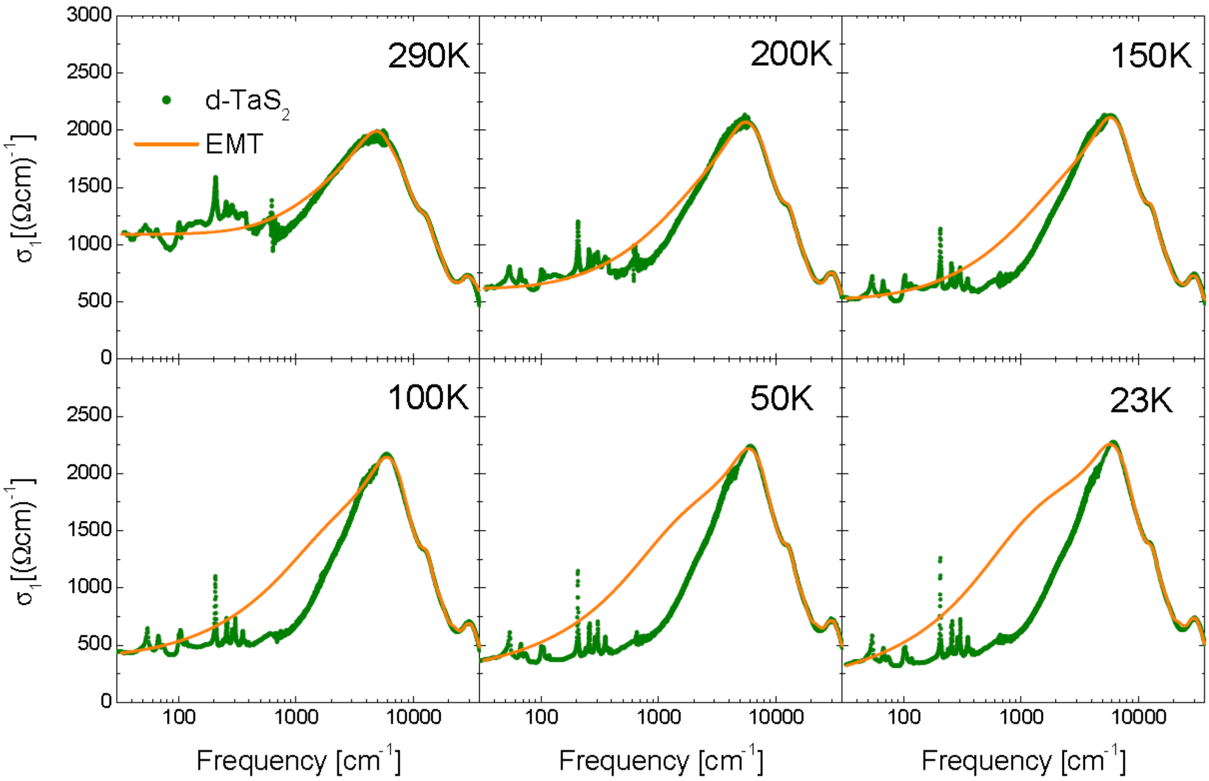

Figure 4.5. EMT fit (solid orange line) to the d-TaS$_2$ experimental data (green circles). Values of the volume fraction and the depolarization factor of the metal grains are such that metal is percolating.

Figure 4.5 shows that our basic model gives a more or less satisfactory fit at higher temperatures, but as we lower the temperature below 200 K, the surface plasmon feature becomes too large to adequately represent the behavior of the experimental curve. The problem boils down to this: to reproduce the percolation of the metallic grains seen in the experiments, we have to increase the metal volume ratio, which in turn overgrows the surface plasmon. If we decrease the metal volume fraction to enable a good fit at interband frequencies, we lose percolation and low-frequency conductivity falls to zero.

Curiously, EMT fit can be greatly enhanced if we allow an arbitrary Drude-like contribution to be added to the semiconductor grains (Fig. 4.6, Fig. 4.7). This of course turns the semiconductor into a sort of bad metal, but we will continue to call it the semiconductor component for the sake of continuity.

While these models give great fits to the experimental data, they clash with our understanding of the nature of the grains in the NCCDW phase. One might try to explain this by invoking incomplete charge transfer of the 13th electron from the semiconducting to metallic domains, but we believe there is a simpler solution. As we have already stated, STM, x-ray and dc measurements tell us that metallic domains are interconnected, but the connections are pinched by the semiconductor domains. Moreover, the scattering in these connections is much larger than in the center of the metallic grains. Therefore, all these fits are telling us is that we should add a third component, which will model the connectors between the metallic grains. Connectors should be metallic in character, but with a much larger scattering rate.

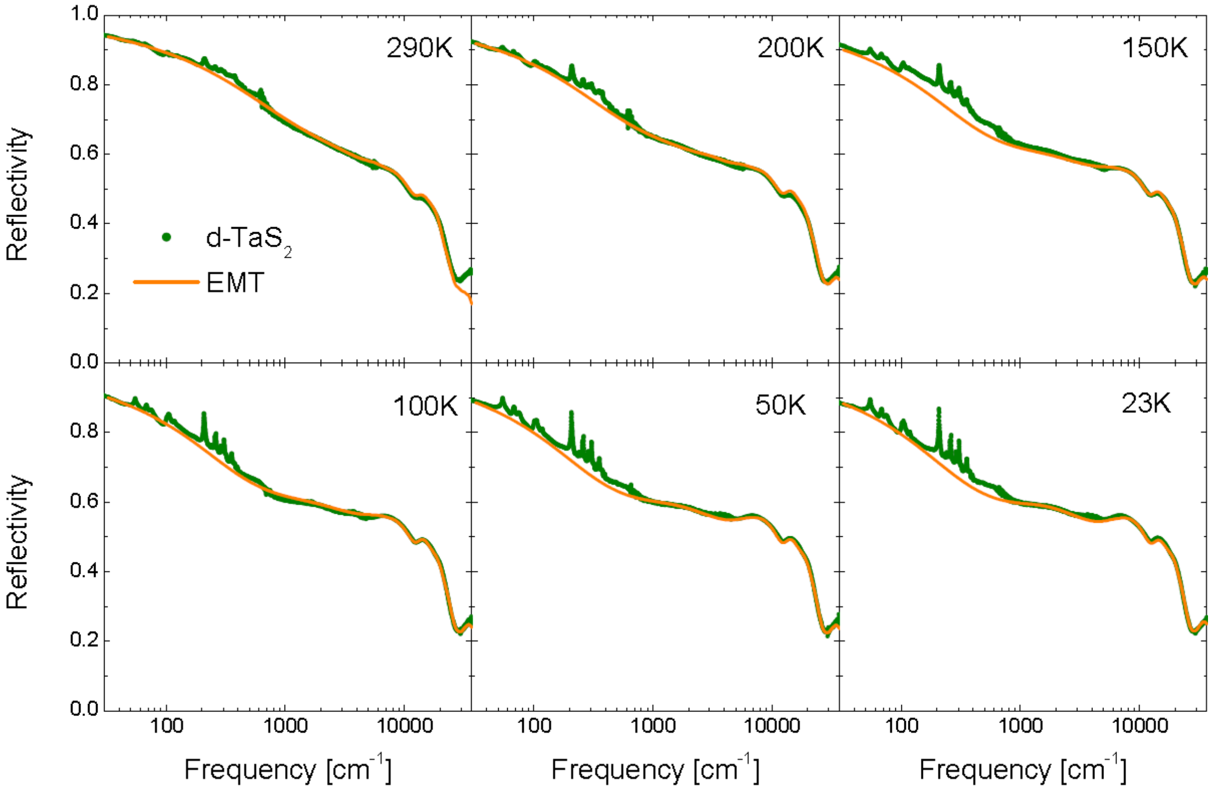

Figure 4.6. EMT fit (solid orange line) to the d-TaS$_2$ experimental reflectivity data (green circles). An arbitrary Drude-like contribution has been added to the “semiconductor” model.

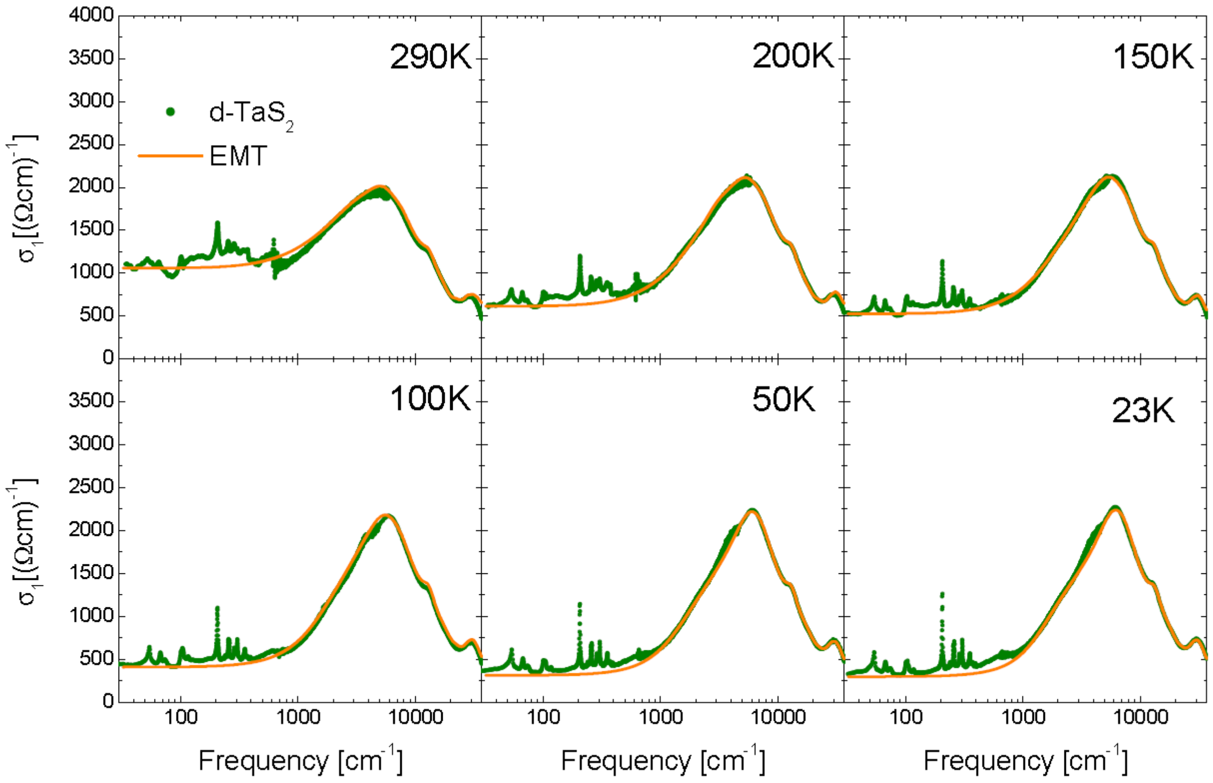

Figure 4.7. EMT fit (solid orange line) to the d-TaS$_2$ optical conductivity data (green circles). An arbitrary Drude-like contribution has been added to the “semiconductor” model.

4.3.2. The 3-component EMT model

The metal component of the 3-component EMT is based on DFT calculations and resistivity measurements under pressure (Fig. 4.4), just as in the 2-component model. The additional component in the model are the connections between the metal grains which are introduced to the model as a simple Drude term with the DFT calculated plasma frequency of 42079 cm^{-1}. Damping of 12000 cm^{-1} was chosen for the connections at all temperatures (Fig. 4.8). The semiconductor component is fitted to the experimental data. In Figure 4.9, the semiconductor component is compared to the data for 1T-TaS_2 at 23 K (CCDW/Mott insulator phase). The comparison seems to indicate no change in the CDW gap between the CCDW and NCCDW phases, and additional spectral weight present in the CCDW phase.

The 3-component EMT model gives excellent fits to the experimental data (Fig. 4.10, Fig. 4.11). Unlike the 2-component EMT models it is compliant with the physical picture gained from the various experiments from literature. Based on these findings, we feel confident that the NC phase of 1T-TaS_2 should be regarded as a composite phase and all analysis of its optical properties must be done with this in mind. The composite model gives a plausible explanation for the lack of the low-frequency spectral weight expected from the DFT calculations of the optical spectra of the undeformed triangles. Composite optical response also provides the additional spectral weight just below the interband transitions, which is missing in the homogeneous model. This additional spectral weight is standardly explained within the theory [Carr1985] as a localized surface plasmon (see Chapter 1.2.4) on the surface of the metallic grains.

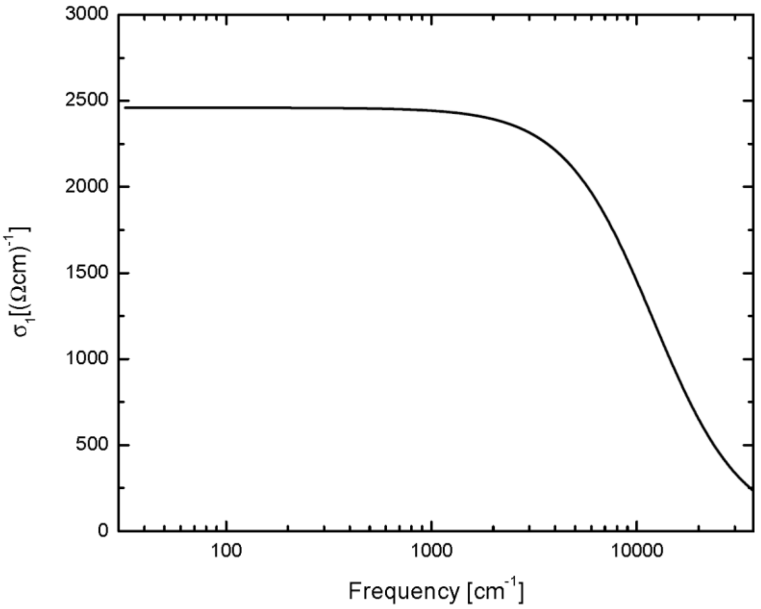

Figure 4.8. Metal connector component for the 3-component Bruggeman EMT fit.

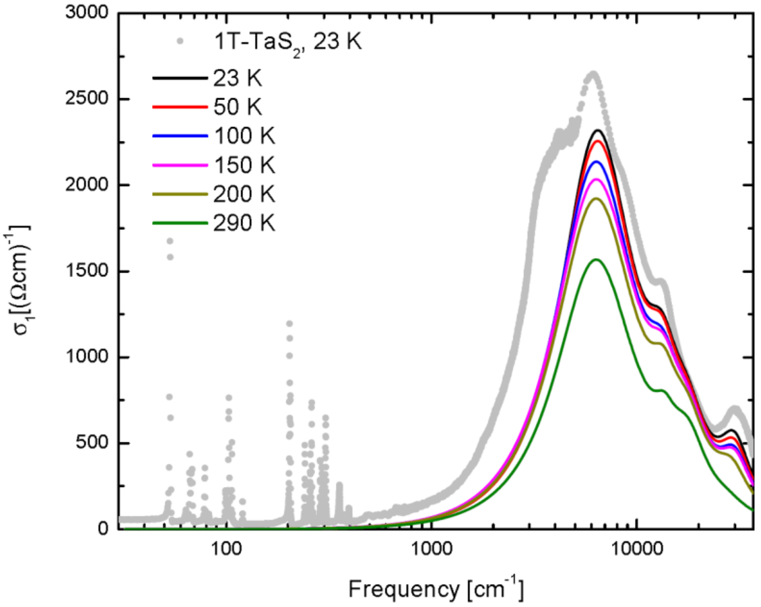

Figure 4.9. Semiconductor component for the 3-component Bruggeman EMT fit. Model (solid lines) is compared to the optical conductivity of the 1T-TaS$_2$ at 23 K (gray circles, CCDW/Mott insulator phase).

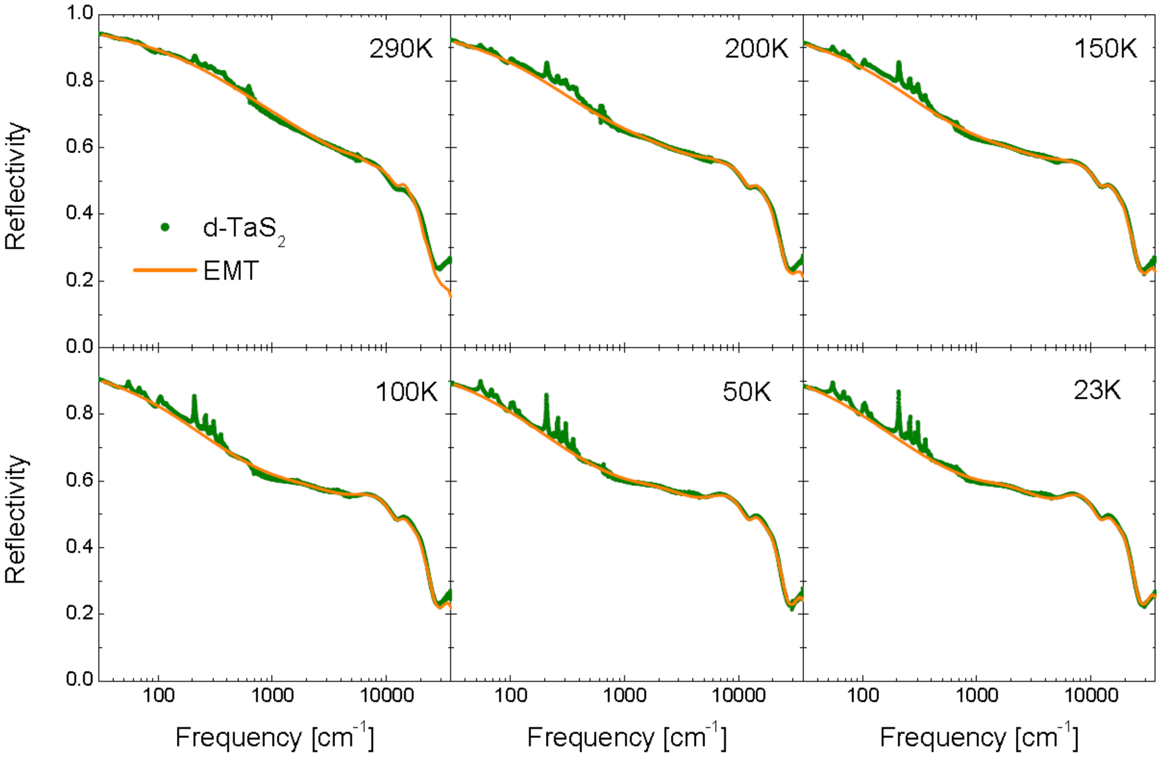

Figure 4.10. Three-component Bruggeman EMT fit (solid orange line) to the d-TaS_2 experimental reflectivity data (green circles).

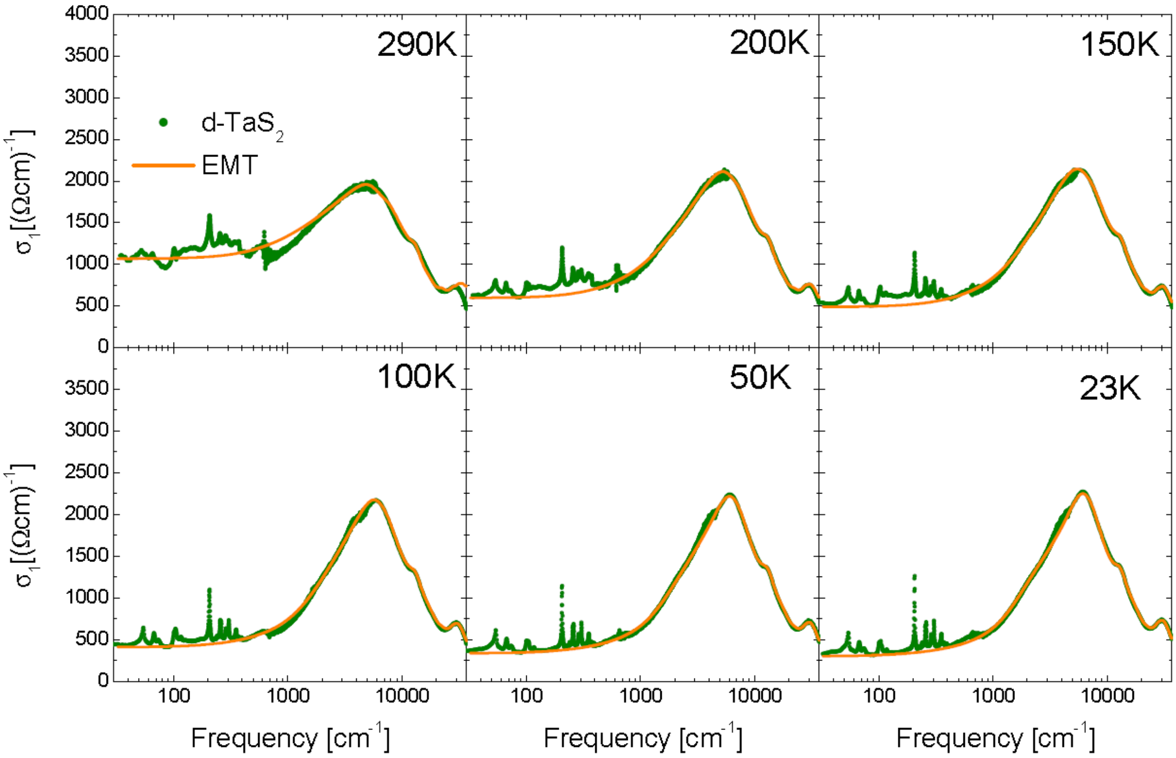

Figure 4.11. Three-component Bruggeman EMT fit (solid orange line) to the d-TaS_2 optical conductivity data (green circles).

4.4. Conclusions of Chapter 4

While the nano-texturing of the NCCDW phase of 1T-TaS$_2$ has been proven to exist for a relatively long time [Spijkerman1997], the extreme relevance it has for the transport properties has been recognized relatively recently [Sipos2008]. However, the impact this nano-texturing has on the optical properties of the material has not been realized until now. Previous models of optical properties of the NCCDW phase of 1T-TaS$_2$ were based on the premise that we are dealing with a single crystal so the homogeneous Drude-Lorentz model is best suited to describe all phases of the material. Although this might seem as a logical first step, it grossly underestimates the effect electron density nano-structuring has on the NCCDW phase. In effect, the material in the NCCDW phase has a regular, kagome-like array of semiconducting and metallic areas. This means that the NCCDW phase of 1T-TaS$_2$ is, for all intents and purposes, a textured nano-composite phase. To adequately model its optical response, more complex models are required than the standard homogeneous Drude-Lorentz model.

NCCDW phase of 1T-TaS$_2$ was studied in this work down to very low temperatures by using a 1T-TaS$_2$ sample doped with less than 0.1% copper, which completely suppressed the CCDW/Mott insulator transition. The 3-component Bruggeman effective medium theory has been shown to satisfactorily model the temperature dependent optical response of the NCCDW phase. Two standing problems of the homogeneous model of the optical properties of the NCCDW phase were addressed: missing spectral weight at low frequencies belonging to the metallic domains and excess spectral weight just below the interband transitions. Both problems were identified as consequences of the (effectively) nano-composite nature of the NCCDW phase and modeled within the EMT. Spectral weight of the metallic triangles is actually much larger, in accordance with the DFT calculations, but the EMT mixing produces the reduction at low frequencies. The excess spectral weight which could not be explained in a homogeneous model (because it was too low in frequency to be an interband transition, yet much too strong and wide for a phonon mode), was identified as the localized surface plasmon on the surface of the metallic domains.

Chapter 5

CHARGE REDISTRIBUTION OVER SUPERSTRUCTURE

The CCDW and NCCDW phases of 1T-TaS$_2$ are composed of stars, each star having 13 original undeformed TaS$_2$ formula units. The deformation that leads to the formation of stars also introduces the charge redistribution between its formula units, identified as the charge-density-wave (CDW) state. This charge redistribution is essential for the appearance of new optical modes. We will show how the charge redistribution and mere refolding of acoustical phonon branches of the parent phase results in four groups of optically active phonons in the acoustic frequency range, as observed experimentally. The high symmetry of stars implies the ABBA pattern of emerging oscillator spectral weights, whereas the ratio of two intensities reflects the charge redistribution in the star. The analysis presented in this chapter was partly developed in collaboration with Dr. Eduard Tutiš.

5.1. Optical conductivity of phonons

Real part of the optical conductivity originating from the lattice oscillations has the general form

$$\sigma_{\alpha\alpha}(\omega) = \sum_{\mu} \frac{\omega^2 \Gamma_\mu}{\left(\omega_\mu^2 - \omega^2\right)^2 + \omega^2 \Gamma_\mu^2} f_{\mu,\alpha}$$

where $\alpha = x, y, z$ are the indices of Cartesian axes, μ is the index of the phonon mode, ω_μ stands for the frequency of the mode at $k = 0$, Γ_μ is the width of the phonon signal and $f_{\mu,\alpha}$ stands for the oscillator strength of the mode. The oscillator strength $f_{\mu,\alpha}$ is given by the square of the dipolar strength of the mode,

$$f_{\mu,\alpha} \equiv \frac{1}{V_{u.c.}} \left| \sum_n q_n \frac{\lambda_{n,\alpha}^{\mu}}{\sqrt{m_n}} \right|^2,$$

where n goes over the atoms in the unit cell of the crystal, q_n and m_n stand respectively for the charge and the mass of the atom labeled by n, $V_{u.c.}$ is the volume of the unit cell, and $\lambda_{n,\alpha}^{\mu}$ are the components of the polarization vector. As usual, the expansion of the displacement $u_{n,\alpha}(R,t)$ (of atom n in the unit cell at the Bravais lattice node R) over the phonon modes is written in the form (with a_k^{μ} being the expansion coefficients and N the number of unit cells):

$$u_{n,\alpha}(R,t) = \frac{1}{\sqrt{m_n}} \frac{1}{\sqrt{N}} \sum_{\mu} \sum_{k} a_k^{\mu}\, e^{-i\omega_{\mu,k} t} \lambda_{n,\alpha}^{\mu,k} e^{ikR}$$

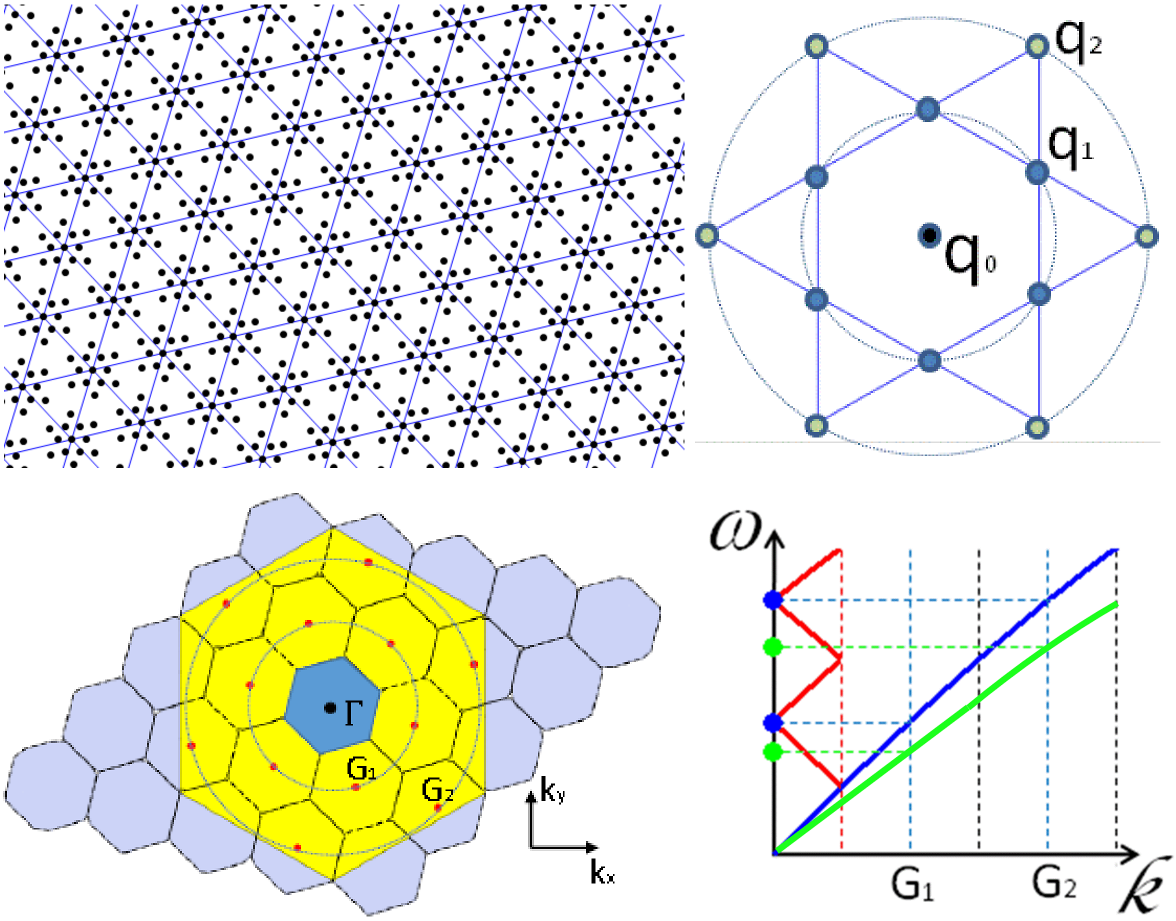

Figure 5.1. *Top left*: Representation of the CCDW superstructured lattice with the star-like clusters (deformations exaggerated for effect). *Top right*: Representation of one Star-of-David deformation in the commensurate CDW of 1T-TaS_2. For simplicity, only Ta sites are shown, but each dot actually represents one unit cell of the original undeformed lattice (one Ta, two S). q_0 is the charge change in the center (compared to the charge at the same site with no deformation), q_1 is the charge change on any site of the inner ring in the star, q_2 is the charge change on any site of the outer ring. *Bottom left*: Representation of the unit cell refolding due to the superstructuring. Red circles mark the reciprocal points of the undeformed unit cell that will be refolded onto the Γ point of the new deformed unit cell. Notice that there are two inequivalent wave vectors being refolded: one in the inner circle (labeled G_1) and one in the outer circle (labeled G_2). *Bottom right*: Simplified sketch of refolding of two acoustic phonon branches due to superstructuring.

Let us look at superstructuring such as the one in the CCDW phase of 1T-TaS$_2$. In 1T-TaS$_2$, thirteen of the original unit cells containing one Ta atom and two S atoms form a Star-of-David cluster, with stars themselves forming a regular structure (Fig. 5.1, top left). Generally speaking, deformation of the crystal lattice produces the deformed unit cell in real space, which is larger than the original undeformed unit cell (Fig. 5.1, top right). The M-fold enlarged unit is composed of M original unit cells at nodes $R = R_1, \dots, R_M$ of the Bravais lattice of the parent crystal (e.g. in Fig. 5.1, top right, each site can be labeled from R_1 to R_{13}). Atoms in the extended cell can be conveniently indexed by the composite index (n, R) that includes the position of the primitive unit cell R and the index n of the atom within that cell (for 1T-TaS$_2$, the index n would go over one Ta atom and two S atoms). In the reciprocal space, super-structuring leads to the Brillouin zone that is M-fold smaller than the original one (small blue hexagon in Fig. 5.1, bottom left).

The lattice dynamics can be followed either within this new and smaller Brillouin zone or within the original and bigger one. Of course, the total number of degrees of freedom in the crystal does not change upon restructuring, so the number of phonon branches in original zone does not change, whereas the number of phonon branches is M times bigger in the new zone (Fig. 5.1, bottom right). The simple folding of the phonon branches from the old to the new zone links the mode μ at the wave vector k in the original zone to the mode (μ, G) at wave-vector κ in the new zone, with $k = \kappa + G$. The index $G = G_1, \dots, G_M$ denotes one of the vectors of the reciprocal lattice of the reconstructed crystal that falls within the original Brillouin zone. For 1T-TaS$_2$ the index G would go from G_1 to G_{13}, although only three of those wave vectors are inequivalent – one for the center (always labeled Γ), one for the inner circle (labeled G_1) and one for the outer circle (labeled G_2, Fig. 5.1, bottom left). There are 6 equivalent wave vectors at the inner and 6 at the outer circle so we can label them as $G_{1,j}$ and $G_{2,j}$, $j = 1, \dots, 6$ for the inner and outer circle, respectively.

The contribution of phonons to the optical conductivity of the restructured crystal is written as

$$\sigma_{\alpha\alpha}(\omega) = \frac{1}{V_M} \sum_{\mu,G} \frac{\omega^2 \Gamma_{(\mu,G)}}{\left[\omega_{(\mu,G)}^2 - \omega^2\right]^2 + \omega^2 \Gamma_{(\mu,G)}^2} \left| \sum_{R,n} q_{(R,n)} \frac{\lambda_{(R,n),\alpha}^{(\mu,G)}}{\sqrt{m_n}} \right|^2$$

where V_M is the volume of the reconstructed unit cell, $V_M = V_{u.c.}/M$. As will be shown below, changes in $q_{(R,n)}$ introduced by restructuring lead to the new optically active modes in the acoustic frequency range of the parent structure, whereas the changes in polarization vectors

$\lambda_{(R,n),\alpha}^{(\mu,G)}$ introduced by the (partial) condensation of the super-structuring phonon-mode are non-essential in that respect. Thus, the polarization vectors $\lambda_{(R,n),\alpha}^{(\mu,G)}$ derived by formally refolding the phonon spectrum before the condensation may be used to calculate the optical strengths of new phonon modes.

5.3. Acoustic and dipolar modes

Acoustic modes produce no electric dipole in the crystal, irrespective of their wave vector. This is just another way of stating that these modes are not optically active. The static deformation that produces stars in 1T-TaS$_2$ emerges from the softening and the subsequent freezing of the acoustic modes (at $k = G_{1,j}, G_{2,j},\ j = 1, \dots ,6$) of the parent structure. We may further assume that the oscillations of the supercell within the frequency range of the acoustic branches of the parent structure can be decomposed into acoustic modes of the parent structure. No electric dipole can be produced by such oscillations without additional charge redistribution, whatever the changes in the dynamical matrix of the system may be. On the other hand, charge redistribution produces optically active modes even in the absence of any further changes in the dynamical matrix. Thus, charge redistribution between the primitive unit cells in the (commensurate) CDW system is the essential requirement for finite optical response of emerging $\kappa = 0$ modes in the acoustical frequency range. Top panel of Figure 5.2 shows the result of simple mass-spring model calculation for 1T-TaS$_2$. In the model, the lattice is undeformed, while the charge distribution is changed. It is evident that this simple model of 1T-TaS$_2$ shows four Ta-related modes (labeled Ta$_1$, Ta$_2$, T$_3$ and Ta$_4$ from the lowest to the highest in frequency, respectively). The last mode visible in the figure is the S$_0$ mode. This is the sulphur-related mode which is always present. In fact, in the undeformed 1T-TaS$_2$ in the metallic state, S$_0$ is the only mode present. Lower panel of Figure 5.2 shows the experimental real part of optical conductivity for 1T-TaS$_2$ at 23 K. This is a clear example of what happens when lattice deformation is added to the charge redistribution (as is the case in the real material). Basic phonon modes have been split-off into additional peaks as a consequence. It is important to notice here that since the changes in the dynamical matrix do not introduce new optically active modes (i.e. no new spectral weight is added), splitting of a peak merely distributes the spectral weight of the original mode among its split-off descendants. In other words, by merely summing over the spectral weight of the split-off modes attributed to one of the original modes, we can determine the exact spectral weight of the said original mode. Red circles and labels in the bottom panel of Figure 5.2 show our determination of the affiliation each experimental peak has to the original peaks brought on by charge redistribution.

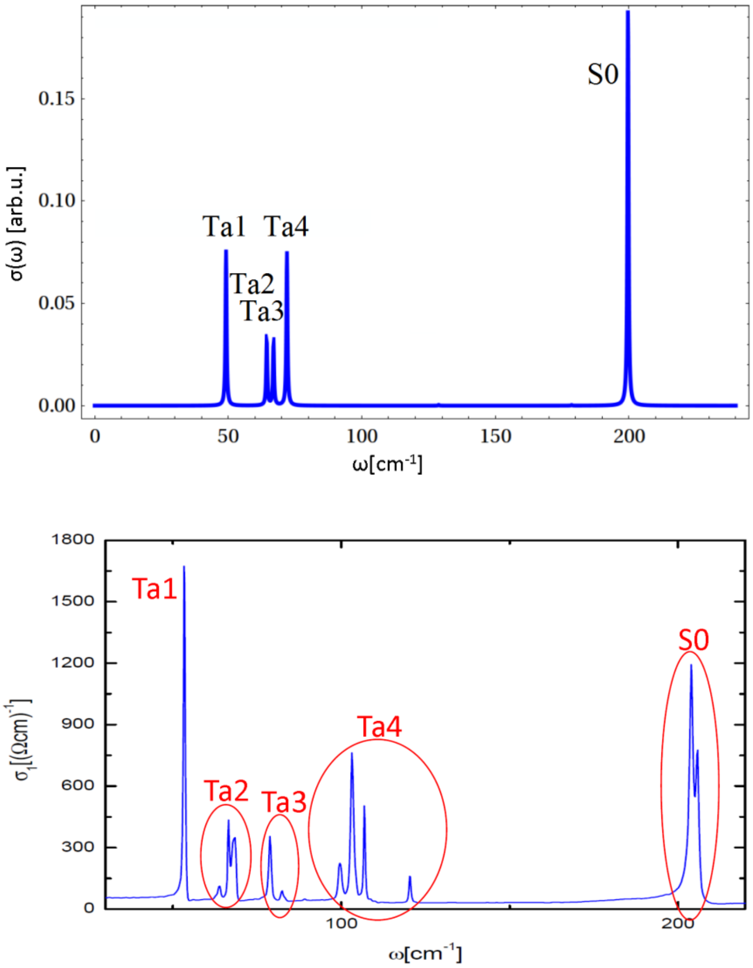

Figure 5.2. *Top*: Result of a simple mass-spring model of 1T-TaS$_2$. There is no deformation of the lattice, only charge redistribution. Resulting modes have been labeled from lowest to highest in frequency Ta$_1$, Ta$_2$, Ta$_3$, Ta$_4$ and S$_0$. *Bottom*: Real part of the experimental optical conductivity of 1T-TaS$_2$ at 23 K. Phonon groups split-off from the original mode are indicated (see text for details).

The displacement of the atom n in the primitive cell labeled R ($R = R_1, \ldots, R_M$) in a simply refolded system may be written as

$$u_{(R,n),\alpha}(t) = \frac{1}{\sqrt{m_n}}\frac{1}{\sqrt{N'M}}\sum_{\mu}\sum_{G}\sum_{\kappa} a^{\mu}_{\kappa+G}\,(t)\lambda^{\mu,\kappa+G}_{n,\alpha}e^{i(\kappa+G)R}$$

$$\equiv \frac{1}{\sqrt{m_n}}\frac{1}{\sqrt{N'}}\sum_{(\mu,G)}\sum_{\kappa} a^{(\mu,G)}_{\kappa}\,(t)\lambda^{(\mu,G),\kappa}_{(R,n),\alpha}$$

where κ goes over the Brillouin zone of the reconstructed crystal (*M* times smaller than the original Brillouin zone) and $G = G_1, \dots, G_M$ goes over the vectors of the reciprocal lattice of the reconstructed crystal that fall within the original Brillouin zone. The number of phonon modes in the reduced Brillouin zone is *M* times increased. The modes, now labeled by (μ, *G*), have frequencies

$$\omega^2_{(\mu,G),\kappa} = \omega^2_{\mu.\kappa+G}$$

and polarization vectors

$$\lambda^{(\mu,G),\kappa}_{(j,R),\alpha} = \frac{1}{\sqrt{M}}\lambda^{\mu,\kappa+G}_{j,\alpha}e^{i(\kappa+G)R}$$

5.4. Optical response of a restructured system

The response comprises the contribution of $\kappa = 0$ modes,

$$\sigma_{\alpha\alpha}(\omega) = \frac{1}{V_M}\sum_{\mu,G}\frac{\omega^2\Gamma_{(\mu,G)}}{\left[\omega^2_{(\mu,G)} - \omega^2\right]^2 + \omega^2\Gamma^2_{(\mu,G)}}\left|\sum_{R,n} q_{(R,n)}\frac{\lambda^{(\mu,G)}_{(R,n),\alpha}}{\sqrt{m_n}}\right|^2$$

where the *M* phonon branches, $G = G_1,\dots,G_M$, appear for each original branch μ. For the branches derived from the acoustic branch μ, the $G = 0$ branch is of no interest ($\omega_{(\mu,G)} = 0$), whereas the 12 remaining branches may be grouped in two “rings” $r = 1, 2$ (Fig. 5.1, bottom left), corresponding to two groups of reciprocal lattice wave-vectors of equal distance from the origin, and related by the π/3 rotation $\Re$

$$G_{r,j} \equiv \Re^{j-1}G_r,\quad r = 1,2;\ j = 1,\dots,6$$

and of the same frequency

$$\omega_{\mu,G_{r,j}} = \omega_{\mu,G_r}$$

We assume that the charge redistribution dominantly occurs on tantalum (Ta) atoms, thus

$$\sigma_{\alpha\alpha} = \frac{1}{m_{Ta}}\frac{1}{V_M}\sum_{\mu,g} \frac{\omega^2\Gamma_{\mu,r}}{\left[\omega_{\mu,G_r}^2 - \omega^2\right]^2 + \omega^2\Gamma_{\mu,r}^2} f_{\mu,r,\alpha}$$

where the common oscillator strength for the “ring” is given by the sum

$$f_{\mu,r,\alpha} \equiv \sum_{j=1}^{6}\left|\sum_R q_{Ta,R}\,\lambda_{Ta,R,\alpha}^{(\mu,G_{r,j})}\right|^2.$$

This sum may be evaluated to

$$f_{\mu,r,\alpha} \equiv \sum_{j=1}^{6}\left|\lambda_{Ta,\alpha}^{\mu}(G_{r,j})\right|^2\left|\frac{1}{\sqrt{M}}\sum_R q_{Ta,Z}\,e^{iG_{r,j}R}\right|^2$$

$$= \sqrt{M}|q(G_r)|^2\sum_{j=1}^{6}|\lambda_{Ta,\alpha}^{\mu}(G_{r,j})|^2 = 3\sqrt{M}\lambda_{Ta}^2|q(G_r)|^2$$

where the “Star-Fourier transform” of the charge distribution was defined as

$$q(G) \equiv \frac{1}{M}\sum_R q_{Ta,R}\,e^{iGR}$$

The relation

$$\sum_{j=1}^{6}\left|\lambda_{Ta,\alpha}^{\mu}(G_{r,j})\right|^2 = 3\lambda_{Ta}^2$$

was also used, based on the symmetry of the acoustic polarization vector of Ta-displacements.

$$\lambda_{Ta}^{\mu}\left(G_{r,j}\right) = \Re^{j-1}\boldsymbol{\lambda}_{Ta}^{\mu}(G_r),$$

$$\sum_{j=1}^{6}\left|\lambda_{Ta,\alpha}^{\mu}(G_{gj})\right|^2 = \lambda_{Ta}^2 \approx \frac{m_{Ta}}{m_{Ta}+2m_s}$$

The last estimate of the polarization vector λ_{Ta} may be made based of the requirement for the acoustic modes $u_{Ta} \approx u_{S1} \approx u_{S2}$, leading to $\lambda_{Ta}^2 \approx \frac{m_{Ta}}{m_{Ta}+2m_s}$. Thus the optical intensities of the modes are essentially determined only by the Star-Fourier transforms of the charge distribution

$$f_{\mu,r} \propto |q(G_r)|^2$$

The charges of Ta-atoms within the Star-of-David will be conveniently denoted by $q_0 = -12q$, $q_1 = q - \sqrt{M}\delta$, and $q_2 = q + \sqrt{M}\delta$ respectively for the Ta-atom in the center of the star, the Ta-atom in the inner ring and the Ta-atom in the outer rings of the star. The neutrality demands to have $q_0 + 6q_1 + 6q_2 = 0$. Within this notation the Star-Fourier transforms of the charge distribution, and the optical phonon intensities are simply expressed as

$$f_{1,2} \propto \left|q(G_{1,2})\right|^2 = |q \pm \delta|^2$$

5.5. Analysis of the NCCDW phonon data

Using this analysis, we can calculate the relative charge redistribution over the superstructure of the commensurate CDW lattice of 1T-TaS_2. To do so, we need to know the relative spectral weights of the four original Ta modes created by the charge distribution (if structural deformation is not taken into account). In a real crystal, we also have structural deformation, but this only induces splitting of the phonon peaks, seen in the experimental data. Spectral weight of each original phonon mode is preserved and distributed among its split-off "descendants". We label the original phonon modes as Ta_1, Ta_2, Ta_3 and Ta_4 and refer to their split-off modes collectively as Ta_1, Ta_2, Ta_3 and Ta_4 phonon groups. Spectral weight of each original phonon mode can be calculated by summing the spectral weights of phonons in its phonon group. Two phonon groups related to wave vector G_1 should have the same spectral weight (we will call it B), while phonon groups related to wave vector G_2 should have the same spectral weight (we will call it A).

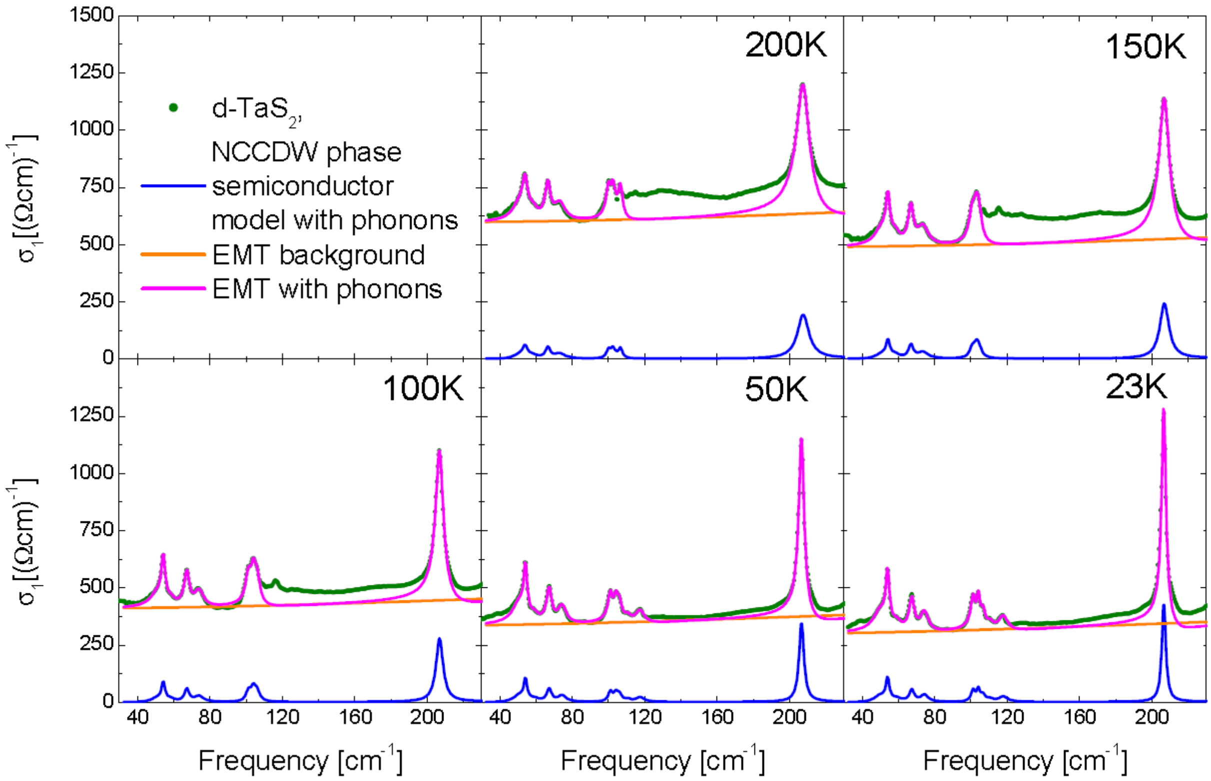

Figure 5.3. Three-component Bruggeman EMT fit (solid magenta line) to the d-TaS$_2$ optical conductivity data (green circles) in the NCCDW phase. Phonon modes have been added to the semiconducting model. The phonon mode just above 200 cm^{-1} has also been added to the metal and connector model. The logic behind mode assignation is the same as in Figure 5.2.

Figure 5.3 shows the comparison of the 3-component EMT fits with and without phonons to the experimental data. Phonon modes have been divided into four groups Ta$_1$, Ta$_2$, Ta$_3$ and Ta$_4$, based on the insight gained from DFT calculations. Spectral weight of phonons within each group has been summed and normalized to the spectral weight of the Ta$_1$ phonon group. The result is shown in Table 5.1. The data definitely displays an A:B:B:A pattern of relative spectral weights of phonon groups. More than that, relative spectral weights seem to roughly have a 1:1/3:1/3:1 relation at 23 K which changes in temperature to 1:1/2:1/2:1 at 200 K.

Table 5.1. Relative spectral weights (with errors) of the four tantalum phonon groups in NC phase of d-TaS$_2$, normalized to the first tantalum phonon group. Spectral weights were obtained by fitting the phonon modes within the 3-component Bruggeman EMT.

T[K]	$\frac{SW(Ta1)}{SW(Ta1)}$	$\frac{SW(Ta2)}{SW(Ta1)}$	$\frac{SW(Ta3)}{SW(Ta1)}$	$\frac{SW(Ta4)}{SW(Ta1)}$
23	1	0.36 ± 0.05	0.34 ± 0.05	0.9 ± 0.2
50	1	0.35 ± 0.05	0.31 ± 0.05	1.1 ± 0.2
100	1	0.49 ± 0.05	0.47 ± 0.05	1.3 ± 0.6
150	1	0.50 ± 0.05	0.54 ± 0.05	1.5 ± 0.6
200	1	0.44 ± 0.05	0.45 ± 0.05	1.4 ± 0.6

We can now calculate the redistribution of charge over the superstructure in the semiconducting domains of the NCCDW phase (Table 5.2). The data in Table 5.2 displays the relative charge redistribution on the central site, inner ring and outer ring of the David-star deformation, normalized to the change on the central site. We can see that, within the error of the calculation, all charge redistribution is between the outer ring and the center, at all temperatures. It is possible that up to 10% of the charge transferred to the center comes from the inner ring as the temperature is increased, but this seems to be negligible compared to the exchange between the inner ring and the center.

Table 5.2. Redistribution of charges in the NC phase of d-TaS$_2$, normalized to the central site of the deformation. Error is ±0.1.

T[K]	$\Delta Q_0/\Delta Q_0$	$6\Delta Q_1/\Delta Q_0$	$6\Delta Q_2/\Delta Q_0$
23	1	-0.0	-1.0
50	1	-0.0	-1.0
100	1	-0.1	-0.9
150	1	-0.1	-0.9
200	1	-0.1	-0.9

5.6. Analysis of the CCDW phonon data

Due to the high asymmetry of several phonon modes in the CCDW phase of 1T-TaS$_2$, we used the Fano formula (1.1) [Fano1961, Dean2011, Thomsen1991] to fit the observed phonon modes.

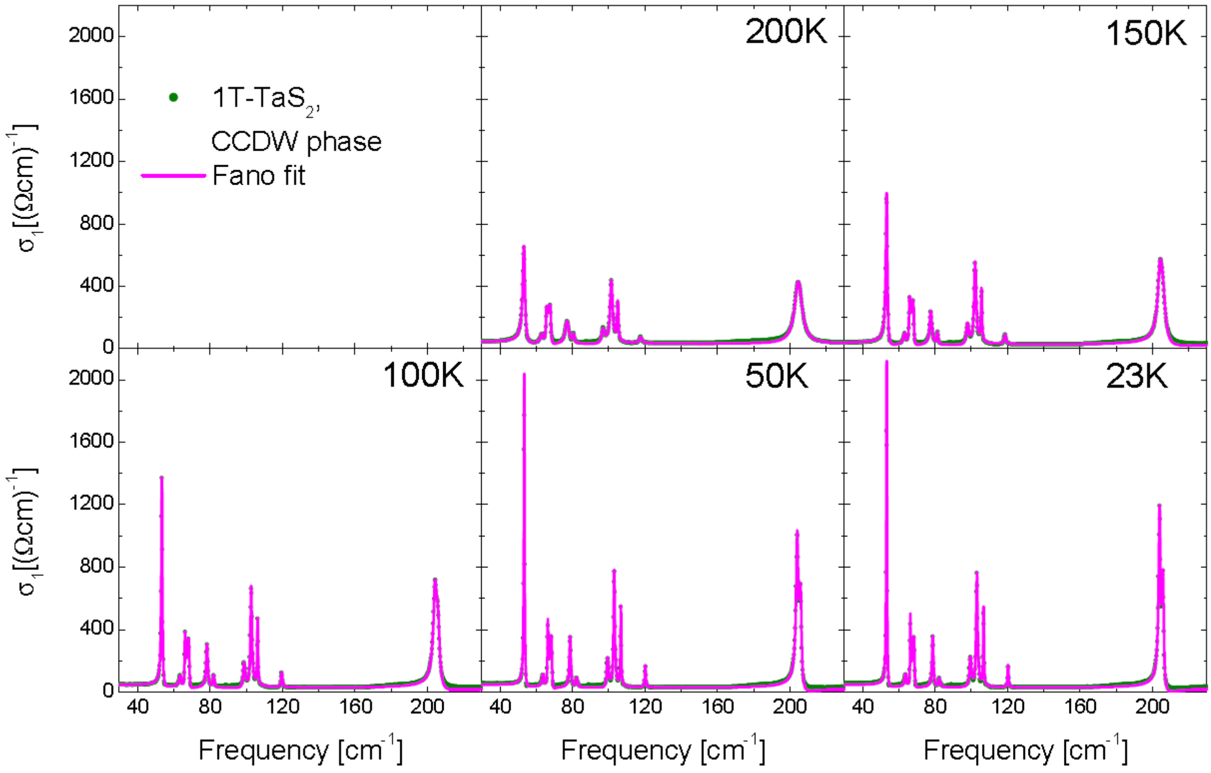

Figure 5.4. Fano fit (solid magenta line) to the 1T-TaS$_2$ optical conductivity data (green circles) in the CCDW phase.

Figure 5.4 shows the Fano fit to the experimental optical conductivity of 1T-TaS$_2$ in the CCDW phase. For all fits we had to use a small Drude-like background. Spectral weight of a Fano mode can be calculated using the expression (1.2) [Cappelluti2012, DiPietro2014]. 5.3 gives the spectral weight of the Ta phonon groups normalized to Ta1, the phonon group lowest in frequency. It shows that relative spectral weights progress from 1:2/3:1/3:1 relation at 23K to the 1:2/3:1/2:1 relation at 200K. Within our analysis, we expect the spectral weight relation to be A:B:B:A (i.e. spectral weights are expected to be the same for the pair of groups related to the same wavevector which folds into the Γ point of the deformed unit cell). Therefore, our analysis seems not to be adequate for the CCDW/Mott insulator phase.

Table 5.3. Relative spectral weights with errors of the four tantalum phonon groups in the C phase of 1T-TaS$_2$, normalized to the first tantalum phonon group. Spectral weights were obtained by fitting the phonon modes with the Fano asymmetrical phonons.

T[K]	$\frac{SW(Ta1)}{SW(Ta1)}$	$\frac{SW(Ta2)}{SW(Ta1)}$	$\frac{SW(Ta3)}{SW(Ta1)}$	$\frac{SW(Ta4)}{SW(Ta1)}$
23	1	0.60 ± 0.05	0.37 ± 0.05	1.3 ± 0.3
50	1	0.59 ± 0.05	0.38 ± 0.05	1.2 ± 0.3
100	1	0.66 ± 0.05	0.44 ± 0.05	1.3 ± 0.3
150	1	0.66 ± 0.05	0.41 ± 0.05	1.2 ± 0.3
200	1	0.60 ± 0.05	0.45 ± 0.05	1.2 ± 0.3

5.7. Conclusions of Chapter 5

Superstructuring has a profound effect on the optical properties of 1T-TaS_2. This is true for both the commensurate and nearly commensurate phase. Superstructuring causes the folding of the original undeformed first Brillouin zone into the smaller deformed zone. This is also why acoustical phonon dispersion branches refold into the smaller first Brillouin zone. In doing so, acoustical (i.e. not optically active) modes produce new optical modes at finite frequencies. Refolding alone is not enough to make the new optical mode active. As it has been demonstrated in this chapter, the bottom line is that to get active optical modes there has to be a dipole moment (i.e. charge redistribution). All the lattice deformation then does is to split the optical modes brought on by the charge redistribution, but this does not change the spectral weight of the original mode.

Novel analysis of the phonon modes presented here enables the determination of the charge redistribution over the star-like deformation in the commensurate phase of 1T-TaS_2 solely from the optical data. Considering that the NCCDW phase consists of undeformed areas and CCDW domains, analysis extends to the NCCDW phase. Based on this analysis, we find that effectively all charge transfer in the NCCDW phase of d-TaS_2 is between the outer ring and the center of the star, leaving the inner ring untouched (within the error of the procedure).

An assumption (backed by the DFT calculations) we have used in this analysis is that Ta-related orbitals dominate the Fermi level. This in turn allowed us to approximate the covalent bond within the layer with an effectively “ionic” bond. This approximation looks at the charges around the Ta atoms as an electron cloud sticking to its respective atom. This procedure yields good results in the NCCDW phase, but in the CCDW/Mott phase we run into problems. The ratio of the phonon mode spectral weights is clearly not A:B:B:A anymore. This precludes us from using the same procedure because the A:B:B:A pattern is a consequence of the effective “ionicity” of Ta atoms in the NCCDW phase. Changes in the spectral weight ratios of phonon modes in the CCDW phase of 1T-TaS_2 point to the mixing of the Ta and S orbitals at the Fermi level as the 13th electron is localized on the star-like superstructure. Therefore, we were not able to determine the charge transfer in the commensurate/Mott phase.

Chapter 6

SUPERSTRUCTURING OF 1T-TiSe$_2$

6.1. Introduction to 1T-$TiSe_2$

1T-polytype of $TiSe_2$ shows the same basic structure as previously described 1T-TaS_2 – one transition metal atom in an octahedral arrangement between six chalcogenide atoms. 1T-$TiSe_2$ is also a quasi-two-dimensional layered material where each layer consists of one Ti plane sandwiched between two Se planes. There are strong covalent bonds within layers and, as standardly described, weak van der Waals bonds between layers. In the normal phase the material has a hexagonal structure with lattice constants of a = 3.535 Å in-plane and c = 6.004 Å out of plane [DiSalvo1976B, Greenaway1965] (Fig. 6.1). Se planes are positioned at 0.25c below and above Ti plane.

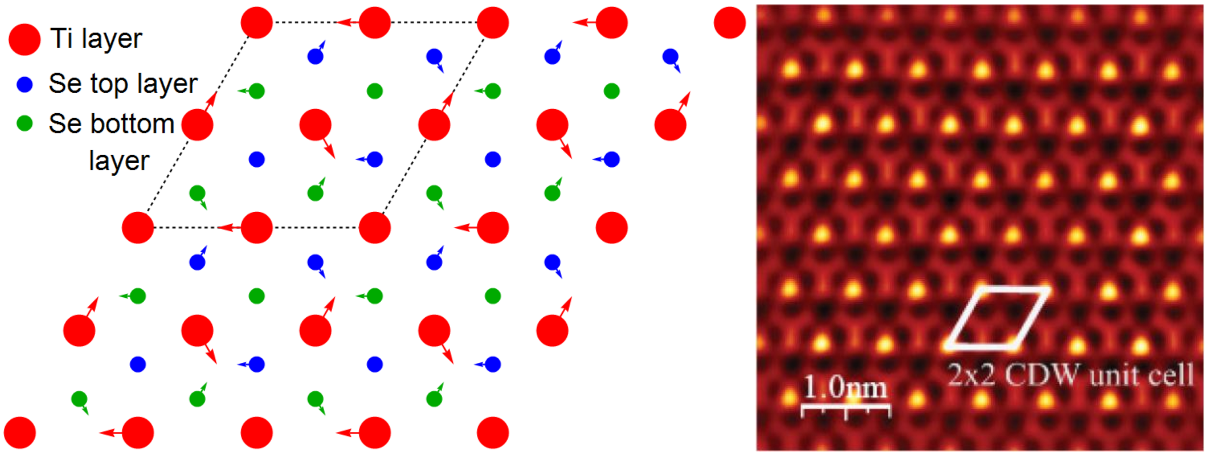

Figure 6.1. The normal-phase structure and CDW phase displacement of 1T-$TiSe_2$. *Left*: representation of 1T-$TiSe_2$ structure based on ref. [DiSalvo1976B]. Arrows indicate the displacement of atoms in the low-temperature CDW phase. Displacements have been exaggerated for effect. The dashed lines show the deformed unit cell. *Right*: atomic resolution STM image of 1T-$TiSe_2$ at 77 K [Cazzaniga2012].

Compared to the 1T-TaS_2, the periodic lattice distortion/CDW transition in 1T-$TiSe_2$ is markedly different [Rossnagel2011]. For instance, a commensurate superlattice forms without the occurrence of an incommensurate phase, and there is no hysteresis. At room temperature, the material is in the normal (undistorted) phase. Around 200 K, 1T-$TiSe_2$ undergoes a second-order phase transition to a commensurate 2 × 2 × 2 CDW phase [DiSalvo1976B]. The transition involves a wave vector corresponding to a high-symmetry point L of the Brillouin zone (see Figure 6.2). The atomic displacement pattern within an Se–Ti–Se sandwich is shown in Figure 6.1. At low temperature (77 K), the metal atom displacements are about 0.085 Å, and the ratio of Ti to Se displacements is roughly 3:1. All displacements are parallel to the plane of the layer [DiSalvo1976B].

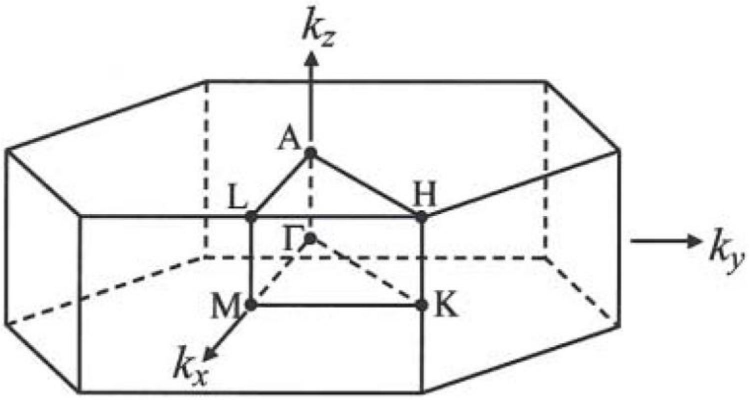

Figure 6.2. High symmetry points of hexagonal first Brillouin zone [Kidd2002].

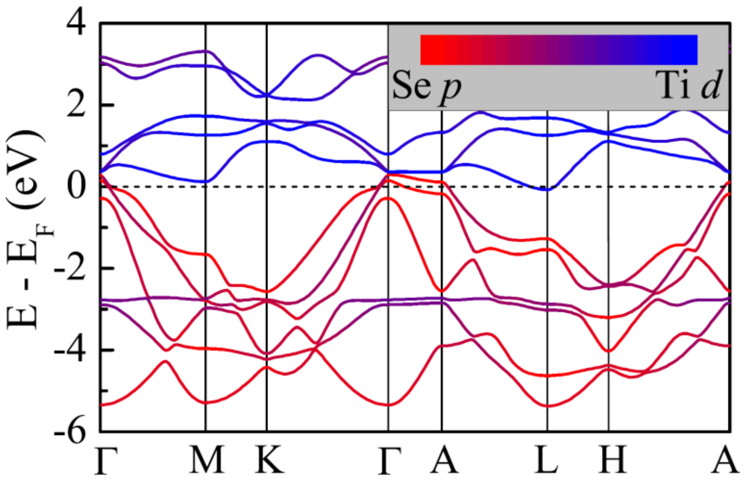

Figure 6.3. Electronic band structure of 1T-TiSe$_2$ in the normal phase [Zhu2014]. Hole pocket is visible at Γ and electron pocket is visible at L.

Band calculations show that, near E_F, the electronic structure of 1T-TiSe$_2$ is governed by two bands, giving rise to the hole-like Se 4*p* derived valence band maximum at the Γ point and the electron-like Ti 3*d* derived conduction band minimum at the L point of the first Brillouin zone [Leventi-Peetz1995, Zhu2014] (Fig. 6.3). These electron and hole pockets can be seen in ARPES measurements (Fig. 6.4).

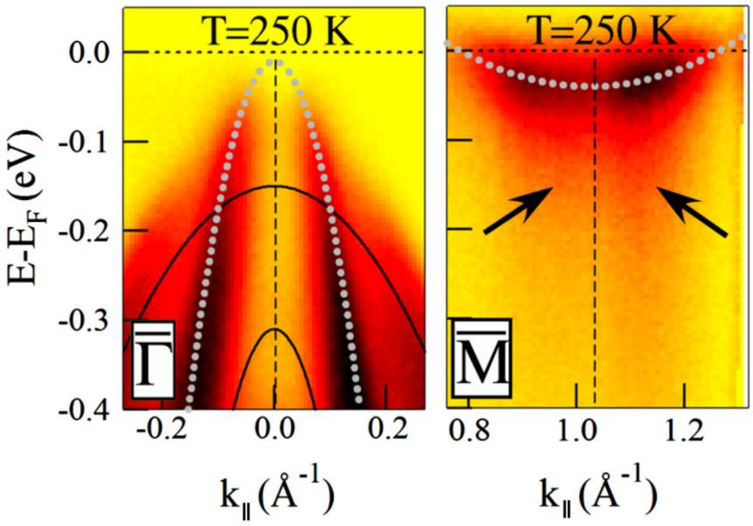

Figure 6.4. ARPES spectra of 1T-$TiSe_2$ above the CDW transition temperature at the Γ and M points of the first Brillouin zone. Thick dotted lines are parabolic fits to the bands in the normal phase [Cercellier2007].

The origin of the CDW order in 1T-$TiSe_2$ has been the subject of a heated debate. Some authors have propagated the idea of traditional Fermi surface nesting [Rossnagel2011], but this is very unlikely due to the shape of the Fermi surface of 1T-$TiSe_2$. Front contenders for the explanation of CDW existence are the excitonic insulator scenario [May2011] and indirect Jahn-Teller effect [Kidd2002]. Relative importance of the electron-electron and electro-phonon interactions is still in dispute [VanWezel2010, Monney2011, Hellmann2012, Castellan2013, Weber2011].

Even the seemingly easy question of semimetallic or semiconducting nature of 1T-$TiSe_2$ does not yet have a definite answer. References [Li2007, Anderson1985] say it is a semimetal with a 120 meV indirect band overlap, with electron and hole pockets at the L and Γ points of the Brillouin zone, respectively [Rohwer2011, Cercellier2007]. References [Rasch2008, Kidd2002] say it is a semiconductor with an indirect band gap of 150 meV. Experimental ARPES spectra show strong band renormalizations with a very large transfer of spectral weight into backfolded bands in the low temperature phase [Cercellier2007].

6.2. Transport and optical properties of 1T-$TiSe_2$

The electrical resistivity parallel to the layers is shown in Figure 6.5. The resistivity exhibits a peak associated with the superlattice formation near 165 K [DiSalvo1976B, DiSalvo1978, Benda1974]. Figure 6.5 also shows Hall coefficient (current parallel and magnetic field perpendicular to the layers). Above the transition temperature, Hall coefficient R_H is positive indicating, within a two band approximation, that hole mobility dominates over electron mobility.

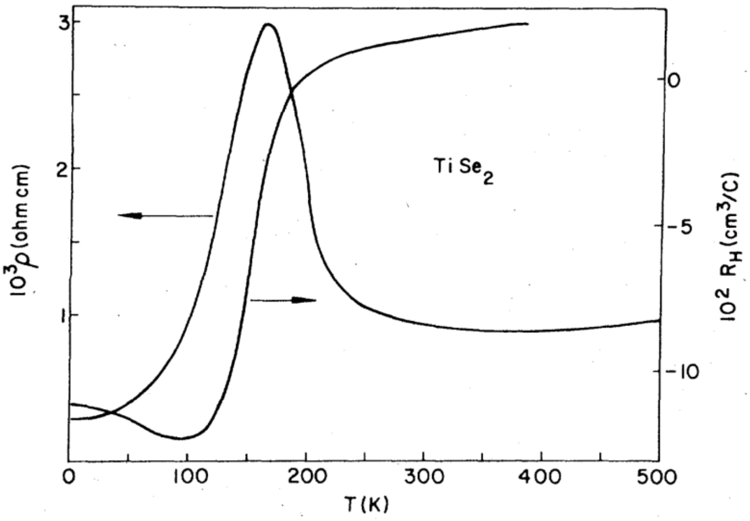

Figure 6.5. Electrical resistivity and the Hall coefficient with the current parallel to the layers for a $TiSe_2$ single crystal [DiSalvo1978].

Transition to the CDW ordered phase modifies the low-frequency optical response of 1T-$TiSe_2$. The CDW-induced energy gap introduces a broad single-particle Se4p-Ti3d interband resonance in the optical conductivity at around 3000 cm^{-1} [Li2007]. At room temperature, collective plasma oscillation of unbound electrons and holes causes a broad maximum at a central energy of around 1200 cm^{-1}. At temperatures below the CDW phase transition, electronic correlations reduce the density of free carriers n by 5 to 10 times, as indicated from the Hall effect, Seebeck coefficient, electrical resistivity, angle-resolved synchrotron ultraviolet photoemission and infrared reflectivity measurements [DiSalvo1976B, DiSalvo1978, Traum1978, Levy1981]. According to ref. [Li2007], this shifts the screened plasmon pole to around 360 cm^{-1}.

Periodic lattice deformation also changes the optical phonon response in a characteristic way. Figure 6.6 shows the reflectivity measured for this work in the frequency range 40 cm^{-1} to 37000 cm^{-1} and temperature range 10 K to 290 K. General features of the 1T-TiSe$_2$ optical spectra have already been described in literature. Above the transition temperature, a single optical phonon resonance at 137 cm^{-1} is observed [Li2007, Holy1977]. Below the transition temperature, backfolding to the Γ point yields additional infrared-active in-plane modes. The extremely high low-frequency reflectivity suggests a semimetal picture of 1T-TiSe$_2$ rather strongly, compared to the semiconductor option.

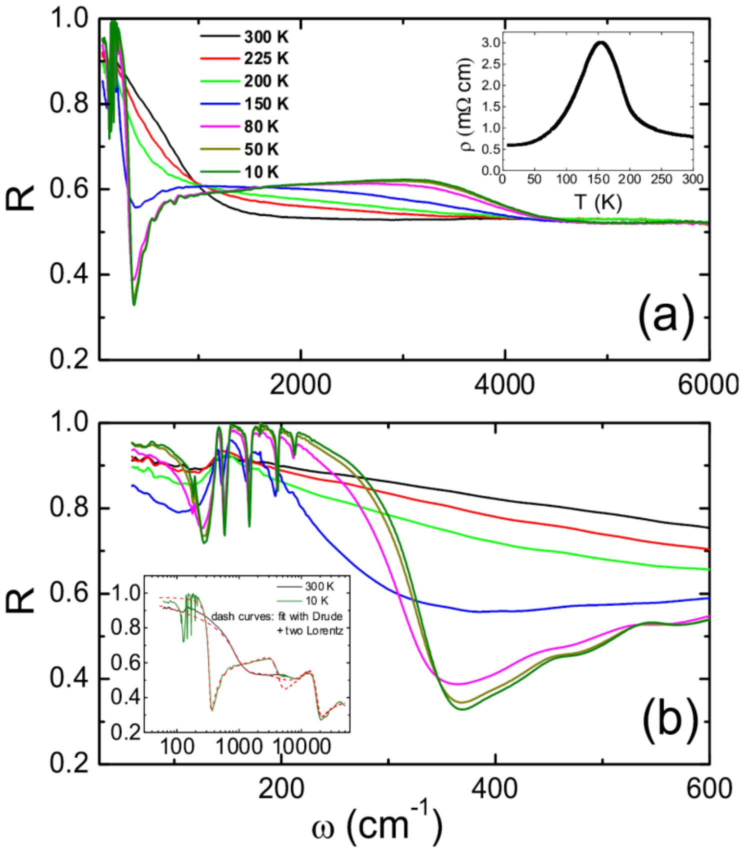

Figure 6.6. *Upper panel*: The temperature dependent $R(\omega)$ in the frequency range from 30 to 6000 cm^{-1}. The inset is the T-dependent DC resistivity. *Lower panel*: The expanded plot of $R(\omega)$ from 30 to 600 cm^{-1}. The inset shows $R(\omega)$ data up to 50 000 cm-1on a logarithm scale. Dashed curves are [Li2007] fits to a simple Drude-Lorentz model. [Li2007]

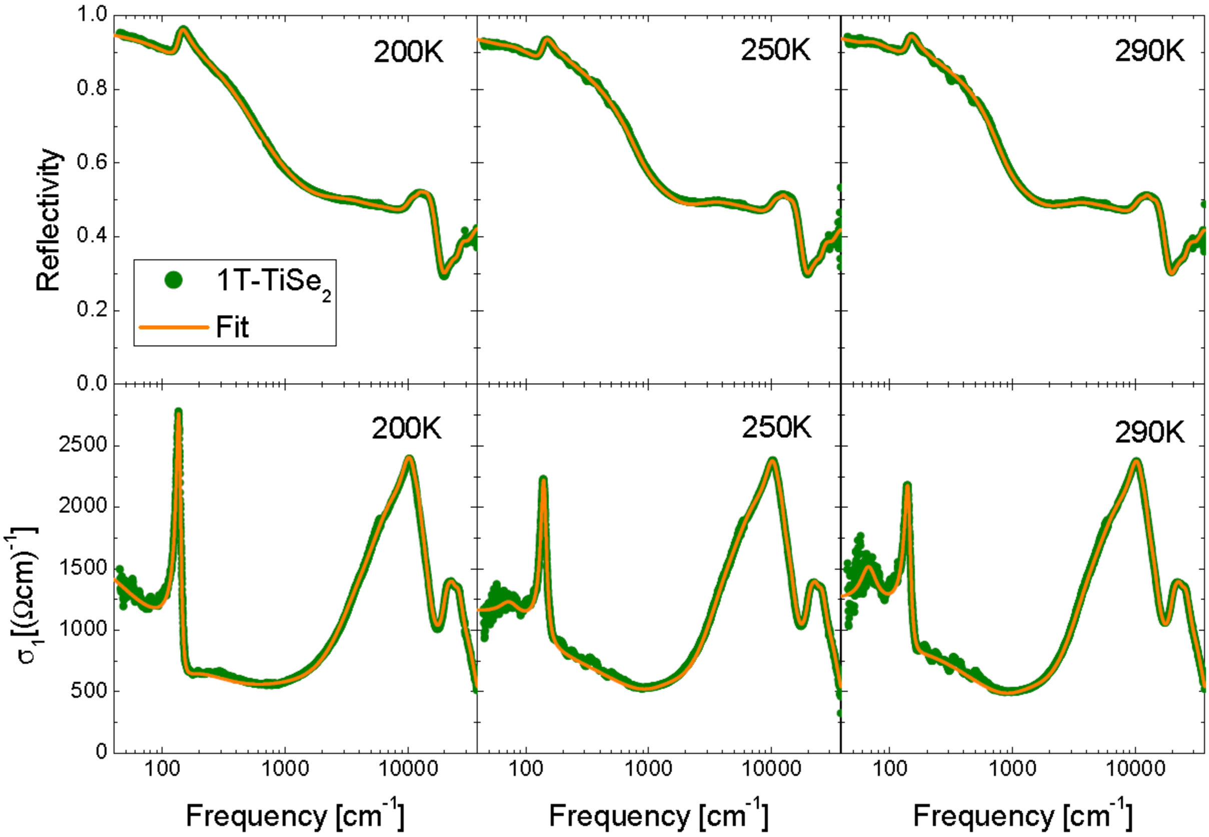

Figure 6.7. Temperature dependent measured reflectivity (upper row) and optical conductivity (lower row) of 1T-TiSe$_2$ (green circles) in the normal (undeformed) phase. Kramers-Kronig consistent fit to the data is shown with solid orange curves (see text for details).

The experimental results for the reflectivity of the compound above phase transition are shown in Fig. 6.7, along with the calculated real part of the optical reflectivity and the simultaneous fit to both sets of data using the modified Drude-Lorentz model described later in the text. Measurements have been performed in such a wide frequency range specifically to eliminate the possibility of artificially introduced artefacts during the calculation of the optical conductivity. This, in combination with the in situ gold evaporation procedure, gives us highly reliable data for the low-frequency optical conductivity.

Our data concurs with ref. [Li2007] that reflectivity shows a distinctly metallic character. Following previous optical investigations of 1T-TiSe$_2$, it would be standard to fit our data by using a simple model with one Drude for the low frequency intraband excitations and

Lorentzians for the interband and phonons as in ref. [Li2007]. This procedure gives only an approximation of the measured data and examination of the best fit by Li et al. to their measured reflectivity in the normal phase (shown in Fig. 6.6, inset of the lower panel), actually shows that they were unable to correctly capture the behavior of the whole intraband related frequency region.

Band picture given in the introduction to 1T-TiSe$_2$ gives us the physical background to think that the fitting model should be changed. Namely, since there are both electron and hole pockets present at the Fermi level, we would expect they would both contribute to the low frequency optical conductivity. In other words, one needs to use a two-band model to correctly show the low frequency behavior. It should be noted that H. P. Vaterlaus and F. Lévy have indeed noticed that they could describe two frequency regions of the intraband related background of the reflectivity curve only by selecting two different damping values. In this way, using the one-band model, they could choose to fit better either the region lower or higher in frequency, but not both. However, they failed to make the connection to the two-band model. Two band model has also been used by Di Salvo *et al*. ([DiSalvo1976B, DiSalvo1978]), to explain the temperature dependent Hall coefficient of 1T-TiSe$_2$.

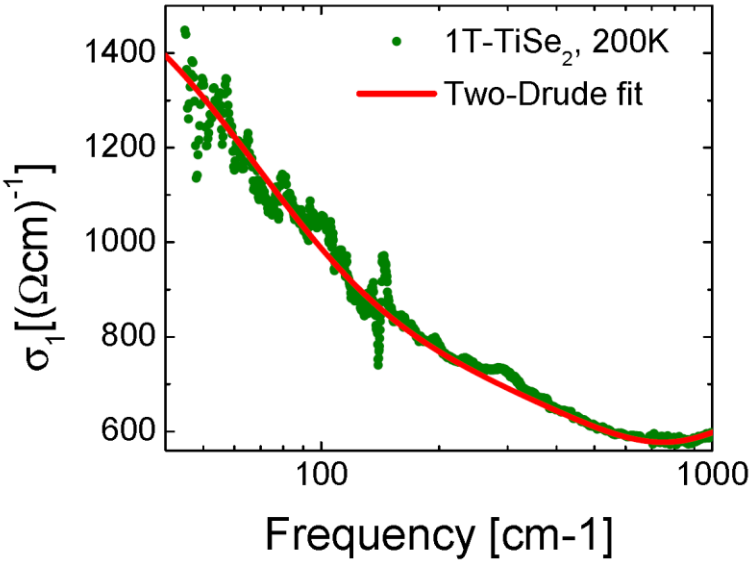

Figure 6.8. Optical conductivity of 1T-TiSe$_2$ at 200 K with the asymmetric phonon peak subtracted. Red curve shows two Drude terms are both necessary and sufficient to obtain a fit to the experimental data.

To illustrate the two-band nature of the intraband region further, we turn to our data at 200 K. It is the lowest measurement we have in the normal phase, so in this way we minimize the temperature related noise in the measurements. One thing that stands out in the 200 K optical conductivity is the strong asymmetry of the phonon mode sitting right on top of the intraband. We have used the Fano model described in Chapter 1 to subtract the asymmetric peak from the experimental data. The result is shown in Figure 6.8. The phonon mode has been successfully removed and a fit using two Drude terms drawn to emphasize that two Drude terms are both necessary and sufficient to obtain a fit to the experimental data. Notice that the intraband related optical conductivity curve has a break near 132 cm^{-1}. This is not an artefact of the Fano procedure because if we subtracted the asymmetric phonon too much or too little, the result would still be asymmetric. The curve would have a higher value on one side and a lower value on the other side, with a step between them. Since there is no combination of parameter values that could produce the observed break in a one-band Drude term, we conclude based on Figure 6.8 that there are at least two Drude-like contributions in the intraband region of the optical curves. In other words, two-band model is the minimum viable model of the optical properties of 1T-TiSe$_2$.

6.3.1. Effect of degeneracy on the band model

The reason we remain careful about the number of bands actually present is degeneracy. If a band is degenerate, consisting of several sub-bands with identical fit parameters, we will not be able to discern the actual number of sub-bands from optical conductivity alone. We will actually see a normal Drude-like intraband with damping equal to the damping of each sub-band and with a spectral weight equal to the sum of spectral weights of individual sub-bands. The question is how this affects our calculations based on the extracted optical data.

Consider the case where one band per charge carrier species crosses the Fermi level. Considering that 1T-TiSe$_2$ has one electron band and one hole band at the Fermi level, we will restrict ourselves to these two charge carriers (if there would be another hole or electron band at the Fermi level with different parameters, its carriers would need to be counted as an additional carrier species). If a band is degenerate, then the connection between the measured spectral weight of the band SW_α (given in SI units, hence the $1/4\pi\varepsilon_0$ in the equation) and the carrier density $n_{\alpha i}$ and mass $m^*_{\alpha i}$ of each degenerate sub-band is given by

$$\frac{8}{4\pi\varepsilon_0} SW_\alpha = \omega_{p,\alpha}^2 = \sum_{i=1}^{d_\alpha} \frac{n_{\alpha i} e^2}{\varepsilon_0 m_{\alpha i}^*}, \quad \alpha = e, h$$

where *i* sums over the degenerate sub-bands, d is the degeneracy, *c* is the speed of light, e is the charge of an electron and ε_0 is the dielectric constant of vacuum. Index α labels an electron or a hole degenerate band.

For a degenerate band:

a) $m_{\alpha i}^* = m_\alpha^*, \forall i \in [1, d]$ because $m_{\alpha i}^* = \hbar^2 \left(\frac{d^2 E}{dk^2}\right)^{-1}$ ($m_{\alpha i}^*$ is inversely proportional to the curvature of the band; if the curvature of the bands, and hence the effective mass, would be different, the sub-bands would not be degenerate)

b) $n_{\alpha 1} = n_{\alpha 2} = \cdots = n_{\alpha d} \equiv n'_\alpha$ (the carrier densities of degenerate sub-bands are identical)

c) $\sum_{i=1}^{d} n_{\alpha i} = d n'_\alpha = n_\alpha$ (the sum over the carrier densities of degenerate sub-bands gives the total carrier density for carriers α, provided only one degenerate band crosses the Fermi level per carrier species)

d) $\mu_{\alpha i} = \mu_\alpha, \forall i \in [1, d]$ because $\mu_{\alpha i} = e\tau_{\alpha i}/m_{\alpha i}^*$ (effective mass and scattering rate of degenerate sub-bands are the same for each sub-band so mobility will be the same for all sub-bands)

Now, using points a) through c)

$$\frac{8}{4\pi\varepsilon_0} SW_\alpha = \frac{n_\alpha e^2}{\varepsilon_0 m_\alpha^*}, \quad \alpha = e, h \tag{6.1}$$

Therefore, degeneracy does not affect the calculation of the total carrier density of carriers α. Calculation is the same as it would be for just two bands.

Hall coefficient for the case of two degenerate bands crossing the Fermi level, one each for holes and electrons is [Kireev1978]

$$R_H = \frac{1}{e} \frac{\sum_{i=1}^{d_h} n_{hi} \mu_{hi}^2 - \sum_{j=1}^{d_e} n_{ej} \mu_{ej}^2}{\left(\sum_{i=1}^{d_h} n_{hi} \mu_{hi} + \sum_{j=1}^{d_e} n_{ej} \mu_{ej}\right)^2}$$

Using points b) through d), as well as $n_h = n_e \equiv n$ for the stoichiometric (i.e. pure) 1T-TiSe$_2$,

$$R_H = \frac{1}{e}\frac{n_h\mu_h^2 - n_e\mu_e^2}{(n_h\mu_h + n_e\mu_e)^2} = \frac{1}{ne}\frac{1-\frac{\mu_e}{\mu_h}}{1+\frac{\mu_e}{\mu_h}} \tag{6.2}$$

Again, degeneracy does not affect the final equations (unless we are specifically interested in carrier densities of degenerate sub-bands) and calculation is the same as it would be for just two bands. This is an important finding when extracting conclusions from the optical data for 1T-TiSe$_2$ because we know for certain that the electron band is threefold degenerate (there is one electron pocket at the L point, but there are three non-equivalent L points). Even more importantly, there is a possibility that the hole band is twofold degenerate, but spin-orbit coupling might remove this degeneracy. Unfortunately, we are not aware of any papers answering this question conclusively. The result of this chapter assures us that this will not affect our fitting and calculations as long as we are not concerned with the properties of an individual degenerate sub-band.

6.3.2. Two-band model of the normal phase

Analysis of our optical data within the two-band model allows us discern not only the spectral weight belonging to the hole and electron band but also, for the first time, the scattering times of each carrier channel. This was inaccessible to the transport measurements such as [DiSalvo1978]. Figure 6.7 shows our fits within the two-band model to the measured reflectivity and calculated optical conductivity. We used two Drude terms to fit the intraband region (labeled Drude 1 and Drude 2 for now), one Fano peak to fit the asymmetrical phonon mode and a number of Lorentzians to fit the interband transitions at higher frequencies. To obtain satisfactory fits to the experimental data we had to add a Lorentzian term at low frequencies (below the phonon mode). This term shows a critical behavior where the resonant frequency of the term goes to zero as the temperature is lowered. More work is needed to understand the nature of this term. Initial rough fits have shown that the spectral weight of Drude 2 term is always larger than the spectral weight of Drude 1 term in the normal phase.

At 290 K the ratio of spectral weights is around 9. Using the relation between spectral weight and plasma frequency we get

$$\frac{1}{4\pi\varepsilon_0}SW_i = \frac{\omega_{p,i}^2}{8} = \frac{1}{8}\frac{ne^2}{\varepsilon_0 m_i^*}, \qquad i = 1,2 \tag{6.3}$$

Notice that we have introduced the assumption of stoichiometry of the sample so the charge carrier densities of the bands are assumed to be the same, $n_1 = n_2 = n$. Now we can see that the ratio of spectral weights is

$$\frac{SW_2}{SW_1} = \frac{m_1^*}{m_2^*} = 9 \pm 1 \tag{6.4}$$

As explained in the introduction, we expect one of these bands to be the electron pocket and the other to be the hole pocket. It should be noted here that, unlike the hole pocket with its cylindrical Fermi surface, the electron pocket of 1T-TiSe$_2$ is given in reciprocal space by a Fermi surface ellipsoid. This means that effective mass of electrons in 1T-TiSe$_2$ is anisotropic, so what exactly would m_e^* represent in (6.4)? It is standard in conductivity related calculations to approximate the anisotropic effective mass of a band with the simple harmonic mean [Ziman1960]

$$\frac{1}{m^*} = \frac{1}{3}\left(\frac{1}{m_1^*} + \frac{1}{m_2^*} + \frac{1}{m_3^*}\right)$$

where m_1^*, m_2^* and m_3^* are the effective masses of electrons along the three principal directions of the electron pocket Fermi surface ellipsoid. In 1T-TiSe$_2$ the situation is a little complicated by the fact that the electron pocket ellipsoid is tilted in relation to the TiSe$_2$ layers (long principal axis of the ellipsoid points in the Γ-L direction of the hexagonal first Brillouin zone). Our optical measurements were done by exposing the sample to electromagnetic wave propagating in a direction normal to the layers. This means that we actually probed the electrons with effective masses belonging to an in-plane projection of the actual electron pocket ellipsoid. Moreover, as conductivities are additive, spectral weight is equal to the integral of the real part of conductivity and effective mass is inversely proportional to both, electrons with the smallest effective mass will make the largest contribution to the optically determined spectral weight. Therefore, we expect our optically determined effective electron mass to be close to the light electron mass determined from ARPES in the L-H direction, instead to the harmonic mean predicted by [Ziman1960].

ARPES measurements at 260 K from [Kidd2002] estimate the hole mass as $m_h^* = -0.29m_0$ (m_0 is the rest mass of a free electron), heavy electron mass as $m_e^* = 6.42m_0$ (measured along L-A) and light electron mass as $m_e^* = 2.8m_0$ (measured along L-H). It is straightforward to see that

$$\left.\frac{m_{e,light}^*}{m_h^*}\right|_{[Kidd2002]} = 9.66, \qquad \left.\frac{m_{e,heavy}^*}{m_h^*}\right|_{[Kidd2002]} = 22.1$$

References [Pillo2000] and [Rossnagell2002] agree that the heavy electron mass is much bigger than the hole mass, giving estimates of the $m_{e,heavy}^*/m_h^*$ ratio of 16 and 19.4, respectively. This allows us to identify band 1 in our two-band model as an electron band and band 2 as a hole band so that our optical measurements give

$$\frac{m_e^*}{m_h^*} = 9 \pm 1 \tag{6.5}$$

As we have expected, our ratio is in excellent agreement with the [Kidd2002] ratio for the light electron effective mass.

To refine the temperature dependent fits of the optical data, we have imposed some restraints based on transport measurements. Firstly, the sum of optical conductivities of the two fitted bands normalized to the value at 290 K, $\sigma_{TOT}(\omega = 0, T)/\sigma_{TOT}(\omega = 0{,}290K)$, has to follow the temperature dependence of the measured dc conductivity, $\sigma_{dc}(T)/\sigma_{dc}(290K)$. Secondly, looking at the expression (6.2), we see that by using the approximation of a constant charge carrier density and ratio $R_H(T)/R_H(290K)$, we get the relative reduction factor from Hall coefficient measurements from which the mobility ratio can be calculated. We use the Hall coefficient data from ref. [DiSalvo1978]. Mobility of charge carriers in a band is given by

$$\mu_\alpha = \frac{e\tau_\alpha}{m_\alpha^*} = \frac{1}{2\pi c}\frac{e}{m_\alpha^*\gamma_\alpha}, \quad \alpha = e, h$$

which means that the mobility ratio for electron and hole bands is

$$\frac{\mu_e}{\mu_h} = \frac{m_h^*\gamma_h}{m_e^*\gamma_e} \tag{6.6}$$

Figure 6.9 displays the fitting parameters (spectral weight and damping) of both Drude terms at 200, 225, 250 and 290 K. There is a large difference in the spectral weight of bands. Damping of the bands also shows a clear separation, with damping of the hole band being approximately 5 times larger than the damping of the electron band. We can see that the damping of both bands is increased as the temperature is lowered, but the rate of increase is higher for the hole band.

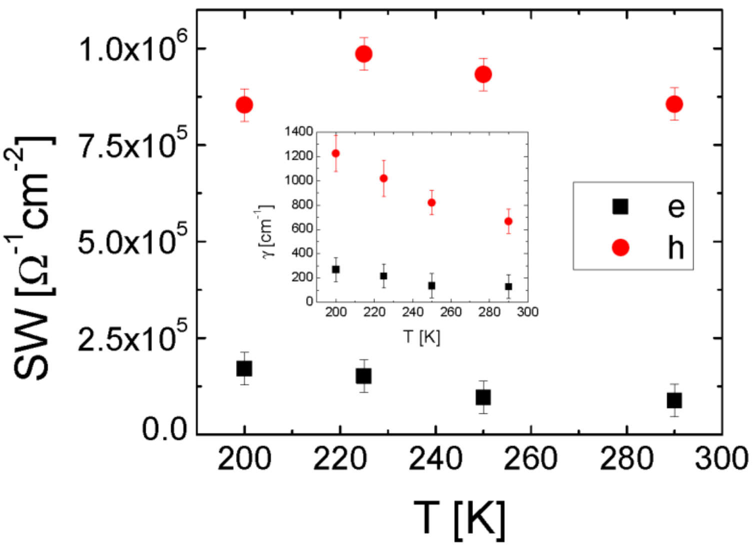

Figure 6.9. Parameters of the Kramers-Kronig-consistent fit to the experimental optical data for the 1T-TiSe$_2$ in the normal phase. *SW* is the spectral weight (in Ω^{-1}cm^{-2}) of the Drude term defined as $SW/4\pi\varepsilon_0 = \omega_p^2/8$, where ω_p is the plasma frequency. *Inset*: scattering rates of the two Drude contributions. γ is the width (or damping) of the Drude term in cm^{-1}, defined through the scattering time τ as $\tau^{-1} = 2\pi c\gamma$.

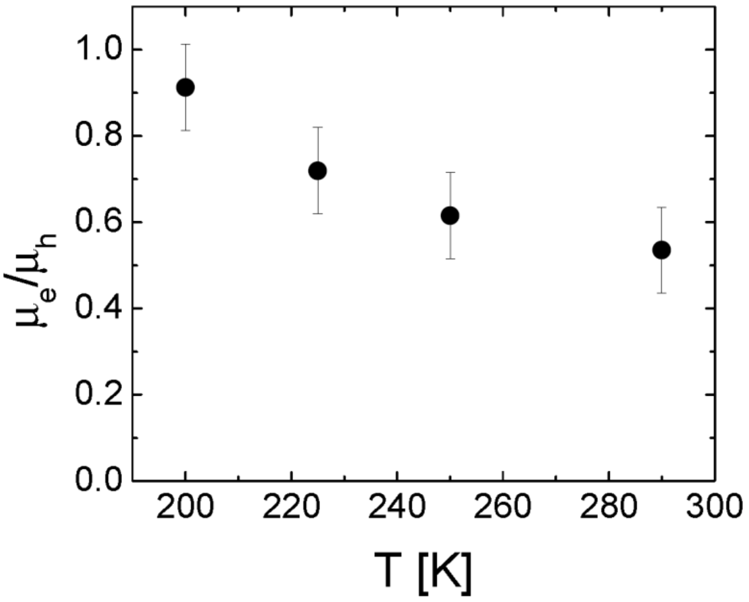

Figure 6.10. Temperature dependent ratio of the electron and hole mobility based on the fit to the measured optical data. According to equation (6.2), this temperature dependence takes the Hall coefficient to zero around 200 K as the temperature is lowered, in accordance with the [DiSalvo1978] measurements.

We aim to estimate the width of the carrier bands using the quasi-two-dimensional approximation for the treatment of 1T-TiSe$_2$. Even though this is a standard assumption for this material in literature, some caveats must be made. According to DFT calculations, quasi-two-dimensional approximation is more than adequate for the hole pockets but, as it was stated earlier, Fermi surface of the electron pocket is an ellipsoid meaning it has a 3-dimensional character. Therefore, we will restrict ourselves to calculating the width of the hole band. Expression for the charge density in a quasi-two-dimensional band is

$$n_{2D} = g_{2D}\Delta E$$

$g_{2D} = m^*/\pi\hbar^2$ is the density of states for the band and ΔE is the band width. n_{2D} is the charge density within one layer of 1T-TiSe$_2$, and we can get it by multiplying the bulk charge density *n* with the lattice constant perpendicular to the layers (i.e. 6Å).

If we compare the above expression which includes the band width to the expression for the spectral weight (6.3), we see that both are actually proportional to the ratio n/m^* and

$$\Delta E_h = \frac{\pi\varepsilon_0\hbar^2}{e^2} d_\perp \omega_{p,h}^2 = \frac{2\hbar^2}{e^2} d_\perp SW_h \tag{6.7}$$

$d_\perp$ is the lattice constant perpendicular to the layers and SW_h is the spectral weight of the hole band determined from optical measurements. Therefore, the band weight of a two-dimensional band can actually be calculated from the spectral weight of the band determined from optical measurements, without using any mass or carrier density data from literature. Lattice constant perpendicular to the layers is the only information specific for the material we need from other measurements. Values calculated directly in this way are given in Table 6.1. With an assumed error in SW of around 20%, error in energy is 10 meV and error in equivalent temperature is 116 K.

To produce occupancy of the valence band by holes in the case of a small-gap semiconductor, we would need to provide thermal excitation equivalent to $\Delta E + E_G = \Delta E_e + \Delta E_h + E_G$, where E_G is the semiconductor gap. Since the temperature equivalent ($E = k_B T$) to the energy of 53 meV is 608 K, it is quite evident that the temperature of 290 K is not nearly enough to produce thermal excitation necessary for optical measurements such as ours in the semiconductor scenario, even if we neglect both the E_G and ΔE_e. The same argument holds for other temperatures presented in Table 6.1. Therefore we conclude that our sample must be a semimetal, with an overlap of the electron and the hole bands, because temperature excitation at the measured temperatures does not provide enough energy for carriers to populate even the hole band, let alone cross a gap that would be present if the material was a semiconductor.

Table 6.1. Measurement temperature, calculated hole band width and the equivalent temperature ($\Delta E = kT$).

T [K]	ΔE [meV]	eq. T [K]
200	52	607
225	60	700
250	57	663
290	52	608

As we have mentioned before, there is a possibility (based on DFT calculations) that the hole band is doubly degenerate. In that case, the width of each degenerate sub-band is half of the values listed in Table 6.1. This would somewhat weaken the conclusion for 290 K, but at lower temperatures the band width is still too large to support the temperature enabled population of the hole band in the semiconductor picture of the material.

It is worth comparing the equivalent temperatures of the hole band width to the temperatures equivalent to the scattering of holes. Equivalent temperature for hole scattering is between

Notice that the damping of the hole band is above 660 cm-1 (950 K equivalent temperature) for all measured temperatures, meaning holes are in the limit of strongly scattered fermion gas. In other words, interaction of holes has to be taken into account in the normal phase.

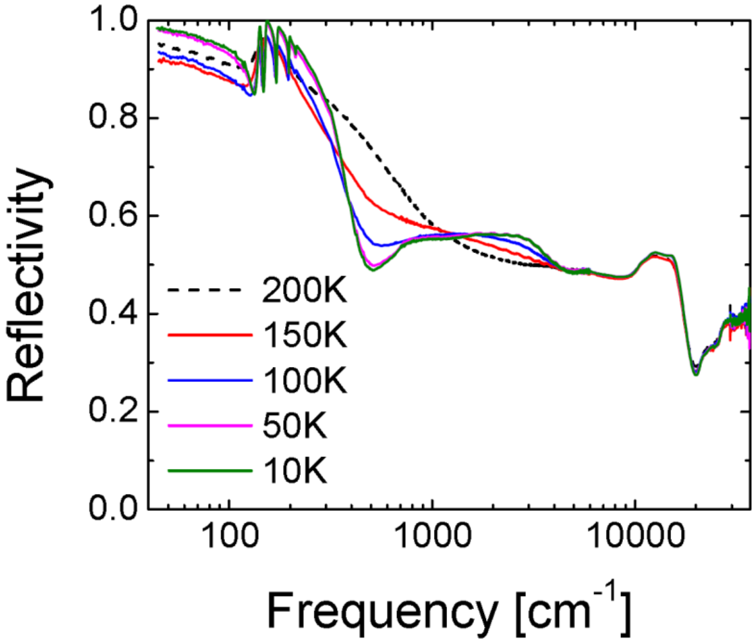

Figure 6.11. Temperature dependent measured reflectivity of 1T-TiSe$_2$ in the CDW phase (solid lines). Measurement in the normal phase, at 200 K (dashed line), is shown to emphasize the change between the normal and CDW phase.

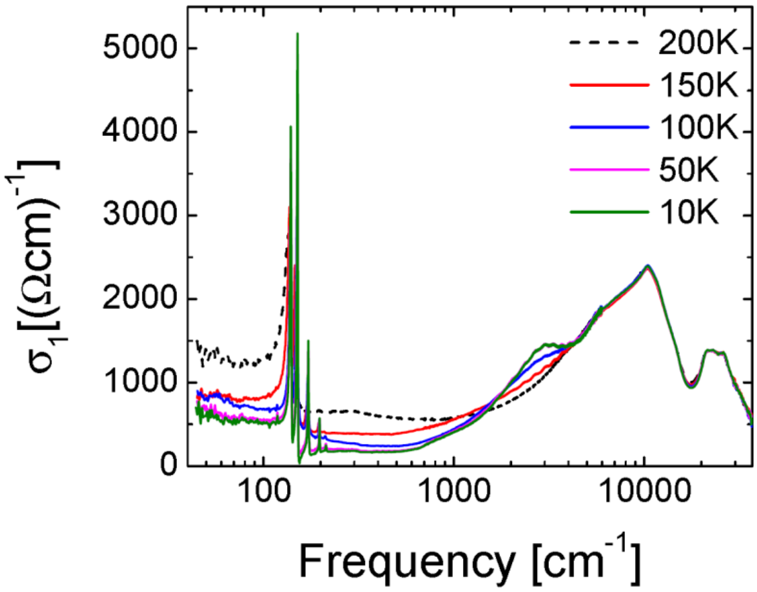

Figure 6.12. Temperature dependent calculated real part of optical conductivity of 1T-TiSe$_2$ in the CDW phase (solid lines). Kramers-Kronig consistent fit to the data is shown with solid orange curves (see text for details). Measurement in the normal phase, at 200 K (dashed line), is shown to emphasize the change between the normal and CDW phase.

The experimental results for the reflectivity and the calculated real part of the optical conductivity of the compound below phase transition are shown in Fig. 6.11 and Fig. 6.12, respectively. The complete analysis and fitting of the CDW phase is a work in progress and falls under the outlook for this work. Here, only the measured reflectivity, calculated optical conductivity and a brief initial analysis will be presented.

As already shown in literature [Levy1981, Li2007], there are five phonon modes in the CDW phase. Based on their grouping, we conclude that all of the modes that appear in the CDW phase are split-off from the original single mode in the normal phase. Unlike the 1T-TaS$_2$, there is no separate phonon group at lower frequencies in the CDW phase of 1T-TiSe$_2$. We cannot perform the analysis described in Chapter 5 on the phonon modes of 1T-TiSe$_2$ because the starting assumption there was that the Ta orbital dominates the Fermi level and S orbital contribution to the density of states is negligible. Here, Se orbitals have a non-negligible contribution to the density of states at the Fermi level.

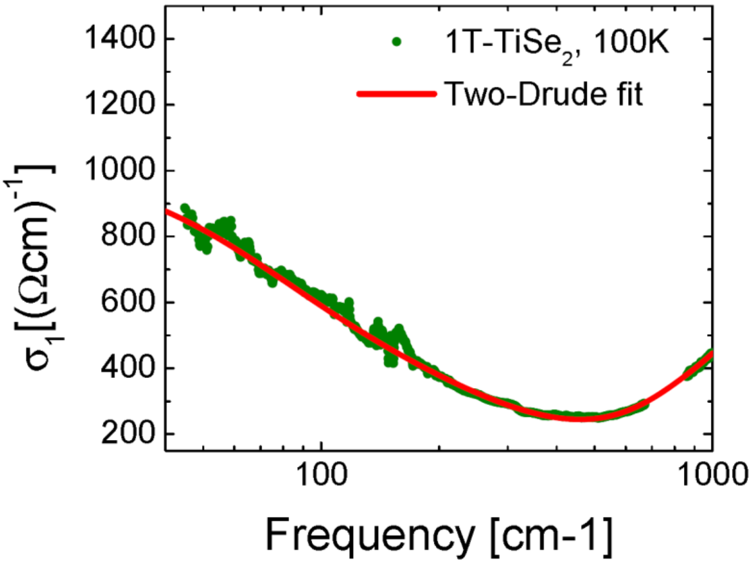

Figure 6.13. Optical conductivity of 1T-TiSe$_2$ at 10 K with the asymmetric phonon peaks subtracted. Red curve shows two Drude terms might be applicable when fitting to the experimental data in the CDW phase.

Below the phase transition the bands are refolded back onto the Γ point, making the band structure and the appropriateness of the two-band model used in the normal phase unclear. However, as the rough fit using two Drude terms shows in Figure 6.13, there are indications that the model using two Drude terms might be applicable in the CDW phase as well. More work is needed to verify such possibility.

6.5. Effects of doping

CDW in 1T-$TiSe_2$ was found to be suppressed by hydrostatic pressure around 5 GPa [Joe2014, Kusmartseva2009, Snow2003] as well as intercalation of copper atoms [Morosan2006], causing superconductivity to emerge. Even self-doping effects for crystals grown at different temperatures can strongly perturbate the CDW phase by introducing structural defects such as intercalated Ti atoms, Se vacancies, and Se substitutions by residual iodine and oxygen (depending on growing procedure) [Hildebrand2014, DiSalvo1976B]. Intercalations by Fe, Eu and Pd have also been studied [Cui2006, Danzenbacher2000, Morosan2010], as well as Ti substitutions by Ta, Nb and Hf [DiSalvo1978, Benda1974, Borghesi1984] and Se substitutions by S and Te [Caille1983, Freund1984, May2011].

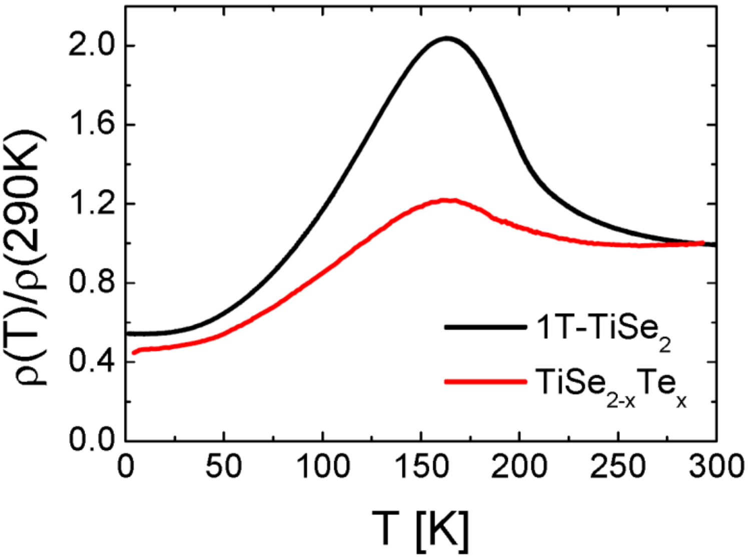

Figure 6.14. Comparison of temperature dependent measured resistivity of 1T-$TiSe_2$ and 1T-$TiSe_{2-x}Te_x$ (x = 0.03), normalized to their 290 K values.

We have investigated the optical response of Te doped 1T-$TiSe_2$, $TiSe_{2-x}Te_x$, where $x = 0.03$. Electrical resistivity curves of the pure and doped $TiSe_2$ are shown in Figure 6.14. We can see that 1.5% substitution of Se with Te dampens the CDW related peak, but it is not suppressed to lower temperatures. The CDW peak, although wider, is still clearly discernable.

Considering that $TiSe_{2-x}Te_x$, where $x = 0.05$ has a metallic electrical resistivity without a trace of the CDW related peak [May2011], we conclude that the critical Te substitution is between 1.5% and 2.5%.

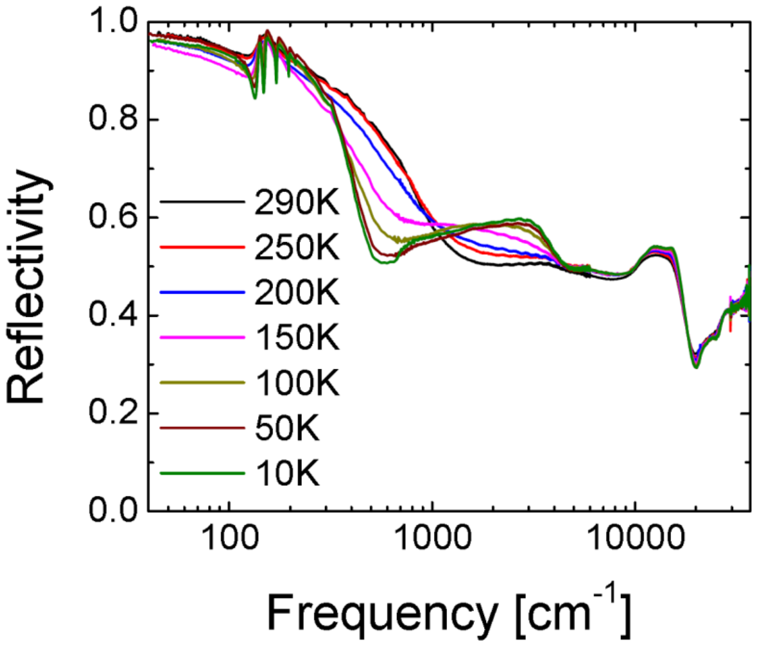

Figure 6.15. Temperature dependent measured reflectivity of 1T-$TiSe_{2-x}Te_x$, $x = 0.03$.

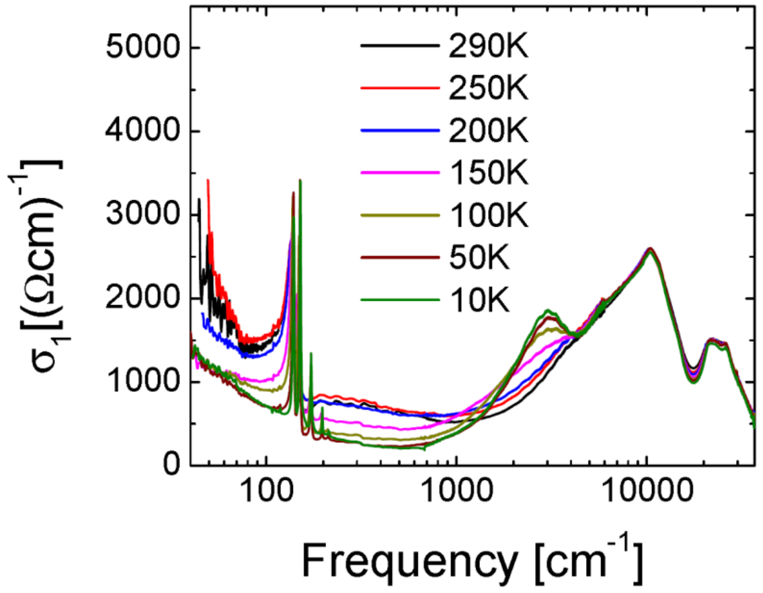

Figure 6.16. Temperature dependent real part of optical conductivity of 1T-$TiSe_{2-x}Te_x$ obtained through Kramers-Kronig analysis.

The same fitting procedure used for the pure 1T-$TiSe_2$, was used here. The complete analysis of the doped sample falls outside the scope of this thesis. Reflectivity of the doped sample also shows a highly metallic character both below and above the transition temperature. As indicated by the peak in the electrical resistivity, CDW transition is present in the doped sample. This is evident from the splitting of the normal phase phonon mode into five low temperature modes. Our initial fits again suggest that two bands (modeled by two Drude contributions) are essential to get a good fit of both reflectivity and real part of optical conductivity in the normal phase, but more work is needed to confirm this.

6.6. Conclusions of Chapter 6

This chapter presents the first experimental study of the optical response of pure and doped 1T-TiSe$_2$ in which high quality of the optical data permits for the precise separation of the components in the optical continuum (coming from free carriers) and the optical phonons which come on the top of this continuum. The coupling of optical phonons and the continuum clearly manifests itself through the pronounced asymmetric (Fano) shape of the phonon signals. This work presents a detailed analysis of the normal phase of pure 1T-TiSe$_2$. The parameters of the phonon mode present in the normal phase are determined. Further investigation is necessary to see if this data may be used to conclude on the charge re-distribution in the charge density wave state, as it was done for the first time in this thesis for 1T-TaS$_2$. At the moment the non-negligible contribution of the Se orbital to the density of states at the Fermi level presents a problem. Measurements on the CDW phase of pure 1T-TiSe$_2$ as well as measurements on both phases of the doped sample are presented. More work is needed to confirm that the findings of the normal phase extend to the CDW phase and to the doped material.

This work represents the first study which clearly resolves the separate contribution of two types of carriers in 1T-TiSe$_2$ in the intraband optical continuum of the normal phase. Our data provides the spectral weight of two components as well as their scattering rates in a wide temperature range. This is expected to help in determining the true nature of the low temperature state, where some exotic mechanisms, including the excitonic condensate phase, have been proposed in recent years. In this work, however, we confined our microscopic analysis of the two-component signal to the normal, high temperature phase. The motivation for this is twofold. First, the ARPES studies and DFT calculations in 1T-TiSe$_2$ provide a clear foundation for the two-component picture in the high temperature phase, in terms of hole and electron pockets. Second, normal state sets the stage for the instability, and our measurements are the first to resolve the separate contributions of electron and hole pockets to conductivity and separately determine their scattering rates. From our data we are able to independently determine the compensation factor in the Hall effect. This work has shown that the band width of the hole band in 1T-TiSe$_2$ can be estimated directly from the optical measurements. In this way we have shown that the semiconductor picture of this material is not realistic because the thermal population of the hole band would require temperatures more than double than the ones measured. Our conclusion is that 1T-TiSe$_2$ in the normal phase must therefore be a semimetal, with an overlap of the hole and electron bands.

CONCLUSIONS

This thesis deals with the diverse physical background of layered transition metal dichalcogenides as seen in two selected materials, 1T-TaS_2 and 1T-$TiSe_2$. Both have layers, both have the same undistorted intra-layer structure, both experience charge density waves, yet they have vastly different physical properties.

1T-TaS_2 has a complicated phase diagram, but our focus is on two of the phases: the low-temperature CCDW phase with the star-like superstructures and the room-temperature NCCDW phase with a nano-sized regular mosaic of semiconducting and metallic domains. These phases show striking examples of complex superstructuring that a simple Peierls mechanism can produce. We looked at the pure material and one doped with less than 0.1% copper. Doping suppresses the CCDW/Mott transition completely and the sample remains in the NCCDW phase down to the lowest temperatures measured in this work. This allowed us to make a direct comparison of the phases at low temperatures, as well as the first ever detailed examination of optical properties of the NCCDW phase of 1T-TaS_2 at low temperatures. The NCCDW phase shows a puzzling lack of low-frequency spectral weight, as inferred from DFT calculations for the metallic domains. This work shows that the nano-textured NCCDW phase cannot be analyzed within the simple homogeneous Drude-Lorentz model. Instead, effectively nano-composite nature of the phase has to be considered when developing a model of the optical response. We chose Bruggeman effective medium theory (EMT) as the simplest model of optical properties able to deal with a nano-textured system near the edge of percolation. In particular, the 3-component Bruggeman EMT model was shown to satisfactorily model the measured optical response, confirming that connections between the metallic areas also play an important role in the properties of the NCCDW phase, as well as metallic and semiconducting domains. This was already suspected from the discrepancy between the transport measurements and the DFT calculations, but our EMT models for the first time explicitly show that nano-texturing effects are responsible for the loss of the low-frequency spectral weight in the optical response of the NCCDW phase. Additionally, the existence of the localized surface plasmon (LSP) in the optical response of the NCCDW is established for the first time. LSP adds significant spectral weight to the optical conductivity of interband peaks lowest in frequency. EMT also successfully explains the asymmetrical phonon response found in the measured optical data as another consequence of the nano-texturing. While focusing on the phonon modes of 1T-TaS_2, we have developed a novel analysis which enables us to determine the redistribution of charge over the star-like superstructure from the spectral weight of Ta-related phonon modes.

1T-TiSe$_2$ has a much simpler phase diagram with only two phases and no hysteresis. However, it does not suffer a lack of unsolved problems. At low temperatures the material is in a commensurate CDW phase similar to the CCDW phase of 1T-TaS$_2$. Unlike 1T-TaS$_2$, Peierls mechanism is very unlikely to be responsible for the CDW in 1T-TiSe$_2$ due to the shape of the Fermi surface. More likely candidates are excitons and Jahn-Teller effect, but the true origin of the CDW in 1T-TiSe$_2$ is still unresolved. We have therefore concentrated our efforts to better understand the normal undistorted phase, above 200 K, as it sets the stage for the low-temperature superstructuring. Prominent features of the normal phase which are expected to impact the properties of the material are the hole and electron pockets. Known degeneration of the electron band and suspected degeneration of the hole band also point to a more complex physical picture than single-band model might provide. Although the need to model the intraband excitations using multiple band theory has been hinted at in some optical works, the connection was never explicitly made. This work for the first time establishes the two-band model, with electrons and holes as charge carriers, as the minimal required and sufficient model of the optical properties of 1T-TiSe$_2$ in the normal phase. Whether this material is a semiconductor with an indirect band gap or a semimetal with an indirect band overlap is a matter of dispute in the literature. This model allows us to make an estimate of the width of the hole band and in turn provides an estimate of the minimum temperature needed for thermal excitation to be responsible for the measured optical data, as suggested by the semiconducting model. Our work shows that the estimated temperature is more than twice the actual measured temperature. Actual difference is even higher since we were did not include the gap or the width of the electron band since we were unable to correctly determine them from our data. We conclude that 1T-TiSe$_2$ is actually a semimetal, with an indirect overlap of the electron and hole bands.

To summarize, this work brings the first ever analysis of the optical properties of the NCCDW phase of 1T-TaS$_2$ at temperatures below 200 K. NCCDW phase is for the first time identified as nano-composite-like and optical response is modeled with a 3-component Bruggeman effective medium theory. This novel approach to the NCCDW phase of 1T-TaS$_2$ accounts for both the lack of spectral weight at very low frequencies and for the surplus spectral weight just below interband. The surplus spectral weight is in this work identified as a localized surface plasmon. This work for the first time shows the asymmetry of the optical phonon modes brought upon by the coupling of spatially distinct nano-sized domains which comprise the material. Asymmetry in the NCCDW phase is explained as an additional effect of the nano-composite optical response. A novel analysis which allows the determination of the charge redistribution over the star-like superstructure in the CCDW phase of 1T-TaS_2 directly from optical measurements of the spectral weights of phonon modes is presented in the thesis. Multiband nature of the electronic state of the high-temperature phase of 1T-$TiSe_2$ was suggested earlier by DFT calculations and transport measurements and even hinted at in some optical works. This work brings the first ever confirmation that the two-band model with electron and hole channels is the minimal sufficient model which can describe the optical properties of the high-temperature phase. Spectral weights and scattering of each channel are for the first time separately determined. Strong scattering of the charge carriers is shown. In this thesis, the band width of the quasi-2D hole band is calculated, allowing to settle the ongoing debate and determine that 1T-$TiSe_2$ in the high-temperature phase is a semimetal.

APPENDIX A

INTRODUCTION TO
OPTICAL PROPERTIES OF SOLIDS

This thesis relies heavily on optical measurements and analysis of optical properties of the investigated samples. Therefore, a brief introduction into the properties and phenomena critical to obtaining the results of the thesis is in order. The following text is based on some standard textbooks on interaction of electromagnetic waves and materials. Reference [Dressel2003] is primarily used, but other sources are also included.

Optical properties of solids can provide information on various phenomena such as energy band structure, impurity levels, excitons, localized defects and lattice vibrations [Dresselhaus2001]. In an experiment, we measure reflectivity, transmission, absorption, ellipsometry or light scattering of a sample. These measurements then allow us to determine the dielectric function $\varepsilon(\omega)$ and the optical conductivity $\sigma(\omega)$.

A.1. Propagation of electromagnetic waves in vacuum

The interaction of electromagnetic radiation with light is fully described by Maxwell's equations [Dressel2003]. If we assume there are no external and induced currents or charge densities, relevant equations in vacuum (in SI units) are

$$\nabla \times \boldsymbol{E} + \frac{\partial \boldsymbol{B}}{\partial t} = 0 \tag{A.1}$$

$$\nabla \cdot \boldsymbol{E} = 0 \tag{A.2}$$

$$\nabla \times \boldsymbol{B} - \frac{1}{c^2}\frac{\partial \boldsymbol{E}}{\partial t} = 0 \tag{A.3}$$

$$\nabla \cdot \boldsymbol{B} = 0 \tag{A.4}$$

E and ***B*** are the vectors of the electric field and the magnetic induction, respectively. The velocity of light in vacuum, c = 2.99792458×10^8 m/s, is in optical calculations usually approximated by $c \approx 3\times10^8$ m/s = 3×10^{10} cm/s. All quantities are position and time dependent (i.e. $\boldsymbol{E} = \boldsymbol{E}(\boldsymbol{r},t)$, $\boldsymbol{B} = \boldsymbol{B}(\boldsymbol{r},t)$).

The combination of equations (A.1), (A.2) and (A.3) yields the following relation for the electric field

$$\nabla^2 \boldsymbol{E} - \frac{1}{c^2}\frac{\partial^2 \boldsymbol{E}}{\partial t^2} = 0 \tag{A.5}$$

This is a wave equation in its simplest form, without dissipation or other complications. If we consider a monochromatic plane wave of frequency $f = \omega/2\pi$ traveling in a direction given by the wave vector $\boldsymbol{q}$, one possible solution of this differential equation is given by a harmonic wave

$$\boldsymbol{E}(\boldsymbol{r}, t) = \boldsymbol{E}_0 e^{i(\boldsymbol{q}\cdot\boldsymbol{r} - \omega t)}$$

where $\boldsymbol{E}_0$ is the amplitude and $\boldsymbol{q} = \omega/c$. Corresponding equation for the $\boldsymbol{B}$ field can also be derived from the Maxwell's equations and it has the same form as (A.5), with $\boldsymbol{E}$ substituted by $\boldsymbol{B}$.

The three vectors $\boldsymbol{E}$, $\boldsymbol{B}$ and $\boldsymbol{q}$ are perpendicular to each other, so if we say that the wave propagates along the z axis, the electric and magnetic fields will be oriented in the x and y directions, respectively (Fig. A.1).

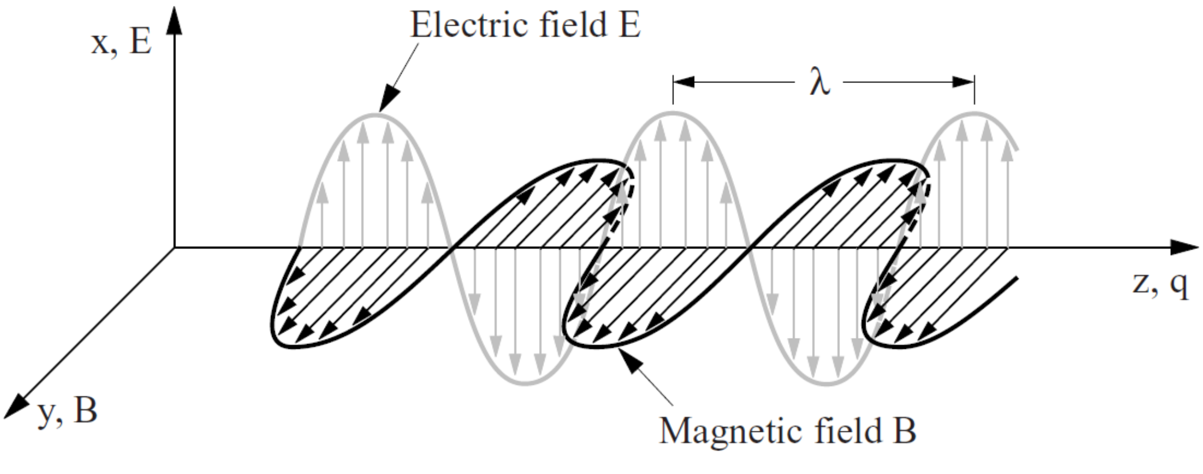

Figure A.1. Linearly polarized electromagnetic radiation of wavelength λ propagating along the z direction. Assuming that the electric field $\boldsymbol{E}$ is along the x direction, the magnetic field $\boldsymbol{B}$ points in the y direction and the wave vector $\boldsymbol{q}$ is directed along the z axis [Dressel2003].

A.2. Propagation of electromagnetic waves in a medium

Electric and magnetic fields will not be uniform within a material, but fluctuate from point to point reflecting the periodicity of the atomic lattice. For wavelengths appreciably larger than the atomic spacing we can nevertheless consider an average value of the electric and magnetic fields. These fields, however, are different compared to the fields in vacuum.

Maxwell's equations in the presence of matter are

$$\nabla \times \boldsymbol{E} + \frac{1}{c}\frac{\partial \boldsymbol{B}}{\partial t} = 0$$

$$\nabla \cdot \boldsymbol{D} = 4\pi\rho$$

$$\nabla \times \boldsymbol{H} - \frac{1}{c}\frac{\partial \boldsymbol{D}}{\partial t} = \frac{4\pi}{c}\boldsymbol{J}$$

$$\nabla \cdot \boldsymbol{B} = 0$$

where we have introduced the electric displacement $\boldsymbol{D}$ and the magnetic field strength $\boldsymbol{H}$ to account for the modifications by the medium. The current density $\boldsymbol{J}$ and the charge density ρ refer to the total quantities including both the external and induced currents and charge densities. They are position and time dependent as well. The electric displacement (or electric flux density) $\boldsymbol{D}$ is defined so that

$$\boldsymbol{D} = \varepsilon\boldsymbol{E} = \varepsilon_0\varepsilon_r\boldsymbol{E} = \varepsilon_0(1 + \chi_e)\boldsymbol{E} = \varepsilon_0\boldsymbol{E} + \boldsymbol{P}$$

where $\varepsilon = \varepsilon_1 + i\varepsilon_2$ is the complex dielectric function, $\varepsilon_0 = 8.8542 \times 10^{-12}\ \mathrm{AsV^{-1}m^{-1}}$ is the dielectric constant of vacuum, ε_r is the relative dielectric constant of the material, χ_e is the complex dielectric susceptibility and $\boldsymbol{P}$ is the dipole moment density or polarization density. The magnetic field strength $\boldsymbol{H}$ is defined so that

$$\boldsymbol{B} = \mu\boldsymbol{H} = \mu_0\mu_r\boldsymbol{H} = \mu_0(1 + \chi_m)\boldsymbol{H} = \mu_0(\boldsymbol{H} + \boldsymbol{M})$$

where $\mu = \mu_1 + i\mu_2$ is the complex permeability, $\mu_0 = 1.2566 \times 10^{-6}\ \mathrm{VsA^{-1}m^{-1}}$ is the permeability of vacuum, μ_r is the relative permeability of a material, χ_m is the complex magnetic susceptibility and $\boldsymbol{M}$ is the magnetic moment density or magnetization. Except in the case of ferromagnetism, the magnetic susceptibility χ_m is typically four to five orders of magnitude smaller than the dielectric susceptibility χ_e. For this reason, the diamagnetic and paramagnetic properties can generally be neglected compared to the dielectric properties when electromagnetic waves pass through a medium. In this case, we will assume $\mu_r \approx 1$.

By writing $\boldsymbol{D} = \varepsilon \boldsymbol{E}$, where $\varepsilon = \varepsilon_1 + i\varepsilon_2$ is the complex dielectric function, the change in magnitude and the phase shift between the displacement $\boldsymbol{D}$ and the electric field $\boldsymbol{E}$ are conveniently expressed. The notation accounts for the general fact that the response of the medium can have a time delay with respect to the applied perturbation.

If we assume that there is no external current, then the total current density $\boldsymbol{J}$ entering Maxwell's equation consists of a contribution arising from the motion of the conductive electrons in the presence of an electric field and a contribution arising from the redistribution of bound charges, $\boldsymbol{J} = \boldsymbol{J}_{cond} + \boldsymbol{J}_{bound}$. Ohm's law is assumed to apply to the conduction current

$$\boldsymbol{J}_{cond} = \sigma_1 \boldsymbol{E}$$

where σ_1 is the conductivity of the material. We can in most cases limit ourselves to the linear response so the conductivity does not depend on the electric field strength. Similarly to the dielectric function, conductivity can be assumed to be complex, $\sigma = \sigma_1 + i\sigma_2$, to include the phase shift of the conduction and the bound current. This leads to a more general Ohm's law

$$\boldsymbol{J} = \sigma \boldsymbol{E}$$

We define the relation between the complex conductivity and complex dielectric function as

$$\varepsilon = \varepsilon_0 + \frac{i}{\omega}\sigma \tag{A.6}$$

To find the wave equations in a medium, an infinite medium is considered to avoid boundary and edge effects. Furthermore, absence of external charges and currents is assumed. Electromagnetic waves are described by a sinusoidal periodic time and spatial dependence

$$\boldsymbol{E}(\boldsymbol{r}, t) = \boldsymbol{E}_0 e^{i(\boldsymbol{q}\cdot\boldsymbol{r} - \omega t)}$$

$$\boldsymbol{H}(\boldsymbol{r}, t) = \boldsymbol{H}_0 e^{i(\boldsymbol{q}\cdot\boldsymbol{r} - \omega t - \varphi)}$$

A phase factor φ is included to indicate that the electric and magnetic fields may be shifted in phase with respect to each other. The wave vector $\boldsymbol{q}$ has to be a complex quantity. To describe the spatial dependence of the wave it has to include propagation as well as an attenuation part.

Using Maxwell's equations, one can obtain wave equations for the electric and magnetic field [Dressel2003]

$$(\nabla^2 + \boldsymbol{q}^2)\boldsymbol{E} = 0$$
$$(\nabla^2 + \boldsymbol{q}^2)\boldsymbol{H} = 0$$

where Helmholtz's compact form of the wave equation is used. Here, the following dispersion relation between the wave vector $\boldsymbol{q}$ and the frequency ω is used

$$\boldsymbol{q} = \omega \left[\mu_0 \varepsilon_1 + \frac{i}{\omega}\mu_0 \sigma_1\right]^{1/2} \boldsymbol{n_q}$$

where we have assumed there is no external charge density, internal charge density is homogeneous and magnetic properties can be neglected ($\mu_r \approx 1$). $\boldsymbol{n_q} = \boldsymbol{q}/|\boldsymbol{q}|$ is the unit vector along the $\boldsymbol{q}$ direction. This complex wave vector $\boldsymbol{q}$ is a compact way of expressing the fact that a wave propagating in the $\boldsymbol{n_q}$ direction experiences a change in wavelength and an attenuation in the medium compared to when it is in free space.

A.3. Reflectivity

Let us consider the propagation of a plane electromagnetic wave from vacuum into a material. The surface of the material lies in the *xy* plane while the *z* axis is positive towards the bulk of the medium. The surface plane is described by the unit vector $\boldsymbol{n_s}$ normal to the surface. We further suppose that the direction of propagation is in the *xz* plane (plane of incidence). The incidence waves arrive at the surface at an angle ψ_i, which is the angle between the wave vector of the incident wave, $\boldsymbol{q_i}$, and $\boldsymbol{n_s}$ in the *xz* plane. One part of the electric and magnetic fields enters the material (i.e. is transmitted) at an angle ψ_t and the other part is reflected off the surface at an angle ψ_r.

Many measurements of the optical properties of solids involve the normal incidence reflectivity. In this special configuration ($\psi_i = \psi_t = \psi_r = 0$) the wave vector $\boldsymbol{q}$ is perpendicular to the surface while ***E*** and ***H*** point in the *x* and *y* directions, respectively. The complex reflection coefficient is given by

$$\hat{r} = \frac{E_{0r}}{E_{0i}} = |\hat{r}|e^{i\phi_r}$$

The phase shift ϕ_r is the difference between the phases of the reflected and the incident waves.

Normal incidence reflectivity can be expressed in terms of the complex dielectric function as [Dressel2003]

$$R = \left|\frac{E_{0r}}{E_{0i}}\right|^2 = \left|\frac{1 - \sqrt{\varepsilon}}{1 + \sqrt{\varepsilon}}\right|^2$$

A.4. Optical properties of metals

Optical transitions between electron states in the partially filled band (intraband transitions) together with transitions between different bands (interband transitions) are responsible for the electrodynamics. Here the focus will be on intraband excitations.

The Drude model regards metals as a classical gas of electrons executing a diffusive motion. The central assumption of the model is the existence of an average relaxation time τ which governs the relaxation of the system to equilibrium (i.e. the state with zero average momentum) after an external electrical field $\boldsymbol{E}$ is removed. Within the model, an expression for the dc conductivity (i.e. $\sigma(\omega = 0)$) can be obtained [Dressel2003]

$$\sigma_{dc} = \frac{ne^2\tau}{m} \tag{A.7}$$

where n is the charge density, while e and m are the charge and mass of a free electron. The complex, frequency dependent, conductivity is given by

$$\sigma(\omega) = \frac{\sigma_{dc}}{1 - i\omega\tau} = \sigma_{dc}\frac{1 + i\omega\tau}{1 + \omega^2\tau^2} \tag{A.8}$$

For reasons that will become apparent later, it is convenient to define the damping $\Gamma = \tau^{-1}$ and write this relation as

$$\sigma(\omega) = \frac{\sigma_{dc}\Gamma}{\Gamma - i\omega} = \sigma_{dc}\Gamma\frac{\Gamma + i\omega}{\Gamma^2 + \omega^2}$$

The plasma frequency of the conducting electrons is defined as [Dressel2003]

$$\omega_p = \sqrt{\frac{ne^2}{m\varepsilon_0}} = \sqrt{\frac{\sigma_{dc}\Gamma}{\varepsilon_0}} \tag{A.9}$$

Now, complex conductivity can be expressed as

$$\sigma(\omega) = \varepsilon_0\omega_p^2\frac{1}{\Gamma - i\omega} = \varepsilon_0\omega_p^2\frac{\Gamma + i\omega}{\Gamma^2 + \omega^2} \tag{A.10}$$

Using the general relation (A.6), the frequency dependence of the complex dielectric function is

$$\varepsilon(\omega) = \varepsilon_0 - \frac{\varepsilon_0 \omega_p^2}{\omega^2 + i\omega\Gamma} = \varepsilon_0 - \frac{\varepsilon_0 \omega_p^2}{\omega} \frac{1 - i\Gamma}{\omega^2 + \Gamma^2} \tag{A.11}$$

There is an average distance traveled by the electrons between collisions, called the mean free path ℓ. Within the framework of the Drude model, $\ell = \langle v \rangle_{th} \tau$, where $\langle v \rangle_{th}$ is the average thermal velocity of classical particles, at temperature T.

The picture is fundamentally different for electrons obeying quantum statistics, and the consequences of this have been developed by Sommerfeld. Within the framework of this model, the concept of the Fermi surface plays a central role. In the absence of an electric field, the Fermi sphere is centered around zero momentum. The Fermi sphere is displaced in the presence of an applied field $\boldsymbol{E}$, with the magnitude of the displacement given by $-eE\tau/\hbar$. The expression (A.8) is again recovered, but the scattering processes which establish the equilibrium in the presence of the electric field involve only electrons near to the Fermi surface. States deep within the Fermi sea are not influenced by the electric field. Consequently the expression for the mean free path is $\ell = v_F \tau$, with v_F the Fermi velocity, and differs dramatically from the mean free path given by the original Drude model. The difference has important consequences for the temperature dependencies. The underlying interaction with the lattice, the electron–electron and the electron–phonon interactions are also of importance and lead to corrections to the above description. Broadly speaking, these effects can be summarized assuming an effective mass which is different from the free-electron mass [Pines1966] and which is also frequency dependent.

The low frequency or Hagen–Rubens regime is defined by the condition $\omega\tau \ll 1$. In this regime the optical properties are mainly determined by the dc conductivity σ_{dc}. The real part of the conductivity σ_1 is frequency independent in this range, while the imaginary part increases linearly with frequency. The reflectivity R is in this regime given by

$$R(\omega) = 1 - \sqrt{\frac{8\varepsilon_0 \omega}{\sigma_{dc}}} \tag{A.12}$$

The practical importance of the Hagen-Rubens relation lies in the fact that optical measurements always cover just a finite range. For extraction of optical conductivity from measured reflectivity, Kramers-Kronig relations are used [Dressel2003, Kittel1996, Landau1960]. The Kramers-Kronig relations however need the reflectivity data in the frequency range $\omega \in [0, \infty]$. One can then simply use the Hagen-Rubens relation to extrapolate the low frequency reflectivity of metals. The high frequency region is usually extrapolated with a fast declining tail proportional to ω^{-2} or ω^{-4}. Above a certain frequency, with a sufficiently small value of the extrapolated tail, $R = 0$ is assumed.

Examples of optical conductivity curves for the Drude model are given in Figure A.2

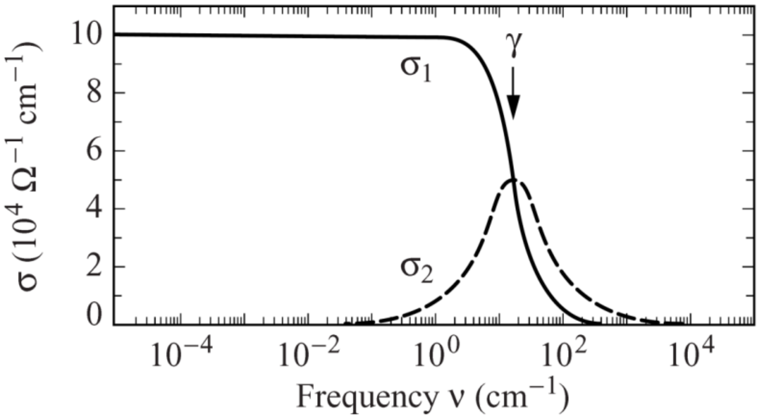

Figure A.2. Frequency dependent conductivity $\sigma(\omega)$ calculated after the Drude model (A.10) for the plasma frequency $\omega_p/(2\pi c) = \nu_p$ = 104 cm^{-1} and the scattering rate $1/(2\pi c\tau) = \gamma =$ 16.8 cm^{-1}. Well below the scattering rate γ, the real part of the conductivity σ_1 is frequency independent with a dc value σ_{dc} = 105 (Ωcm)$^{-1}$, above γ it falls off with ω^{-2}. The imaginary part $\sigma_2(\omega)$ peaks at γ where $\sigma_1 = \sigma_2 = \sigma_{dc}/2$; for low frequencies $\sigma_2(\omega) \propto \omega$, for high frequencies $\sigma_2(\omega) \propto \omega^{-1}$ [Dressel2003].

A.5. Optical properties of semiconductors

Here we will introduce the optical properties of band semiconductors and insulators. The central feature is the appearance of a single-particle gap, separating the valence band from the conduction band. The former is full and the latter is empty at zero temperature. The Fermi energy lies between these bands, leading to zero dc conduction at T = 0 K, and to a finite static dielectric constant. In contrast to metals, interband transitions from the valence band to the conduction band are of superior importance, and these excitations are responsible for the main features of the electrodynamic properties.

Interband transitions are described by the Lorentz model

$$\begin{aligned}\sigma(\omega) &= \frac{\varepsilon_0\omega_p^2\omega}{i(\omega_0^2-\omega^2)+\omega\Gamma} = \varepsilon_0\omega_p^2\omega\frac{\omega\Gamma - i(\omega_0^2-\omega^2)}{(\omega_0^2-\omega^2)^2+\omega^2\Gamma^2}\\ \varepsilon(\omega) &= \varepsilon_0 + \frac{\varepsilon_0\omega_p^2}{\omega_0^2-\omega^2-i\omega\Gamma} = \varepsilon_0 + \varepsilon_0\omega_p^2\frac{\omega_0^2-\omega^2+i\omega\Gamma}{(\omega_0^2-\omega^2)^2+\omega^2\Gamma^2}\end{aligned} \tag{A.13}$$

where ω_0 is the center frequency, often called the oscillator frequency, Γ denotes the broadening of the oscillator due to damping and $\omega_p = \sqrt{ne^2/\varepsilon_0 m}$ describes the oscillator strength, and is referred to as the plasma frequency in analogy to the free-electron case of metals. It is clear by comparing this expressions with equations (A.10) and (A.11) that the Drude model can be obtained from the Lorentz model by setting $\omega_0 = 0$.

Example of optical conductivity curves for Lorentz model are given in Figure A.3

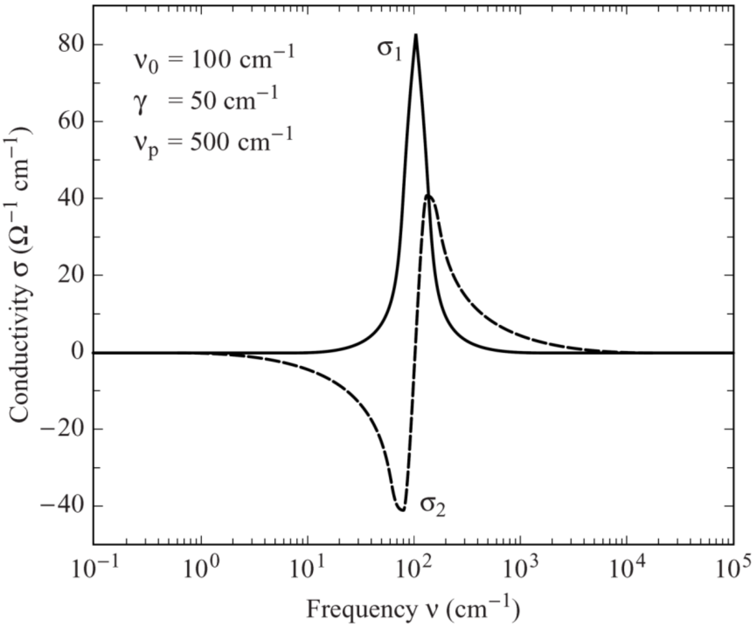

Figure A.3. Real and imaginary parts of the conductivity $\sigma(\omega)$ versus frequency calculated after the Lorentz model (A.13) for center frequency $\omega_0/(2\pi c) = \nu_0 = 100$ cm^{-1}, the width $1/(2\pi c\tau) = \gamma = 50$ cm^{-1} and the plasma frequency $\omega_p/(2\pi c) = \nu_p = 500$ cm^{-1} [Dressel2003].

A.6. Conventions and comparison to experiments

When the optical conductivity obtained through experiment is pictured, it is customary to put frequency ν in cm^{-1} (instead of the angular frequency ω in s^{-1}) on the x-axis of the plot and conductivity in (Ωcm)$^{-1}$ on the y-axis. The conversion of the angular frequency and the plasma frequency used in equations is done with $\omega = 2\pi c\nu$ and $\omega_p = 2\pi c\nu_p$, where c is the speed of light. It is then convenient to define the damping factor γ in cm^{-1} as $\Gamma = 2\pi c\gamma$ [Dressel2003]. The Drude-Lorentz model is now given by

$$\sigma(\nu) = \frac{\varepsilon_0 2\pi c\nu_p^2\nu}{i(\nu_0^2 - \nu^2) + \nu\gamma} = \varepsilon_0 2\pi c\omega_p^2\omega \frac{\omega\gamma - i(\omega_0^2 - \omega^2)}{(\omega_0^2 - \omega^2)^2 + \omega^2\gamma^2}$$

$$\varepsilon(\nu) = \varepsilon_0 + \frac{\varepsilon_0\nu_p^2}{\nu_0^2 - \nu^2 - i\nu\gamma} = \varepsilon_0 + \varepsilon_0\nu_p^2 \frac{\nu_0^2 - \nu^2 + i\nu\gamma}{(\nu_0^2 - \nu^2)^2 + \nu^2\gamma}$$

To further simplify the equations, it is good to look at how conductivity and dielectric function are related in SI system of units and in Gaussian (cgs) system of units. Conversion can be done using the relations

$$\sigma^{cgs}(\omega) = \frac{\sigma^{SI}(\omega)}{4\pi\varepsilon_0}$$

$$\varepsilon^{cgs}(\omega) = \frac{\varepsilon^{SI}(\omega)}{\varepsilon_0}$$

Usually, when converting optical conductivity we will use relation $1/4\pi\varepsilon_0 \approx 30c$ for simplicity. This relation gives a good value for the converted optical conductivity, but we must always have in mind that we have omitted writing units A^{-1}V (i.e. Ω) on the right-hand side to shorten it if we do dimensional analysis. Now the Drude-Lorentz model can be given by

$$\begin{aligned} \sigma(\nu) &= \frac{1}{60}\frac{\nu_p^2\nu}{i(\nu_0^2 - \nu^2) + \nu\gamma} = \frac{\nu_p^2\nu}{60}\frac{\nu\gamma - i(\nu_0^2 - \nu^2)}{(\nu_0^2 - \nu^2)^2 + \nu^2\gamma^2} \\ \varepsilon(\nu) &= \varepsilon_0 + \frac{\varepsilon_0\nu_p^2}{\nu_0^2 - \nu^2 - i\nu\gamma} = \varepsilon_0 + \varepsilon_0\nu_p^2 \frac{\nu_0^2 - \nu^2 + i\nu\gamma}{(\nu_0^2 - \nu^2)^2 + \nu^2\gamma} \end{aligned} \tag{A.14}$$

where frequency ν, plasma frequency ν_p and damping γ are in cm^{-1}. Optical conductivity σ is in (Ωcm)$^{-1}$ and ε and ε_0 are in AsV^{-1}cm^{-1} (i.e. (Ωcm)$^{-1}$s).

APPENDIX B

BRUGGEMAN

EFFECTIVE MEDIUM THEORY

B.1. Effective medium theory

The simplest way to calculate the optical response of a nano-composite material is by using either Maxwell-Garnett [Garnett1904, Carr1985] or Bruggeman [Bruggeman1935, Landauer1952, Carr1985] effective medium theory (EMT). Maxwell-Garnett EMT is implicitly oriented towards composites with a low volume fraction of the component to be studied. The theory does not give a percolation transition of the component in question even if we increase the volume fraction to the point where the component which was previously scarce now makes up the whole material. Obviously, this poses a problem if we are interested in a system near the percolation transition. In this case the Maxwell-Garnett EMT treatment will be inadequate.

Bruggeman EMT, however, treats all components symmetrically. It is in agreement with the Maxwell-Garnett EMT in the low-fraction limit, but it gives a percolation transition as the volume fraction of a component reaches a certain value. The following text is primarily based on [Carr1985].

Let us consider a two-component composite model of the Bruggeman EMT. One component of the nano-composite is metallic, with a dielectric function ε_M and volume fraction f. The other component is semiconducting, with a dielectric function ε_S and volume fraction $(1 - f)$. Bruggeman EMT treats all constituents of the composite in an equivalent way. Each grain of the composite is regarded as being embedded in a homogeneous effective medium. The effective medium is assumed to possess the optical properties of the composite as a whole. When placed in an external electric field, the grain in question will be polarized, with the electric field inside the grain given by [Carr1985]

$$\vec{E}_p = \frac{3\varepsilon_{eff}}{\varepsilon_p + 2\varepsilon_{eff}} \vec{E}_{eff} e^{-i\omega t}$$

where ε_p is the dielectric function of the grain, ε_{eff} is the effective dielectric function of the composite, $\vec{E}_{eff}$ is the effective field in the medium surrounding the grain, and we have assumed that the grain is spherical.

A self-consistency condition is used where the sum of the electric fields over all grains in the composite equals the effective field of the composite

$$\vec{E}_{eff} = f\vec{E}_M + (1-f)\vec{E}_S \tag{B.1}$$

Using two last expressions, one can obtain the quadratic equation for Bruggeman EMT

$$f\frac{\varepsilon_M - \varepsilon_{eff}}{\varepsilon_M + 2\varepsilon_{eff}} + (1-f)\frac{\varepsilon_S - \varepsilon_{eff}}{\varepsilon_S + 2\varepsilon_{eff}} = 0 \tag{B.2}$$

B.2. Non-spherical grains

More complex grain shapes can be approximated by ellipsoids. The field inside a single ellipsoidal grain in a uniform external field is then

$$\vec{E}_p = \sum_{j=1}^{3} \frac{\varepsilon_{eff}(\hat{x}_j \cdot \hat{e})\hat{x}_j}{g_j(\varepsilon_p)_j + (1-g_j)\varepsilon_{eff}} \vec{E}_{eff} e^{-i\omega t}$$

where we sum over the three principal axes of the ellipsoid, $(\varepsilon_p)_j$ is a component of the dielectric tensor of the ellipsoidal grain in the direction of one of the principal axes of the ellipsoid, and ε_{eff} is assumed isotropic. $\hat{x}_j$ are unit vectors in a coordinate system aligned with the ellipsoidal axes and $\hat{e}$ is a unit vector in the direction of the external electric field. g_j are the three depolarization factors of the ellipsoid [Landau1960, Kittel1996]. Depolarization factors relate the electric field inside the ellipsoid along a principal axis to the component of dipole moment per unit volume along that axis:

$$\left(\vec{E}_p\right)_j = -4\pi g_j \left(\vec{P}\right)_j$$

Depolarization factors are determined by the shape of the ellipsoid. If *a*, *b* and *c* are the half-lengths of the three principal axes of the ellipsoid, then the depolarization factor in the direction of the principal axis with the half-length *a* is

$$g_a = \frac{1}{2}\int_0^{\infty} \frac{abc}{\sqrt{(s+a^2)^3(s+b^2)(s+c^2)}} ds$$

Depolarization factors vary from nearly 0 (electric field along the length of a needle) to nearly 1 (electric field normal to the surface of a flat disc). For a sphere, depolarization factor is 1/3 in all three directions. The sum of the depolarization factors is always one

$$\sum_{j=1}^{3} g_j = 1$$

Previous equation for the field inside a single ellipsoidal grain can be simplified if we assume that the ellipsoids are not randomly oriented. If the principal axes of ellipsoids are oriented parallel to the applied external electric field, only a single term will remain so

$$\vec{E}_p = \frac{\varepsilon_{eff}}{g\varepsilon_p + (1-g)\varepsilon_{eff}} \vec{E}_{eff} e^{-i\omega t} \tag{B.3}$$

Notice that the same result is obtained if the external electric field is randomly oriented within a plane and the ellipsoid has an axis of rotation normal to the plane. This means that the ellipsoid is symmetrical within the plane so the depolarization factor is the same for both in-plane principal axes. Due to the symmetry, we can then always choose the orientation of the ellipsoid so that one of the in-plane principal axes is parallel to the external field.

Now we can again use the self-consistency condition for the sum of the electric fields over all grains (B.1) and, in combination with (B.3), obtain the quadratic equation for Bruggeman EMT

$$f\frac{\varepsilon_M - \varepsilon_{eff}}{g_M\varepsilon_M + (1-g_M)\varepsilon_{eff}} + (1-f)\frac{\varepsilon_S - \varepsilon_{eff}}{g_S\varepsilon_S + (1-g_S)\varepsilon_{eff}} = 0 \tag{B.4}$$

where g_M and g_S are the depolarization factors for the metallic and semiconducting grains, respectively. The change in the shape of the particles (i.e. the depolarization factor) affects the concentration at which percolation occurs within the Bruggeman EMT.

The two solutions of the EMT equation are

$$\varepsilon_{eff} = \frac{(p-f)\varepsilon_M + (p+f-1)\varepsilon_S}{2(p-1)} \pm \frac{\sqrt{-4p(p-1)\varepsilon_M\varepsilon_S + [(p-f)\varepsilon_M + (p+f-1)\varepsilon_S]^2}}{2(p-1)}$$

where $p = g_M + f(g_S - g_M)$. Physical solution is the one for which $Im(\varepsilon_{eff}) \geq 0$ [Carr1985].

For an arbitrary number of components in a composite, we can use the general equation

$$\sum_i f_i \frac{\varepsilon_i - \varepsilon_{eff}}{g_i \varepsilon_i + (1-g_i)\varepsilon_{eff}} = 0$$

where i is the index of the component of the composite. As we progress to a higher order equation, we will have more solutions which satisfy the equation above. Physical solution will again be the one for which $Im(\varepsilon_{eff}) \geq 0$.

B.3. The percolation condition

Here we are concerned with the percolation of the metallic grains. The simplest way to obtain the percolation condition is to notice that we get identical equations with dc conductivities instead of dielectric functions. The general form of the Bruggeman EMT equation for an arbitrary number of components is [Carr1985]

$$\sum_j f_j \frac{\varepsilon_j(\omega) - \varepsilon_{eff}(\omega)}{g_j \varepsilon_j(\omega) + (1-g_j)\varepsilon_{eff}(\omega)} = 0$$

Using relation (A.6), we obtain

$$\sum_j f_j \frac{\sigma_j(\omega) - \sigma_{eff}(\omega)}{g_j \sigma_j(\omega) + \left(1-g_j\right)\sigma_{eff}(\omega) - i\omega\varepsilon_0} = 0$$

If we limit ourselves to the metallic Drude conductivity in the dc limit ($\omega \to 0$) we get

$$\sum_j f_j \frac{\sigma_j - \sigma_{eff}}{g_j \sigma_j + \left(1-g_j\right)\sigma_{eff}} = 0$$

or, for our two components

$$f \frac{\sigma_M - \sigma_{eff}}{g_M \sigma_M + (1-g_M)\sigma_{eff}} + (1-f)\frac{\sigma_S - \sigma_{eff}}{g_S \sigma_S + (1-g_S)\sigma_{eff}} = 0$$

Here σ_M, σ_S and σ_{eff} are dc conductivities ($\sigma_{dc} = \sigma(\omega \to 0)$) of the metal component, semiconducting component and effective medium, respectively. We assume that the semiconducting component is not conductive at low frequencies (i.e. it does not contain a Drude contribution) so $\sigma_S = 0$ and the equation is simplified to

$$f\frac{\sigma_M-\sigma_{eff}}{g_M\sigma_M+(1-g_M)\sigma_{eff}}-\frac{1-f}{1-g_S}=0$$

Non-trivial solution to this equation is

$$\sigma_{eff}=\sigma_M+\sigma_M\frac{1-f}{g_M-1+f(g_S-g_M)}$$

We assume that $\sigma_M > 0$, so the percolation condition $\sigma_{eff} \geq 0$ yields

$$f \geq \frac{g_M}{g_M-g_S+1}$$

If the depolarization factors of metal and semiconducting grains are identical, $g_M = g_S \equiv g$ (e.i. they have the same shape), then this expression is reduced to the well-known percolation condition of the metallic component in a metal-insulator composite, $f \geq g$ [Stroud1998].

B.4. Metallic grains in vacuum

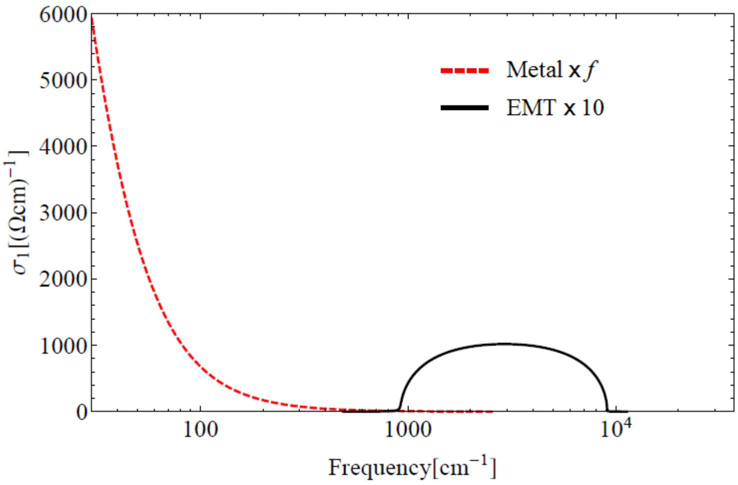

Figure B.1. Real part of the effective optical conductivity of the metal-vacuum composite model. Optical conductivity of the metal component (red dashed curve) is shown with its spectral weight in the composite (i.e. it is multiplied by f). The optical conductivity of the composite (black solid curve), calculated in the Bruggeman EMT, is multiplied by 10 for effect.

Let us consider the case of metallic spherical grains suspended in vacuum. Dielectric function of the vacuum is represented simply by $\varepsilon_0 = 8.8542 \times 10^{-12}\ \mathrm{AsV^{-1}m^{-1}}$, the dielectric constant of vacuum. Metallic component of the composite is modeled with a single Drude contribution by using equation (A.14) with the center frequency $\nu_0 = 0$ cm^{-1}. Plasma frequency of $\nu_p = 10\ 000$ cm^{-1} and damping of $\gamma = 16.8$ cm^{-1} are used as representative of a good metal [Dressel2003]. We have chosen the volume fraction of metal component to be $f = 0.25$ and the depolarization factor for spherical grains is 1/3. Using equations (B.2) and (A.6), we can calculate the optical conductivity of the effective medium (Fig. B.1).

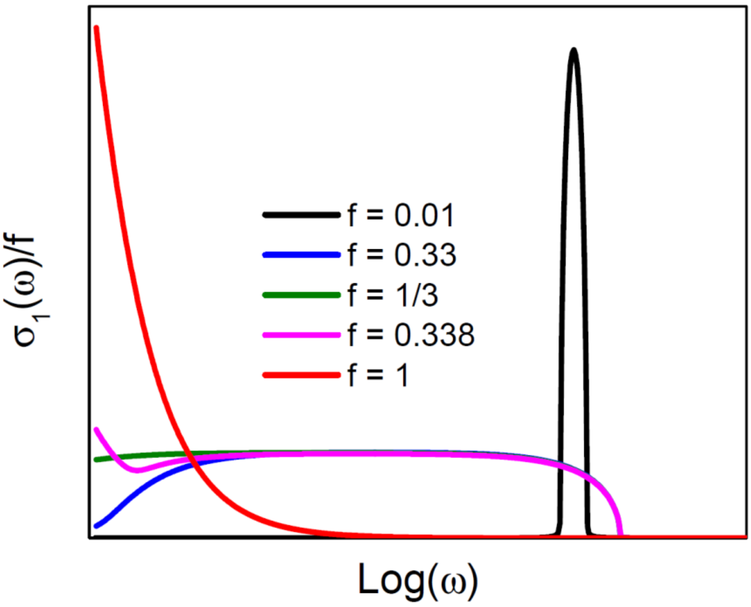

Figure B.2. Optical conductivity of the effective medium for a metal-vacuum composite with different volume fractions f of metal. The curves are normalized to their volume fractions for effect, with the exception of the curve with $f = 1$ which has been divided by 10. The choice of the normalizing factor is arbitrary and used solely to enable the comparison of curve shapes despite the difference in the magnitude of the curves.

EMT curve has one prominent feature, a peak explained within the theory as a localized surface plasmon on the metallic grains [Carr1985]. Figure B.2 shows the evolution of this peak within Bruggeman EMT when the volume fraction of the metallic grains is varied. With 1% metal, the composite shows a narrow peak near $\omega_p/\sqrt{3}$, the expected resonance frequency of the localized surface plasmon in the low metal volume fraction limit within the EMT

[Carr1985]. For the metal volume fraction $f = 1$ (i.e. full metal), we see a standard Drude optical conductivity curve of a bulk metal. Bruggeman EMT predicts percolation of spherical grains at $f = 1/3$. As the fraction of metal is increased from the low limit to the percolation threshold, the plasmon peak is widened and gains spectral weight (the normalization procedure selected for Fig. B.2 enables us to have a better overview of the curve shapes, but obscures the magnitudes at the first glance). At the percolation threshold, the low-frequency edge of the plasmon touches the zero frequency and then recedes to higher frequencies as the volume fraction is increased. At the same time, a quasi-Drude peak emerges at low frequencies which gains spectral weight with increasing volume fraction.

SAŽETAK

1. Uvod

Superstrukturiranje kristalne rešetke pojavljuje se kao impresivan pratilac nekim stanjima kondenzirane tvari. Superstrukturiranje slojevitih materijala pokazuje se posebno zanimljivo zbog niske dimenzionalnosti elektronskog spektra i više specijalnih elektronskih faza koje slojeviti materijali pokazuju već desetljećima [Wilson1969]. Slojeviti članovi obitelji dihalkogenida prijelaznih metala drže interes ovog rada. U toj obitelji materijala pojavilo se više zanimljivih tema poput metal-izolator prijelaza, teksturiranih faza elektronskih kondenzata i supravodljivosti. Dihalkogenidi prijelaznih metala imaju kemijsku formulu MX_2, gdje je M atom prijelaznog metala a X predstavlja halkogenidni atom. Svaki sloj ima kristalnu strukturu u X-M-X formi pri čemu se ravnina atoma prijelaznog metala nalazi između dviju ravnina halkogenidnih atoma. Atomi unutar slojeva su kovalentno povezani dok je veza među slojevima slaba i općenito se u literaturi predstavlja kao van der Waalsova.

Dihalkogenidi prijelaznih metala su posebno zapaženi kao prvi kvazi-dvodimenzionalni materijali koji su pokazali prijelaz vala gustoće naboja. U nekim slučajevima, smatralo se da se radi o prvim direktnim poopćenjima Peierlsovog mehanizma vala gustoće naboja koji je prethodno opažen u kvazi-jednodimenzionalnim spojevima. Drugi mehanizmi, poput Jahn-Teller efekta i ekscitonskog izolatora su također predloženi u slučajevima u kojima Peierlsov mehanizam nije bio utemeljen.

Ovaj rad proučava utjecaj superstrukturiranja na optička i transportna svojstva čistih i dopiranih uzoraka 1T-TaS_2 i 1T-$TiSe_2$. Ovi dihalkogenidi prijelaznih metala pokazuju kako jednostavna slojevita struktura može rezultirati kompleksnim preplitanjem raznih elektronskih faza. Ovaj doktorski rad ima 7 poglavlja. Prvo poglavlje daje uvod u područje dihalkogenida prijelaznih metala i kratak uvod u potrebne teorijski modele. Ukoliko je procijenjeno kao nužno za razumijevanje rezultata rada, šira teorijska pozadina stavljena je u dodatke. Drugo poglavlje daje pregled upotrijebljenih eksperimentalnih metoda. Treće poglavlje predstavlja pregled dosadašnjeg rada na čistom i dopiranom 1T-TaS_2. Ovdje su također prezentirani rezultati mjerenja uz osnovnu analizu. Četvrto poglavlje uvodi posljedice nanoteksturiranosti približno sumjerljive faze vala gustoće naboja u 1T-TaS2 i potrebu za korištenjem teorije efektivnog medija. Peto poglavlje se bavi posljedicama superstrukturiranjem uzrokovanog preslagivanja fononskih disperzija na optički spektar. Predstavljena je nova procedura za dobivanje informacija o preraspodjeli naboja uslijed superstrukturiranja. Šesto poglavlje predstavlja prijašnji rad na 1T-TiSe$_2$ kao i nove rezultate. Pokazuje se da je model dviju vodljivih vrpci dovoljan za objašnjenje mjerenih optičkih spektara. Dodatak A daje uvod u optička svojstva materijala bitna za ovaj rad. Dodatak B daje uvod u Bruggemanovu teoriju efektivnog medija.

2. Eksperimentalne metode

U radu su prezentirana optička mjerenja reflektivnosti na čistim i dopiranim uzorcima 1T-TaS$_2$ i 1T-TiSe$_2$ u rasponu frekvencija od 30 cm^{-1} do 37000 cm^{-1}. Sva optička mjerenja napravljena su u grupi prof. dr. Martina Dressela na 1. Physikalisches Institut Sveučilišta u Stuttgartu, u Njemačkoj. Mjerenja električne otpornosti napravljena su na istim uzorcima u grupi dr. sc. Ane Smontare u Laboratoriju za fiziku transportnih svojstava, Instituta za fiziku u Zagrebu, u Hrvatskoj.

Ako je valna duljina upadnog elektromagnetskog zračenja puno manja od dimenzija uzorka, vrijede pravila geometrijske optike, a difrakcijski i rubni efekti su od manjeg značaja. Standardna mjerenja refleksije se izvode u iznimno širokom frekvencijskom području, od milimetarskih valova do ultraljubičastog područja (između 1 cm^{-1} i 10^6 cm^{-1}). Iako su monokromatski izvori s prilagodljivom frekvencijom dostupni u infracrvenom, vidljivom i ultraljubičastom području, standardno se koriste širokopojasni izvori nekoherentnog zračenja, a željena frekvencija se onda odabire pomoću posebnih optičkih elemenata. Pošto se mjerenja izvode u konačnom rasponu frekvencija, potrebno je ekstrapolirati na osnovu postojećih podataka do $\omega = 0$ i $\omega = \infty$. Kod metala se niskofrekventni dio spektra ekstrapolira pomoću Hagen-Rubens jednadžbe (vidi Prilog A, jedn. (A.12)), dok se kod poluvodiča niskofrekventni dio ekstrapolira kao konstanta čiji je iznos jednak reflektivnosti na najnižoj mjerenoj frekvenciji. U oba slučaja visokofrekventni dio se iznad ultraljubičastog područja ekstrapolira pomoću ω^{-2} ili ω^{-4} frekvencijske ovisnosti. Ova procedura nam zatim omogućava da pomoću Kramers-Kronig analize [Dressel2003, Kittel1996, Landau1960] dobijemo i realni i imaginarni dio kompleksne vodljivosti.

Prilikom mjerenja infracrvenog frekvencijskog područja, korištena je infracrvena spektroskopija pomoću Fourierovog transformata (*engl.* Fourier Transform Infrared Spectroscopy - FTIR). FTIR spektroskopija koristi osnovni princip Michelsonovog interferometra (vidi sliku 2.1), gdje se zraka iz izvora na polupropusnom zrcalu dijeli na dvije zrake – jednu koja se reflektira na fiksnom zrcalu na udaljenosti L od polupropusnog zrcala i drugu koja se reflektira na pomičnom zrcalu koje oscilira oko udaljenosti L za vrijednost x. Obje zrake se vraćaju na polupropusno zrcalo, rekombiniraju se i tvore interferogram (vidi sliku 2.2, lijevo) zbog razlike optičkih puteva zraka $2x$. Interferogram se pomoću Fourierovog transformata može pretvoriti u frekvencijski ovisan spektar (slika 2.2, desno). Ova procedura se uobičajeno radi pomoću specijaliziranih programskih paketa kakav je i Opus, programski paket standardno isporučen s Bruker FTIR uređajima i korišten u ovom radu. Nakon rekombinacije na polupropusnom zrcalu, zraka napušta interferometer, reflektira se na uzorku ili zrcalu i dolazi na detektor. Prilikom refleksije na uzorku, svjetlost će na nekim valnim duljinama biti više ili manje apsorbirana što se može vidjeti tako da se konačni frekvencijski ovisan spektar uzorka podijeli sa spektrom upadne zrake.

Mjerenja u sklopu ovog rada su koristila tri FTIR spektrometra: Bruker IFS 66v/S, Bruker Vertex 80v i Bruker IFS 113v. Mjerenja su se vršila u temperaturnom području od 10 K do 290 K, pri čemu su korišteni kriostati opremljeni KBr prozorima. Bruker IFS 66v/S i Bruker Vertex 80v korišteni su u srednjem infracrvenom (*engl.* mid-infrared - MIR) frekventnom području od 500 cm^{-1} do 8000 cm^{-1} uz rezoluciju od 1 cm^{-1}. Iznimka su mjerenja na dopiranom 1T-TaS$_2$ uzorku (d-TaS$_2$), gdje je korištena rezolucija 0.5 cm^{-1}. Za mjerenja u MIR području, spektroskopi su bili opremljeni s HYPERION IR mikroskopom. Bruker IFS 113v spektrometar korišten je za mjerenja u frekvencijskom rasponu od 10 cm^{-1} do 800 cm^{-1} uz rezoluciju od 0.24 cm^{-1}. Spektrometar je bio opremljen posebnim kriostatom koji je omogućavao *in-situ* naparavanje zlata na uzorak. Pomoću referentnih mjerenja na pozlaćenom uzorku značajno je podignuta kvaliteta mjerenja.

Kako bi se što više povećao mjereni frekvencijski raspon, u suradnji s Mathiasom Eichlerom iz grupe prof. dr. Martina Dressela na 1. Physikalisches Institut Sveučilišta u Stuttgartu, napravljena su elipsometrijska mjerenja kojima se mjereni raspon povisio na 37000 cm^{-1}. Pri mjerenju se na uzorku reflektira linearno polarizirana svjetlost čija se polarizacija mijenja u eliptičnu uslijed interakcije s površinom uzorka. Upotrebom Fourierove analize amplitude i faze detektiranog signala, mogu se izračunati elipsometrijski kutevi Ψ and Δ. U jednostavnom slučaju gdje se razmatra samo granica zraka uzorka, reflektivnost i optička vodljivost mogu se izračunati direktno iz elipsometrijskih kuteva [Dressel2003]. U ovom radu korišten je Woolam VASE (Variable Angle Spectroscopic Ellipsometer) elipsometar.

Električna vodljivost mjerena je u suradnji s dr. sc. Petrom Popčevićem, u grupi dr. sc. Ane Smontare u Laboratoriju za fiziku transportnih svojstava Instituta za fiziku u Zagrebu, u Hrvatskoj. Korištena je standardna metoda četiri kontakta.

Uzorke je sintetizirao dr. Helmuth Berger sa École polytechnique fédérale de Lausanne (EPFL), dok je njihovo korištenje za ovo istraživanje omogućio prof. dr. László Forró, Laboratoire de Physique de la Matière Complexe u EPFL-u. Korišteni su čisti i dopirani monokristalni uzorci 1T-TaS_2 i 1T-$TiSe_2$. Dopirani uzorak 1T-TaS_2 (d-TaS_2) pripada istoj seriji kao i uzorak čija su svojstva opisana u referenci [Xu2010]. d-TaS_2 je dopiran s manje od 0.1% bakra. Dopirani uzorak 1T-$TiSe_2$ je 1T-$TiSe_{2-x}Te_x$, gdje je $x = 0.03$.

3. Superstrukturiranje 1T-TaS_2

1T-TaS_2 je slojeviti materijal s jakom kovalentnom vezom unutar sloja i, prema literaturi, slabim van der Waals vezama među slojevima (slika 3.1). Dugo je poznato da ovaj materijal ima pet stabilnih faza koje ovise o temperaturi, pri čemu četiri faze podržavaju valove gustoće naboja (*engl*. Charge Density Waves - CDW) [Wilson1975, Scruby1975, Bayliss1984, Thomson1994]. Nedavno je otkrivena i šesta stabilna faza koja je dostupna samo ako se material izloži femtosekundnim laserskim pulsevima na niskim temperaturama [Stojchevska2014]. Nedeformirana faza 1T-TaS_2, koja se pojavljuje iznad 543 K [Bayliss1983], ima jako jednostavnu strukturu. U svakom sloju, heksagonalna dvodimenzionalna rešetka tantalovih atoma nalazi se u sendviču između dviju istih takvih ravnina sumporovih atoma, na način da se svaki Ta atom nalazi u oktahedralnoj konfiguraciji između šest S atoma. Konstante rešetke u nedeformiranoj fazi su $a = b = 3.36$ Å u ravnini i $c = 5.90$ Å okomito na ravninu [Jellinek1962]. Nedeformirana faza je metalična pošto svaki Ta atom ima po jedan elektron u polupopunjenoj 5*d* vrpci [Rossnagel2006]. Na niskoj temperaturi materijal je u fazi sumjerljivog vala gustoće naboja (*engl*. Commensurate CDW - CCDW) s periodičkom deformacijom kristalne rešetke u obliku Davidove zvijezde [Wilson1975, Thomson1988] (slika 3.1, c). Svaka Davidova zvijezda sastoji se od 13 Ta atoma, pri čemu imamo jedan centralni atom i po šest atoma u dva koncentrična prstena oko središnjeg. Zvijezde se nalaze u superstrukturi s $\sqrt{13}a \times \sqrt{13}a$ rotiranom jediničnom ćelijom u odnosu na jediničnu ćeliju nedeformiranog materijala. Gustoća stanja deformiranog materijala ima procijep, pri čemu samo 12 elektrona iz polupopunjenih Ta vrpci stane ispod procijepa. Preostali, trinaesti elektron ostaje iznad procijepa, u polupopunjenoj podvrpci na Fermijevom nivou [Rossnagel2006]. Ovo omogućava Mottovu lokalizaciju u dvije dimenzije [Fazekas1979, Fazekas1980] koju potvrđuju spektroskopska mjerenja [Pillo2000, Zwick1998], kao i STM (skenirajuća tunelirajuća mikroskopija) mjerenja [Kim1994]. Mjerenja pokazuju da je Mottov procijep reda veličine 0.1 eV [Gasparov2002, Pillo2001, Manzke1989, Dardel1992], što se slaže i s DFT (engl. Density Functional Theory) proračunima [Freericks2009]. Mottova faza u 1T-TaS$_2$ jedinstvena je po tome što je to jedini poznati dihalkogenid prijelaznog metala u kojem je nađena. Na sobnoj temperaturi materijal je u miješanoj fazi približno sumjerljivog vala gustoće naboja (*engl.* nearly commensurate CDW - NCCDW) (slika 3.1 d). NCCDW superstruktura izgleda kao superstruktura koja upotrebljava zvjezdastu superstrukturu CCDW faze kako bi se napravila tekstura koja se sastoji od približno heksagonalnih CCDW domena i približno trokutastih nedeformiranih područja između CDW domena [Wilson1975, Wu1989, Thomson1994, Spijkerman1997]. Ta tekstura izgledom podsjeća na kagome rešetku. Trinaesti elektron koji se na niskim temperaturama lokalizirao, ovdje nalazi energetski povoljnijim prijeći iz CCDW domena u nedeformirane trokute. Slijedom toga, možemo govoriti o teksturi poluvodičkih heksagona i metaličnih trokuta [Thomson1994, Spijkerman1997]. Osim ovih faza, system još može biti u fazi nesumjerljivog vala gustoće naboja (*engl.* incommensurate CDW - ICCDW), "prugastoj" (*engl.* striped) fazi i prije spomenutoj fotoinduciranoj fazi (za više informacija o ovim fazama pogledati [Wilson1975, Scruby1975, Bayliss1984, Thomson1994, Stojchevska2014]). U ovom radu će se istraživati CCDW/Mott i NCCDW faza 1T-TaS$_2$.

Električna otpornost 1T-TaS$_2$ (slika 3.3), pokazuje nemetalno ponašanje u NCCDW fazi, jak porast otpornosti u CCDW/Mott fazi i fazni prijelaz prvog reda sa širokom histerezom između. Nemetalno ponašanje u NCCDW fazi objašnjeno je kao posljedica nano-teksture poluvodičkih heksagona i metaličnih trokuta u kagome-nalik rasporedu [Sipos2008, Spijkerman1997]. Smatra se da pri tome uski kanali koji povezuju metalična područja najviše doprinose raspršenju vodljivih elektrona u mjerenju električne otpornosti. Poluvodičke domene se povećavaju ako se temperature spušta [Thomson1994] pri čemu se ne mijenja omjer površina poluvodičkih i metalnih domena [Ritschel2013]. To znači da se metalične domene zapravo povećavaju zajedno sa poluvodičkim domenama kako se temperatura spušta.

Istovremeno, kako poluvodičke domene postaju sve pravilnije heksagonalne, tako sve više “stišću”, tj. sužuju kanale koji povezuju vodljiva područja pri čemu se povećava raspršenje vodljivih elektrona.

Optička svojstva i fononski modovi 1T-TaS_2 proučavani su u širokom rasponu temperatura i frekvencija [Benda1974, Beal1975, Barker1975, Bayliss1983, Gorshunov1986, Karecki1979, Uchida1981, Gasparov2002]. Slika 3.4 prikazuje reflektivnost mjerenu za ovaj rad na čistom 1T-TaS_2 u CCDW/Mott i NCCDW fazi. Slika 3.5 prikazuje optičku vodljivost dobivenu iz mjerene reflektivnosti pomoću Kramers-Kronig analize. Krivulje pokazuju jasno razdvajanje NCCDW i CCDW/Mott faze. Porast reflektivnosti s porastom temperature u NCCDW fazi je u skladu s nemetalnim ponašanjem električne otpornosti, ali je u suprotnosti s visokim iznosom reflektivnosti i metaličnim oblikom krivulje u niskofrekventnom području. Ovaj prividni paradoks samo je jedan od tragova koji vode na efektivno nano-kompozitnu prirodu elekktronskog odziva u 1T-TaS_2. Između 50 i 400 cm^{-1} nalaze se dvije jasno odvojene grupe fononskih modova. Jednostavna analiza u okviru modela mase na opruzi govori nam da je fononska grupa niža u frekvenciji povezana s težim atomima (Ta), a fononska grupa viša u frekvenciji povezana s lakšim atomima (S). Fononski modovi su prisutni i u CCDW i NCCDW fazi, pri čemu su modovi u NCCDW fazi puno širi i zasjenjeni, dok su modovi u CCDW fazi oštri i moguće je razlučiti više vrhova.

Poznato je da tlak jako utječe na svojstva 1T-TaS_2. CCDW/Mott prijelaz će biti potpuno potisnut u korist NCCDW faze upotrebom tlaka oko 1 GPa, pri čemu materijal postaje supravodljiv. Daljnjim povećavanjem tlaka potiskuju se sve ostale CDW faze sve dok materijal ne bude u nedeformiranoj metaličnoj fazi iznad 8 GPa [Sipos2008]. Značajni uvid reference [Sipos2008] je da jednom kad se supravodljiva faza potpuno ostvari u NCCDW fazi, temperatura supravodljivog prijelaza ostaje konstantna oko 5 K bez obzira na povećanje tlaka, pa čak bez obzira i na nestanak NCCDW faze u kojoj supravodljivost i nastaje. Ova neosjetljivost supravodljivosti na nestanak faze u kojoj nastaje (i svih ostalih CDW faza) govori da su domene u kojima supravodjivost nastaje jako slične nedeformiranoj metaličnoj fazi. Dakle, supravodljivost nastaje u metaličnim trokutastim domenama u NCCDW fazi, a metalična faza iz reference [Sipos2008] predstavlja njihovu dobru aproksimaciju.

Usprkos tome što nisu direktno zamjenjivi, dopiranje se često koristi kao kemijski analogon tlaku. 1T-TaS_2 je detaljno proučen upotrebom dopiranja [Thomson1972, Wu1988, Tison2004, Benda1974, DiSalvo1975, Endo2000, Ang2013, DiSalvo1976A, Ko2011, Ang2012, Pettenkofer1994, Pettenkofer1991, Xu2010, Lahoud2014]. Značajno za ovaj rad, pokazano je da lagano dopiranje s manje od 0.1% bakra u potpunosti potiskuje CCDW/Mott fazu i omogućuje istraživanje NCCDW faze do najnižih temperatura [Xu2010] (Fig. 3.7). Naš uzorak dopiranog 1T-TaS_2 pripada istoj seriji kao i uzorak čija su svojstva istraživana u referenci [Xu2010], te ga označavamo d-TaS_2 kao u [Xu2010]. Naša optička mjerenja pokazuju da materijal zaista ostaje u NCCDW fazi do najniže mjerene temperature od 23 K (slike 3.8, 3.9). Slika 3.10 prikazuje slaganje temperaturno ovisnih optičkih vodljivosti za $\omega \rightarrow 0$ s dc vrijednostima.

4. Nano-kompozitno superstrukturiranje u 1T-TaS_2

Rendgenska i STM mjerenja utvrdila su da 1T-TaS_2 efektivno odgovara nano-kompozitu [Spijkerman1997, Thomson1994]. Sumjerljive poluvodičke domene su približno heksagoni dimenzije 7 nm. Poluvodičke i metalične domene zajedno tvore kagome rešetku što nam omogućuje da procijenimo volumni udio poluvodičke komponente na ¾ i volumni udio metalične komponente na ¼. Optički odziv kompozita sa zrnima nanometarske veličine će biti drugačiji od odziva homogenog uzorka. Najjednostavniji način modeliranja optičkog odziva nano-kompozita je pomoću teorije efektivnog medija (*engl.* Effective Medium Theory - EMT), pri čemu smo mi odabrali Bruggemanovu teoriju [Bruggeman1935, Landauer1952, Carr1985] zbog simetričnog tretmana zrna raznih vrsta.

U sklopu ovog rada upotrijebljen je trokomponentni Bruggemanov EMT model NCCDW faze 1T-TaS_2. Model se dobro slaže s mjerenim refleksijskim krivuljama i optičkim vodljivostima dobivenima na temelju Kramers-Kronig analize (slike 4.10, 4.11). Tri komponente koje čine kompozitni model su metalna zrna, konekcije među metalnim zrnima i poluvodička zrna. Metalna zrna simuliraju metalične trokutiće u NCCDW fazi, a njihova optička vodljivost dobivena je na temelju frekvencije plazme dobivene iz DFT računa napravljenih u suradnji s prof. dr. Ivom Batistićem i raspršenja u metalnoj fazi dobivenog iz mjerenja električne otpornosti pod tlakom iz reference [Sipos2008] (slika 4.4). Konekcije među metaličnim trokutićima su simulirane zrnima koja imaju frekvenciju plazme jednaku onoj metalnih zrna, ali puno veće raspršenje (slika 4.8). Sumjerljivi heksagoni u NCCDW fazi su simulirani poluvodičkim zrnima čiji se optički odziv sastoji od serije Lorentzijana čiji su parametri prilagođavani eksperimentalnim podacima (slika 4.9). U radu je pokazano da Bruggemanov trokomponentni EMT model uspješno slijedi eksperimentalne krivulje (slike 4.10, 4.11). Ovime su riješena dva problema modeliranja optičkih svojstava NCCDW faze u homogenom Drude-Lorentz modelu: nedostajuća spektralna težina na niskim frekvencijama koja pripada metaličnim trokutićima i višak spektralne težine ispod međuvrpčanih pobuđenja. U radu je pokazano da je spektralna težina niskofrekventnog odziva metaličnih trokutića u skladu s DFT računima i zapravo puno veća nego što bi se moglo zaključiti iz homogenog modela eksperimentalnih krivulja. Višak spektralne težine ispod međuvrpčanih pobuđenja je prenisko u frekvenciji da bi se objasnio kao dio međuvrpčanih pobuđenja, a istovremeno ima preveliku širinu i spektralnu težinu za fononski mod. U radu je pokazano da ta dodatna spektralna težina pripada lokaliziranom površinskom plazmonu na površini metaličnih domena, a koji se pojavljuje prilikom EMT miješanja komponenti modela kao direktna posljedica nano-teksturiranosti NCCDW faze u 1T-TaS$_2$.

5. Preraspodjela naboja preko superstrukture

Superstrukturiranje ima izniman utjecaj na optička svojstva 1T-TaS$_2$, kako u NCCDW tako i u CCDW fazi. Superstrukturiranje uzrokuje smanjenje jedinične rešetke u recipročnom prostoru i preslagivanje originalne nedeformirane prve Billouinove zone u manju deformiranu zonu. Prilikom toga, akustičke fononske grane se također preslaguju što dovodi do novih optičkih modova na konačnim frekvencijama. Merđutim, samo preslagivanje nije dovoljno da bi potencijalni optički mod bio aktivan. Nužan (i dovoljan) uvjet za aktivan optički mod je postojanje dipola, tj. preraspodjela naboja (slika 5.2). Dodatna deformacija rešetke, prisutna u realnom materijalu, zatim dovodi do cijepanja vrhova, ali ne može promijeniti ukupnu spektralnu težinu originalnog moda.

Nova analiza fononskih modova prikazana u ovom radu omogućuje određivanje preraspodjele naboja preko superstrukture u CCDW fazi. Pošto se NCCDW faza sastoji od nedeformiranih poručja i CCDW domena, analiza se može primjeniti i na NCCDW fazu. Na temelju te analize, nalazimo da se prilikom superstrukturiranja sav naboj preraspodjeljuje između vanjskog prstena zvjezdaste deformacije i centra. Unutrašnji prsten ostaje pri tome nedirnut (do na grešku procedure).

U ovoj analizi korištena je pretpostavka temeljena na DFT računima da Ta orbitale dominiraju Fermijevim nivoem. Ova pretpostavka zauzvrat omogućava da kovalentne veze između atoma unutar sloja aproksimiramo efektivno „ionskom“ vezom. Pri tome pretpostavljamo da se elektronski oblaci oko Ta atoma drže svojih atoma. Ova procedura daje dobre rezultate u NCCDW fazi, međutim u CCDW/Mott fazi nailazimo na probleme. Omjer spektralnih težina fononskih modova u CCDW/Mott fazi više nije A:B:B:A. To znači da ne možemo u tom slučaju upotrijebiti istu analizu jer A:B:B:A uzorak izvire iz pretpostavke efektivne „ioničnosti“ atoma. Promjene u omjeru spektralnih težina fononskih modova ukazuju na miješanje Ta i S orbitala na Fermi nivou.

6. Superstrukturiranje 1T-TiSe$_2$

1T-TiSe$_2$ ima strukturu identičnu onoj 1T-TaS$_2$, pri čemu na mjestu atoma tantala stoje atomi titana, a na mjestu atoma sumpora stoje atomi selena. Međutim, ta dva materijala pokazuju veliku razliku u fizikalnim svojstvima. 1T-TiSe$_2$ se na sobnoj temperaturi nalazi u normalnoj fazi i tek spuštanjem temperature ispod 200 K ulazi u fazu sumjerljivog vala gustoće naboja [DiSalvo1976B]. Materijal ne pokazuje histerezu u fizikalnim svojstvima pri podizanju temperature iznad 200 K. U normalnoj fazi materijal ima heksagonalnu strukturu s konstantama rešetke a = 3.535 Å (unutar slojeva) i c = 6.004 Å (okomito na slojeve) [DiSalvo1976B, Greenaway1965] (Slika 6.1). Se ravnine se nalaze 0.25c ispod i iznad Ti ravnine. Pri niskim temperaturama (77 K), pomak Ti atoma uslijed vala gustoće naboja je oko 0.085 Å, a omjer pomaka atoma Ti naspram Se je približno 3:1. Svi pomaci su paralelni slojevima [DiSalvo1976B].

Računi pokazuju da u elektronskoj strukturi blizu Fermijevog nivoa postoje dvije vrpce: šupljinska Se 4p valentna vrpca s maksimumom na Γ točki i elektronska Ti 3d vodljiva vrpca s minimum na L točki prve Brillouinove zone [Leventi-Peetz1995, Zhu2014] (Slika 6.3). Ti elektronski i šupljinski džepovi mogu se vidjeti i u ARPES mjerenjima (Slika 6.4).

Priroda vala gustoće naboja u 1T-TiSe$_2$ još nije definitivno određena. Neki autori zagovaraju ideju tradicionalnog Peierlsovog mehanizma [Rossnagel2011], no to nije vjerojatno zbog oblika Fermijeve plohe 1T-TiSe$_2$. Najvjerojatniji mehanizmi za objašnjenje vala gustoće naboja u ovom materijalu su ekscitoni [May2011] i Jahn-Teller efekt [Kidd2002]. Mi nemamo način razlučiti između ova dva scenarija na osnovu optičkih mjerenja. Umjesto toga, usredotočiti ćemo se na normalnu fazu pošto se tamo stvaraju uvjeti za nastanak vala gustoće naboja. Relativna važnost elektron-elektron i elektron-fonon interakcija je još uvijek predmet rasprave [VanWezel2010, Monney2011, Hellmann2012, Castellan2013, Weber2011].

Čak ni naoko lagano pitanje da li je materijal polumetal (*engl.* “semimetal”) ili poluvodič još nema konačan odgovor. Reference [Li2007, Anderson1985] kažu da se radi o polumetalu s indirektnim preklopom vrpci od 120 meV [Rohwer2011, Cercellier2007]. Reference [Rasch2008, Kidd2002] kažu da se radi o poluvodiču s indirektnim procijepom od 150 meV.

Električna otpornost unutar slojeva prikazana je na slici 6.5. Otpornost pokazuje maksimum blizu 165 K povezan sa superstrukturiranjem [DiSalvo1976B, DiSalvo1978, Benda1974]. Slika 6.5 također pokazuje Hall koeficijent za struju paralelnu slojevima i magnetsko polje okomito na slojeve. Iznad temperature prijelaza Hall koeficijent R_H je pozitivan što unutar pretpostavke postojanja šupljinske i elektronske vrpce znači da šupljinska mobilnost dominira.

Mjerena reflektivnost i izračunata optička vodljivost u normalnoj fazi prikazane su na slici 6.7, zajedno s prilagodbom na eksperimentalne podatke. U literaturi je uobičajeno kod 1T-TiSe$_2$ raditi prilagodbu na eksperimentalne podatke pomoću jednog Drude doprinosa [Li2007]. Elektronska struktura materijala upućuje na fizikalnu podlogu za promjenu modela. Naime, pošto su i elektronska i šupljinska vrpca prisutne na Fermijevom nivou, očekivali bismo da obje doprinose niskofrekvrentnoj optičkoj vodljivosti. Drugim riječima, potrebno je koristiti model koji uzima u obzir dvije vrpce koje se modeliraju s dva Drude doprinosa. Naša analiza u okviru modela dvije vrpce daje procjenu omjera efektivnih masa nosioca naboja, što nam omogućuje da usporedbom s ARPES mjerenjima [Kidd2002] identificiramo nosioce naboja u svakoj vrpci. Spektralna težina i gušenje u elektronskoj i šupljinskoj vrpci prikazani su na slici 6.9. Iz poznate spektralne težine vrpce može se direktno izračunati širina vrpce ukoliko je vrpca dvodimenzionalnog karaktera (jednadžba (6.7)). Elektronska vrpca je trodimenzionalnog karaktera pa taj izraz ne možemo primijeniti na nju. Međutim, šupljinska vrpca je dvodimenzionalna i račun na 290 K pokazuje da je širina vrpce 52 meV. Ekvivalentna temperatura računata preko izraza $E = k_B T$ je 608 K. Ovo se oštro protivi poluvodičkoj slici materijala jer naša mjerenja pokazuju da bi za termalnu populaciju vrpci bila potrebna temperatura veća od 608 K (jer tu još treba dodati i širinu procijepa i širinu elektronske vrpce), dok je mjerenje rađeno na 290 K. Stoga zaključujemo da je 1T-TiSe$_2$ u normalnoj fazi polumetal s indirektnim preklopom elektronske i šupljinske vrpce.

U ovom poglavlju predstavljeni su i rezultati mjerenja u CDW fazi čistog materijala, kao i mjerenja u obje faze materijala u kojem je 1.5% atoma Se zamijenjeno atomima Te. Analiza ovih mjerenja u svjetlu nalaza ovog rada je u tijeku i predstavlja smjer u kojem se ovdje započeti rad može nastaviti razvijati.

Bibliography

[Anderson1985] O. Anderson *et al.*, Phys. Rev. Lett. 55, 2188 (1985).

[Ang2012] R. Ang *et al.*, Phys. Rev. Lett. 109, 176403 (2012).

[Ang2013] R. Ang *et al.*, Phys. Rev. B 88, 115145 (2013).

[Ashcroft1976] N. W. Ashcroft and N. D. Mermin, Solid State Physics, CBS Publishing Asia Ltd., 1976.

[Auguie2008] B. Auguié and W. L. Barnes, Phys. Rev. Lett. 101, 143902 (2008).

[Barker1975] A. S. Barker Jr. *et al.*, Phys. Rev. B 12, 2049 (1975).

[Bayliss1983] S. C. Bayliss *et al.*, J. Phys. C: Solid State Phys. 16, L831 (1983).

[Bayliss1984] S. C. Bayliss *et al.*, J. Phys. C: Solid State Phys. 17, L533 (1984).

[Beal1975] A. R. Beal *et al.*, J. Phys. C: Solid State Phys. 8, 4236 (1975).

[Benda1974] J. A. Benda, Phys. Rev. B 10, 1409 (1974).

[Borghesi1984] A. Borghesi *et al.*, Phys. Rev. B 29, 3167 (1984).

[Bovet2003] M. Bovet *et al.*, Phys. Rev. B 67, 125105 (2003).

[Boyer2002] D. Boyer *et al.*, Science 297, 1160 (2002).

[Brockman2000] J. M. Brockman *et al.*, Annu. Rev. Phys. Chem. 51, 41 (2000).

[Bruggeman1935] D. A. G Bruggeman, Ann. Physik (Leipz.) 24, 636 (1935).

[Caille1983] A. Caillé *et al.*, Phys. Rev. B 28, 5454 (1983).

[Cappelluti2012] E. Cappelluti et al., GraphITA 2011, (edited by L. Ottaviano and V. Morandi), Springer-Verlag, Berlin, 2012, p. 27

[Carr1985] G. L. Carr and S. Perkowitz, Infrared and millimeter waves 13, 171 (1985).

[Castellan2013] J-P. Castellan *et al.*, Phys. Rev. Lett. 110, 196404 (2013).

[Cazzaniga2012] M. Cazzaniga *et al.*, Phys. Rev. B 85, 195111 (2012)

[Cercellier2007] H. Cercellier *et al*., Phys. Rev. Lett. 99, 146403 (2007).

[Chan1973] S. K. Chan and V. Heine, J. Phys. F 3, 795 (1973).

[Cui2006] X. Y. Cui *et al*., Phys. Rev. B 73, 085111 (2006).

[Danzenbacher 2000] S. Danzenbächer *et al*., Mol. Cryst. And Liq. Cryst. 341, 45 (2000).

[Dardel1992] B. Dardel *et al*., Phys. Rev. B 46, 7407 (1992).

[Dean2011] N. Dean et al., Phys. Rev. Lett. 106, 016401 (2011).

[Demko2010] Demko *et al*., Eur. Phys. J. B **74**, 27–33 (2010).

[DiPietro2014] P. Di Pietro, Optical Properties of Bismuth-Based Topological Insulators, Springer Theses, Springer International Publishing Switzerland 2014.

[DiSalvo1975] F. J. Di Salvo *et al*., Phys. Rev. B 12, 2220 (1975).

[DiSalvo1976A] F. J. Di Salvo *et al*., Phys. Rev. Lett. 36, 885 (1976).

[DiSalvo1976B] F. J. Di Salvo *et al*., Phys. Rev. B 14, 4321 (1976).

[DiSalvo1978] F. J. Di Salvo *et al*., Phys. Rev. B 17, 3801 (1978).

[Dressel2003] M. Dressel and G. Grüner, Electrodynamics of solids: optical properties of electrons in matter, Cambridge University Press, 2003.

[Dresselhaus2001] M. S. Dresselhaus, Optical Properties of Solids, Lectures in Solid State Physics, 2001 (http://web.mit.edu/course/6/6.732/OldFiles/www/6.732-pt2.pdf).

[Duyne2004] R. P.Van Duyne, Science 306, 985 (2004).

[Efetov1977] K. B. Efetov and A.I. Larkin, Zh. Eksp. Tear. Fiz. 72, 7350 (1977).

[Endo2000] T. Endo *et al*., Surface Science 453, 1 (2000).

[PI1-Web-Ellipsometry] http://www.pi1.uni-stuttgart.de/forschung/methoden/ellipsometrie.en.html.

[Fano1961] U. Fano, Phys. Rev. 124, 1866 (1961).

[Fazekas1979] P. Fazekas and E. Tosatti, Philosophical Magazine B 39, 229 (1979).

[Fazekas1980] P. Fazekas and E. Tosatti, Physica B 99, 183 (1980).

[Fischer2008] H. Fischer and O. J. F. Martin, Optics Express 16, 9144 (2008).

[Freericks2009] Freericks *et al*., Phys. Stat. Sol. B 246, 948 (2009).

[Freund1984] G. A. Freund, Jr. and R. D. Kirby, Phys. Rev. B 30, 7122 (1984).

[Friend1987] R. H. Friend and A. D. Yoffe, Advances in Physics 36, 1 (1987).

[Fukuyama1978] H. Fukuyama and P.A. Lee, Phys. Rev. B 17, 535 (1978).

[Garnett1904] J. C. M. Garnett, Phil. Trans. Roy. Soc. A203, 385 (1904).

[Gasparov2002] L. V. Gasparov *et al*., Phys. Rev. B 66, 094301 (2002).

[Gorshunov1986] B. P. Gorshunov *et al*., Phys. Stat. Sol. B 137, K89 (1986).

[Greenaway1965] D. L. Greenaway and R. Nitsche, J. Phys. Chem. Solids 26, 1445 (1965).

[Grüner1988] G. Grüner, Rev. Mod. Phys. 60, 1129 (1988).

[Grüner1994] G. Grüner, Density Waves in Solids, Perseus publishing, 1994.

[Haes2005] A. J. Haes *et al*., MRS Bull. 30, 368 (2005).

[Haynes2002] C. L. Haynes *et al*., J. Phys. Chem. B 106, 1898 (2002).

[Hellmann2012] S. Hellmann *et al*., Nature Commun. 3, 1039 (2012).

[Herres1984] W. Herres and J. Gronholz, Understanding FT-IR data processing, part 1-3, Comp. Appl. Lab. 2, 216 (1984).

[Hildebrand2014] B. Hildebrand *et al*. Phys. Rev. Lett. 112, 197001 (2014).

[Holy1977] J. Holy *et al*., Phys. Rev. B 16, 3628 (1977).

[Hughes1977] H. P. Hughes, J. Phys. C: Solid State Phys. 10, L319 (1977).

[Hughes2001] H. P. Hughes and H. Starnberg (Eds.), Electron Spectroscopies Applied to Low-dimensional Structures (Vol. 24), Springer, 2001.

[Imry1975] I. Imry and S. K. Ma, Phys. Rev. Lett. 35, 1399 (1975).

[Jellinek1962] F. Jellinek, J. Less-Common Met. 4, 9 (1962).

[Jensen1999] T. R. Jensen *et al*., J. Phys. Chem. B 103, 9846 (1999).

[Jerome1967] D. Jérome *et al*., Phys. Rev. 158, 462 (1967).

[Joe2014] Y. I. Joe *et al*., Nature Phys. Lett. 10, 421 (2014).

[Johnson1972] P. B. Johnson and R. W. Christy, Phys. Rev. B 6, 4370 (1972).

[Karecki1979] D. R. Karecki and B. P. Clayman, Phys. Rev. B 19, 6367 (1979).

[Kelly2003] K. L. Kelly *et al*., J. Phys. Chem. B 107, 668 (2003).

[Kevan1991] S. D. Kevan (Ed.), Angle Resolved Photoemission, Elsevier, 1991.

[Kidd2002] T. E. Kidd *et al*., Phys. Rev. Lett. 88, 226402 (2002).

[Kim1994] J.-J. Kim *et al*., Phys. Rev. Lett. 73, 2103 (1994).

[Kireev1978] P. S. Kireev, Semiconductor Physics 2nd ed., Mir Publishers, 1978.

[Kittel1996] C. Kittel, Introduction to Solid State Physics, 7th ed., John Wiley & Sons, Inc., 1996.

[Knobloch1993] H. Knobloch *et al*., J. Chem. Phys. 98, 10093 (1993).

[Knoll1998] W. Knoll, Annu. Rev. Phys. Chem. 49, 569 (1998).

[Ko2011] K.-T. Ko *et al*., Phys. Rev. Lett. 107, 247201 (2011).

[Kohn1959] W. Kohn, Phys. Rev. Lett. 2, 392 (1959).

[Kramers1926] H.A. Kramers, Nature 117, 775 (1926).

[Kronig1926] R. de L. Kronig, J. Opt. Soc. Am. 12, 547 (1926).

[Kuper1955] C. G. Kuper, Proc. R. Soc. London, Ser. A 227, 214 (1955).

[Kusmartseva2009] A. F. Kusmartseva *et al*., Rev. Lett. 103, 236401 (2009).

[Lahoud2014] E. Lahoud *et al*., Phys. Rev. Lett. 112, 206402 (2014).

[LakeshoreSpecifications] http://www.lakeshore.com/products/cryogenic-temperature-sensors/cernox/models/pages/Specifications.aspx.

[Lamprecht2000] B. Lamprecht *et al*., Phys. Rev. Lett. 84, 4721 (2000).

[Landau1960] L. D. Landau and E. M. Lifshitz, Electrodynamics of Continuous Media, Addison-Wesley, 1960.

[Landauer1952] R. Landauer, J. Appl. Phys. 23, 779 (1952).

[Lee1974] P. A. Lee, T. M. Rice and P. W. Anderson, Solid State Comm. 14, 703 (1974).

[Lee1979] P. A. Lee and T.M. Rice, Phys. Rev. B 19, 3970 (1979).

[Leventi-Peetz1995] A. Leventi-Peetz et al., Phys. Rev. B 51, 17965 (1995).

[Levy1981] F. Lévy *et al.*, Physica 105B, 151 (1981).

[Li2007] G. Li *et al.*, Phys. Rev. Lett. 99, 027404 (2007).

[Li2012] L. J. Li *et al.*, Europhys. Lett. 97, 67005 (2012).

[Liu2013] Y. Liu *et al.*, Appl. Phys. Lett. 102, 192602 (2013).

[Manzke1989] R. Manzke *et al.*, Europhys. Lett. 8, 195 (1989).

[May2011] M. M. May *et al.*, Phys. Rev. Lett. 107, 176405 (2011).

[McFarland2003] A. D. McFarland and R. P. Van Duyne, Nano Lett. 3, 1057 (2003).

[McMillan1976] W. L. McMillan, Phys. Rev. B 14, 1496 (1976).

[Michaels2000] A. M. Michaels *et al.*, J. Phys. C 104, 11965 (2000).

[Mihaly2006] L. Mihály, lectures, Budapest University of Technology and Economics, 2006., http://dept.phy.bme.hu/education/optical_spectroscopy/lecture2_rev.pdf

[Mock2002] J. J. Mock *et al.*, J. Chem. Phys. 116, 6755 (2002).

[Monney2011] C. Monney *et al.*, Phys. Rev. Lett. 106, 106404 (2011).

[Morosan2006] E. Morosan *et al.*, Nature Physics 2, 544 (2006).

[Morosan2010] E. Morosan *et al.*, Phys. Rev. B 81, 094524 (2010).

[Mott1974] N. F. Mott, Metal-Insulator Transitions, Taylor & Francis, London, 1974.

[Novotny2012] L. Novotny and B. Hecht, Principles of Nano-Optics, 2nd ed., Cambridge University Press, 2012.

[Pakizeh2009] T. Pakizeh *et al*., Nano Lett. 9, 882 (2009).

[Peierls1955] R. Peierls, Quantum Theory of Solids, Clarendon, Oxford, 1955.

[Pettenkofer1991] C. Pettenkofer *et al*., Surface Science 251/252, 583 (1991).

[Pettenkofer1994] C. Pettenkofer and W. Jaegermann, Phys. Rev. B 50, 8816 (1994).

[PI1-Web-FTIR] http://www.pi1.uni-stuttgart.de/forschung/methoden/fourier.en.html.

[Pillo2000] T. Pillo *et al*., Phys. Rev. B 62, 4277 (2000).

[Pillo2001] T. Pillo *et al*., Phys. Rev. B 64, 245105 (2001).

[Pines1966] D. Pines and P. Nozieres, The Theory of Quantum Liquids, Vol. 1, Addison-Wesley, 1966.

[Rasch2008] J. C. E. Rasch *et al*., Phys. Rev. Lett. 101, 237602 (2008).

[Ritschel2013] T. Ritschel et al., Phys. Rev. B 87, 125135 (2013).

[Rohwer2011] T. Rohwer *et al*., Nature 471, 490 (2011).

[Rossnagel2002] K. Rossnagel *et al*., Phys. Rev. B 65, 235101 (2002).

[Rossnagel2006] K. Rossnagel and N. V. Smith, Phys. Rev. B 73, 073106 (2006).

[Rossnagel2011] K. Rossnagel, J. Phys.: Condens. Matter 23, 213001 (2011).

[Rouxel1986] J. Rouxel (Ed.), Crystal Chemistry and Properties of Materials with Quasi-One-Dimensional Structures, Reidel, 1986.

[Sato2014] H. Sato et al., Phys. Rev. B 89, 155137 (2014).

[Schlenker1989] C. Schlenker (Ed.), Low Dimensional Electronic Properties of Molybdenum Bronzes and Oxides, Kluwer, 1989.

[Scruby1975] C. B. Scruby, Philosophical Magazine 31, 255 (1975).

[Sham1976] L. J. Sham and B. R. Patton, Phys. Rev. B 13, 2151 (1976).

[Shriver1999] D. F. Shriver and P. W. Atkins, Inorganic Chemistry (3rd ed.). Oxford University Press., 1999.

[Sipos2008] B. Sipos *et al.*, Nature Materials 7, 960 (2008).

[Smith1995] K. E. Smith, Annu. Rep. Prog. Chem., Sect. C: Phys. Chem. 92, 253 (1995).

[Smith2011] B. C. Smith, Fundamentals of Fourier Transform Infrared Spectroscopy 2nd ed., CRC Press, Taylor & Francis Group, 2011.

[Snow2003] C. S. Snow *et al.*, Phys. Rev. Lett. 91, 136402 (2003).

[Spijkerman1997] A. Spijkerman *et al.*, Phys. Rev. B 56, 13757 (1997).

[Stojchevska2014] L. Stojchevska *et al.*, Science 344, 177 (2014).

[Stroud1979] D. Stroud, Phys. Rev. B 19, 1783 (1979).

[Stroud1998] D. Stroud, Superlattices and Microstructures 23, 567 (1998).

[Thomsen1991] C. Thomsen, Topics in Applied Physics: Light Scattering in Solids VI (edited by M. Cardona and G. Güntherodt), Springer-Verlag, Berlin, 1991, Vol. 68, p. 327

[Thomson1972] R. E. Thomson *et al.*, Phys. Rev. Lett. 29, 163 (1972).

[Thomson1988] R. E. Thomson *et al.*, Phys. Rev. B 38, 10734 (1988).

[Thomson1994] R. E. Thomson *et al.*, Phys. Rev. B 49, 16899 (1994).

[Tison2004] Y. Tison *et al.*, Surface Science 563, 83 (2004).

[Traum1978] M. M. Traum *et al.*, Phys. Rev. B 17, 1836 (1978).

[Tutiš2014] private communication with Dr. Eduard Tutiš.

[Uchida1981] S. Uchida and S. Sugai, Physica B 105, 393 (1981).

[VanWezel2010] J. VanWezel *et al.*, Phys. Rev. B 81, 165109 (2010).

[Weber2011] F. Weber *et al.*, Phys. Rev. Lett. 107, 266401 (2011).

[Willets2007] K. A. Willets and R. P. Van Duyne, Annu. Rev. Phys. Chem. 58, 267 (2007).

[Wilson1969] J. A. Wilson and A. D. Yoffe, Advances in Physics 18, 193 (1969).

[Wilson1975] J. A. Wilson, Adv. Phys. 24, 117 (1975).

[Wilson1978] J. A. Wilson, Phys. Rev. B 17, 3880 (1978).

[Wu1988] X. L. Wu *et al*., Nature 335, 55 (1989).

[Wu1989] X. L. Wu and C. M. Lieber, Science 243, 1703 (1989).

[Wu1990] X. L. Wu and C. M. Lieber, Phys. Rev. Lett. 64, 1150 (1990).

[Xu2010] P. Xu *et al*., Phys. Rev. B 81, 172503 (2010).

[Zeng1989] X. C. Zeng *et al*., Phys. Rev. B 39, 13224 (1989).

[Zhu2014] Z. Zhu *et al*., Scientific Reports 4, 4025 (2014).

[Ziman1960] J. M. Ziman, Electrons and Phonons, Oxford University Press, 1960.

[Zwick1998] F. Zwick *et al*., Phys. Rev. Lett. 81, 1058 (1998).

Biography

Kristijan Velebit was born on January 31, 1980 in Sisak, Croatia. He finished high school in 1998 in Petrinja. Under the supervision of Prof. Dr. Miroslav Požek, he graduated physics in 2009 at the Department of Physics, Faculty of Science of the University of Zagreb in Croatia. His diploma thesis was titled “Microwave study of the underdoped superconductor $HgBa_2CuO_4$ in the pseudogap regime”. From February 2010, he works as a research assistant at the Laboratory for the Physics of Transport Phenomena of the Institute of Physics in Zagreb. In the school year 2010/2011 he started the condensed matter physics doctoral study at the Faculty of Science, University of Zagreb, under the supervision of Dr. Ana Smontara. Kristijan Velebit participated in an international scientific collaboration within the UKF project 65/10 “New electronic states driven by frustration in layered materials”. The collaboration was supported by the DAAD (Deutscher Akademischer Austauschdienst – German Academic Exchange Service) research grant awarded to Kristijan Velebit for the project “Optical properties of selected layered materials”. In 2011, Kristijan Velebit stayed a total of six months at the 1. Physikalisches Institut, Universität Stuttgart, in Germany, in the group of Prof. Dr. Martin Dressel, to adopt the techniques of measuring the optical properties. Kristijan Velebit is a coauthor of two scientific papers published in CC journals, and 15 contributions at conferences, both international and domestic.

List of publications

1. A. Smontara, P. Popčević, D. Stanić, K. Velebit, J. Dolinšek, *Anisotropic Transport Properties of the* $Al_{13}TM_4$ *and T-Al-Mn-Fe Complex Metallic Alloys*, Philosophical magazine 91, 2746-2755 (2011) .

2. P. Popčević, I. Batistić, E. Tutiš, K. Velebit, M. Heggen, M. Feuerbacher, *The Generalization of the Kinetic Equations and the Spectral Conductivity Function to Anisotropic Systems: Case* $T\text{-}Al_{72.5}Mn_{21.5}Fe_6$ *Complex Metallic Alloy*, Croatica chemica acta 83, 95-100, (2010).

Workshops and conferences

1. Popčević, Petar; Batistić, Ivo; Velebit, Kristijan; Živković, Ivica; Barišić, Neven; Tutiš, Eduard; Smontara, Ana; Sidorenko, J.; Jaćimović, J.; Tsyrulin, N.; Piatek, J.; Berger, H.; Forro, Laszlo. *Evolution of electronic scattering on frustrated magnetic system under pressure*. From Solid State Physics to Biophysics VII, Dubrovnik, Croatia, 2014, invited talk.

2. Velebit, Kristijan; Popčević, Petar; Batistić, Ivo; Berger, H.; Dressel, M.; Smontara, Ana;Barišić, Neven; Forró, Laszlo; Tutiš, Eduard. *Imprints of nanostructured and Mott phase in optical phonons and continua of 1T-*TaS_2. International school and workshop on electronic crystals (ECRYS 2014), Orsay, France, invited talk.

3. Popčević, Petar; Velebit, Kristijan; Bilušić, Ante; Gille, Peter; Smontara, Ana. *Transport in high quality decagonal quasiperiodic monocrystals d - AlCoNi vs d - AlCoCu*. C-MAC Days 2014, Zagreb, Croatia, talk.

4. Velebit, Kristijan; Popčević, Petar; Smontara, Ana; Berger, Helmuth; Forro, Laszlo; Batistić, Ivo; Barišić, Neven; Dressel, Martin; Tutiš, Eduard. *Optički odziv nano-teksturirane i Mottove faze 1T-*TaS_2. 8th Scientific meeting of Croatian Physical Society, Primošten, Croatia, 2013, talk.

5. Popčević, Petar; Velebit, Kristijan; Kashimoto, Shiro; Dolinšek, J.; Smontara, Ana. *Quantum critical behavior in transport properties of i-AuAlYb*. C-MAC Days 2013, Ljubljana, Slovenia, poster.

6. Popčević, Petar; Velebit, Kristijan; Stanić, Denis; Ivkov, Jovica; Bilušić, Ante; Smontara, Ana. *Anisotropic Transport Properties of Decagonal Quasicrystals and Their Periodic Approximants*. From Solid State Physics to Biophysics VI, Dubrovnik, Croatia, 2012, poster.

7. Velebit, Kristijan; Popčević, Petar; Tutiš, Eduard; Smontara, Ana; Berger, H.; Forró, L.; Eichler, M.; Wu, D.; Barišić, Neven; Dressel, M. *Optical conductivity of the nano-textured phase in 1T-*TaS_2. Physics of Low-Dimensional Conductors: Problems and Perspectives, Zagreb, Croatia, 2012, poster.

8. Velebit, Kristijan; Popčević, Petar; Smontara, Ana; Berger, H.; Forró, L.; Dressel, M.; Barišić, Neven. *The nano-textured phase of 1T-*TaS_2 *probed by optical conductivity*. Electronic States and Physes Induced by Electric or Optical Impacts, Orsay, France, 2012, talk.

9. Popčević, Petar; Velebit, Kristijan; Stanić, Denis; Ivkov, Jovica; Bihar, Željko; Bilušić, Ante; Smontara, Ana. *Thermoelectric properties of quasicrystals*. 14th Joint Vacuum Conference - 12th European Vacuum Conference - 11th Annual Meeting of the German Vacuum Society - 19th Croatian - Slovenian Vacuum Meeting, Dubrovnik, Croatia, 2012, invited talk.

10. Ivkov, Jovica; Velebit, Kristijan; Popčević, Petar; Smontara, Ana; Bilušić, Ante; Berger, H.; Forró, László. *Transport properties of 1T-*TaS_2 *single crystal*. Physics of Low-Dimnesional Conductors: Problems and Perspectives, Zagreb, Croatia, 2012, poster.

11. Popčević, Petar; Ivkov, Jovica; Stanić, Denis; Velebit, Kristijan; Cmrk, Danijel; Smontara, Ana. *Anizotropija transportnih svojstava monokristala dekagonalnog kvazikristala d-*$Al_{70}Co_{10}Ni_{20}$. 7th Scientific meeting of Croatian Physical Society, Primošten, Croatia, 2011, poster.

12. Popčević, Petar; Stanić, Denis; Velebit, Kristijan; Smontara, Ana. *Porijeklo anizotropije transportnih svojstava kompleksnih intermetalika iz obitelji* $Al_{13}TM_4$. 7th Scientific meeting of Croatian Physical Society, Croatia, 2011, poster.

13. Popčević, Petar; Ivkov, Jovica; Stanić, Denis; Velebit, Kristijan; Cmrk, Danijel; Dolinšek J.; Gille, P.; Smontara, Ana. *Anisotropic transport properties of single-crystalline d-Al-Ni-Co decagonal quasicrystal*. CMAC Days, European Integrated Center for the Development of New Metallic Alloys and Compounds, Industry Days and Workshop Sessions, Dresden, Germany, 2010, talk.

14. Velebit, Kristijan; Popčević, Petar; Smontara, Ana; Wu, D.; M. Dressel, M.; Cao, G. H.; Xu, ZA.; Barišić, Neven. *Observation of the Fermi Liquid Behavior in 122-Ironpnictides*. Recent advances in broad-band solid-state NMR of correlated electronic systems, Trogir, Croatia, 2010, poster.

15. Popčević, Petar; Stanić, Denis; Velebit, Kristijan; Bauer, B.; Gille, P.; Heggen, M.; Feuerbacher, M.; Dolinšek, J.; Smontara, Ana. *Origin of the anisotropy in the transport properties of the* $Al_{13}TM_4$ *complex intermetallics*. CMAC Days, European Integrated Center for the Development of New Metallic Alloys and Compounds, Industry Days and Workshop Sessions, Dresden, Germany, 2010, talk.